

NOVEL MODELS AND OBSERVATIONS OF THE SOLAR TRANSITION REGION

by

Jacob Douglas Parker

A dissertation submitted in partial fulfillment  
of the requirements for the degree

of

Doctor of Philosophy

in

Physics

MONTANA STATE UNIVERSITY  
Bozeman, Montana

October 2021

©COPYRIGHT

by

Jacob Douglas Parker

2021

All Rights Reserved

## DEDICATION

I'd like to dedicate this work to my family. To my father and mother, Doug and Raydene, who instilled in me the value of education from a very early age, and who supported me every step of the way, for much longer than they should have had to, in every way I can imagine. Thank you also for teaching me everything I know about enjoying the world and people around me. Because of you my experience in Bozeman has been filled with friends and adventure, something I will never forget. To my sister, Nikki, who somehow managed to finish school before me, put up with me through the worst eras of my growth, and has become a source of level headed wisdom and kindness in my life when I struggle to find it myself. And to my fiancé, Emmy. You have been by my side during my entire experience at MSU. Together we have experienced pain and play, made so many great friends, and have grown tremendously together since we met 13 years ago. Good news is, I think now this means you won't have to marry a student!

Thank you all so much. This has been a long journey, and it's not over yet. I love you guys.

## ACKNOWLEDGEMENTS

I did not complete this work alone. In my eleven years at Montana State I have had the opportunity to work with, and learn from, so many of you. I hope I can acknowledge you all, but if I can't, thank you so much and I hope our paths continue to cross for years to come.

Thank you to C. Riedel, D. Longcope, J. Qiu, C. Kankelborg, J. Carlsten, and R. Babbitt, all of whom I have taken multiple physics courses from, for being supportive, always available, and fun to be around. Thank you to the Physics staff, to N. Williams, M. Jarrett, and J. Bradley, for your support and friendship over the years. Thank you to K. Mashburn and H. Courier for teaching me how to build flight hardware. Thank you to T. Rust for helping me through the frustrations of optical testing, focus, and alignment. Thank you to S. Atwood for starting me down this road. Thank you M. Johnson, N. Goldsworth, H. Moore, A. Tientze, J. Martinez, B. Carroll, and C. Bunn for helping to build and launch ESIS. Thank you to the team at WSMR circa 2019, the Beabouts, H. Haight, and K. Kobayashi for all the assistance and knowledge you have shared with me and the ESIS team. Thank you to D. McKenzie for assisting as a committee member, even after leaving MSU, and to A. Winebarger, for working closely with me over the last year and always being available to help. Lastly to Roy Smart, thank you for all your help in the world of electronics and coding, and insistence on getting things right, and again to Charles, the opportunities and education you've provided me are immeasurable. We made an amazing team, and accomplished something very cool. I hope that doesn't end, and thank you.

## TABLE OF CONTENTS

1. INTRODUCTION .....	1
How does the sun affect us and why do we care? .....	1
Where does the sun's energy and magnetic field come from?.....	2
The Solar Atmosphere .....	2
What are we looking for when we study the solar atmosphere and why? .....	5
How do we study the solar atmosphere?.....	6
Thesis Outline.....	12
2. MODELING A PROPAGATING SAWTOOTH FLARE RIBBON AS A TEARING MODE IN THE PRESENCE OF VELOCITY SHEAR .....	15
Contribution of Authors and Co-Authors .....	15
Manuscript Information .....	16
Abstract .....	17
Introduction .....	17
Linear Tearing Mode Instability with Shear Flow.....	25
Modeling Observations.....	35
Geometry.....	35
Introducing Dimensions .....	37
The Saturated State .....	38
Transformation to Observed Quantities.....	40
Discussions and Conclusions .....	45
Acknowledgements.....	48
3. DETERMINING THE SPECTRAL CONTENT OF MOSES IMAGES.....	49
Contribution of Authors and Co-Authors .....	49
Manuscript Information .....	50
Abstract .....	51
Introduction .....	51
Data .....	54
MOSES .....	54
EIT .....	57
Methods.....	58
Difference Image Cross-Correlation .....	58
Significance Testing .....	61
Forward Model.....	66
Results.....	69
Discussion and Conclusions .....	73

## TABLE OF CONTENTS CONTINUED

Acknowledgments .....	77
4. FIRST FLIGHT OF THE EUV SNAPSHOT IMAGING SPECTROGRAPH (ESIS) .....	78
Contribution of Authors and Co-Authors .....	78
Manuscript Information .....	79
Abstract .....	80
Introduction .....	80
ESIS Mission .....	84
The Experiment .....	85
Launch and Data Collection.....	87
Data .....	90
Level 0 Data .....	92
Level 1 Data .....	93
Level 3 Data .....	95
Conversion to Photons and Despiking.....	95
Optical Distortion Correction and Channel Co-Alignment .....	97
Vignetting Correction.....	98
Relative Radiometric Correction .....	102
Preliminary Results .....	104
Level 3 Difference Images.....	104
Early Inversions .....	111
Discussion/Conclusions and Future Work .....	115
Acknowledgments .....	119
5. FINAL CONCLUSIONS.....	120
REFERENCES CITED.....	123
APPENDICES .....	129
APPENDIX A : Despiking .....	130
APPENDIX B : Multiplicative Algebraic Reconstruction Technique .....	132

## LIST OF TABLES

Table	Page
3.1 Average MOSES Image Spectral Content .....	73
4.1 Dominant spectral lines observed by ESIS. Intensities are relative to O V 629.7 Å.....	84
4.2 ESIS Flight Data Summary .....	90

## LIST OF FIGURES

Figure	Page
1.1 The anatomy of the sun from core to corona. Credit: NASA, Mysteries of the Sun .....	3
1.2 The solar spectrum captured in April 2008 by the Solar instrument onboard the International Space Station. ©CNRS.....	8
1.3 Extreme Ultraviolet images from four different AIA chan- nels. Narrowband images of the sun allow us to study different layers of the solar atmosphere by isolating wave- lengths from emission lines known to form most often at specific temperatures. These images are displayed in log scale to increase contrast and the color tables are synthetic (since these are not visible light images) and assigned by the instrument team.....	10
2.1 A frame from the IRIS 1400Å SJI showing the flare ribbon from the 2014 Apr 18 flare. A subsection of the full SJI is shown on the left using inverse log-scale, with axes marked in arcseconds from disk center. The dark horizontal band is the flare ribbon, and a lighter vertical line at $x = 552.7$ arcseconds is IRIS's spectrographic slit. An outline of the ribbon is reproduced in red on the right, along with notations showing the spatial period, $\lambda$ , amplitude, $h$ , and pattern velocity, $v_0/2$ . A green island-chain shows the proposed orientation of the tearing mode instability, displaced southward for clarity by a distance greater than proposed in the model. A second velocity arrow shows the direction of the proposed shear velocity, $v_0$ , which causes the island chain to move at $v_0/2$ .....	20
2.2 Figure 11 from BLQ reproduced with permission. The upper panel shows the mean Doppler velocity of the blue component of the Si IV lines, plotted against the mean position of the sawtooth pattern along the slit. Time is indicated by color, coded in the bar along the right. The bottom panel repeats this, but highlights in color one of the best defined oscillations.....	22

## LIST OF FIGURES CONTINUED

Figure	Page
2.3 The eigenfunction for the most unstable mode with parameters $S = 1 \times 10^7$ , $V = 1.5 \times 10^{-3}$ , and $\bar{k} = .0234$ plotted along a logarithmic spatial coordinate. This mode has a growth rate $\bar{\gamma} = 2 \times 10^{-4}$ . ....	33
2.4 Contours of $\bar{B}$ (black) and $\bar{u}$ (red) with shear flow $V = 0$ , $1.5 \times 10^{-3}$ , $0.1$ in a,b,c respectively. ....	34
2.5 In the proposed magnetic field configuration a flow in the $\hat{x}$ direction, $\vec{V}$ (blue), deflects overlying magnetic field, $\vec{B}$ (black), at some angle $\theta$ to the inner recently reconnected magnetic field, $\vec{B}$ (red). This results in the labeled currents, $\vec{J}$ (green). The dashed box shows a blown up region of the secondary current sheet where we model the TM/KH Instability. We also show the LOS of the observation to demonstrate how motion in the x-y plane translates to LOS Doppler velocities.....	36
2.6 Contours of TM/KH eigenfunctions for $S = 10^4$ , $\bar{k} = .1315$ , and $V' = .037$ with $\alpha = 1$ . The thick green line shows the trajectory of a particle that started at $[\bar{x}, \bar{y}] = [86, 18]$ . ....	39
2.7 Contoured eigenfunctions of an approximated saturated state. Here the instability growth has stopped and the reconnection inflow/outflow has gone to zero. The green contour shows the trajectory of a fluid element beginning at $[\bar{x}, \bar{y}] = [86, 13]$ .....	41
2.8 Panels a and b show the green trajectory from Figure 2.6 after undergoing the Galilean transform in Equation (2.28). Panels c and d show the same for the green trajectory in Figure 2.7. All displacements have been foreshortened to account for off disk observation and scaled to physical units. The green dot indicates the particles starting location. ....	44

## LIST OF FIGURES CONTINUED

Figure	Page
3.1 Time averaged images for the $m = 0$ and $1$ spectral orders (top row), followed by their difference, $m = 1$ minus $m = 0$ . Regions one through three, boxed in red, show regions of high spectral contamination. Dark features from the $m = 0$ order are adjacent to white smears with pixel shifts too large to be Doppler shifts.....	56
3.2 SOHO EIT Images taken closest the MOSES Launch on February 8th, 2006. Each image was rotated to 2006-02-08 18:47 UT to match the middle MOSES exposure time. After rotation, the EIT 304 channel was linearly co-aligned to the MOSES zero order, and then the same transformation was applied to every other channel. Each image has been fourth root scaled.....	57
3.3 Example 1D MOSES row in the $m = 1$ (a), $0$ (b), and $-1$ (c) spectral orders followed by the cross correlation of $m=1$ and $0$ (d) and the cross-correlation of $m = -1$ and $0$ (e). The cross-correlation of any two MOSES orders is dominated by the autocorrelation of stationary He II features and background making them less useful in identifying spectral content. The strong peaks in correlation at $\pm 250$ pixels are the result of the two bright He II features at $0$ and $250$ overlapping.....	59
3.4 Example MOSES rows in $m = 1$ (a), $0$ (b), and $-1$ (c) spectral orders. Two difference images, $m = 1$ minus $m = 0$ (d) and $m = -1$ minus $m = 0$ (e) are cross-correlated (e). Taking a difference removes stationary He II features so that peaks in cross-correlation are indicative of extra spectral content. Even in this simple example one cannot read off the spectral content of the MOSES images, demonstrating the need for a forward model. ....	60

## LIST OF FIGURES CONTINUED

Figure	Page
3.5 The mean cross-correlation function of MOSES difference image rows (red) is compared to a distribution of mean cross-correlations from a selection of randomly generated test row differences (Section 3). The top panel shows the distribution after taking the mean of 1024 (the number of MOSES rows) randomly chosen test row differences 10,000 times. The bottom panel challenges that all 1024 rows of MOSES are unique and shows the distribution for only 128 randomly chosen difference rows, also 10,000 times. In either case the mean cross-correlation values from the MOSES data exceed the 98 percent confidence interval and are therefore deemed significant and indicative of spectral content in the MOSES data. ....	62
3.6 Best fit DEM used to generate the final synthetic MOSES images. ....	70
3.7 The top panel shows the entire mean cross-correlation along image rows of the MOSES (blue) and synthetic (red) difference images. The bottom panel shows a zoomed in view of the same function in order to highlight features near zero lag. ....	70
3.8 The $I_{+1} - I_0$ difference image, also shown in Figure 3.1c, along side the same difference image prepared from the synthetic MOSES images of best fit. Identical regions 1-3 are boxed in each image for comparison. ....	71
3.9 Using the DEM of best fit shown in Figure 3.6 we generated the above synthetic spectrum using Chianti. Each line intensity has also been weighted by the wavelength dependent throughput of the MOSES optical system (normalized and shown in red). ....	72
4.1 A modeled layout showing the orientation of each ESIS channels' detector relative to the solar image at the octagonal fieldstop. The locations of the brightest wavelengths (He I 584.3 Å, Mg X 609.79 Å, and O V 629.7 Å) in the passband are shown on each detector. The He I 584.3 Å line extends off the detector edge by design, as can be seen in Figure 4.4. ....	86

## LIST OF FIGURES CONTINUED

Figure	Page
4.2 The altitude of the ESIS rocket determined from White Sands Missile Range radar data as a function of elapsed time from launch. The event times listed in Table 4.2 are labeled.....	87
4.3 The reference AIA 304 Å data taken at 18:08:17 UTC was used for determining the absolute pointing. The octagon indicates the ESIS FOV.....	89
4.4 The top panel is the raw, Level 0 image captured by Channel 1 of ESIS during apogee. The bottom panel is the same image after Level 1 processing. The Sun viewed through the octagonal field stop in the O v 629.7 Å spectral line is on the right side of the detector, this portion of the detector was cropped to generate Level 3 data. The Sun viewed through the octagonal field stop in the He I 584.3 Å line is partially on the left side of the detector. The Mg x 609.79 Å line is between and partially overlapping both of these two strong lines. ....	94
4.5 (a) An example of the Level 3 data product from Channel 1 taken at 18:08:46. This data has been aligned using nonlinear mapping parameters to the closest co-temporal AIA 304 Å image, shown in (b). .....	96
4.6 For each ESIS exposure (or image sequence) every channel pair, labeled in the legend, is cross-correlated to measure internal alignment quality. The ratio of zero lag cross-correlation after a quadratic transformation to that of a linear transformation is plotted. Every point is above the ratio = 1 line, indicating improved internal alignment for every combination of ESIS channels at each exposure. ....	99
4.7 Panels a and c show example difference between images with Mg x 609.79 Å masked that are uncorrected and corrected for vignetting respectively. The line fit to the column mean as a function of column (fit between the red bars) shows a difference in background of $\approx$ 5 photons before correction (panel b) at the edges of the field of view, and .4 photons after (panel d). .....	100

## LIST OF FIGURES CONTINUED

Figure	Page
4.8 The red hashed region shows the overlap of the Mg X 609.79 Å spectral line in each channel that is masked prior to the vignetting correction and intensity normalization. These images are displayed in log scale in an attempt to bring out the subtle contamination. The outline of the Mg X can be seen very clearly in difference images like Figure 4.9.	103
4.9 Full FOV Difference between Channel 2 and Channel 3 Level 3 images. Arrows denote the positive dispersion direction in Channel 2 and 3. Events a-c are highlighted in Figure 4.10. Inverted results for Events c and d are shown in Section 4. A time series of Event e is shown in Figure 4.11. The associated animation shows these difference images throughout the ESIS observation.	106
4.10 Events a, b and c identified in Figure 4.9 are examples of a mostly blue, red, and broadened even, respectively. The difference between Channels 2 and 3 is shown in the left hand column, while the Channel 2 and Channel 3 intensities are shown in the middle and right columns. The velocity signature is most easily seen in the difference image, while the straight intensities provide information on the line core intensities.	107
4.11 The largest and most complex velocity event (e) captured by ESIS shown at three different times (complete evolution in animation). The event starts as two jets (one red, one blue) with slight spatial separation, evolves into a strong red shift where the event begins paired with faint blue shifted material above, and ends in a complicated combination of velocity not easily interpreted from difference images. Co-temporal images from AIA 304 Å, 171 Å, and 193 Å are included in the animation for additional context.	109

## LIST OF FIGURES CONTINUED

Figure	Page
4.12 Co-aligned AIA 304 Å, 171 Å, and 193 Å images of event e (highlighted in Figure 4.11) are shown with identical locations labeled. The location of peak intensity (e1) in the ESIS Level 3 data is also the location of brightest intensity in these EUV channels. We also note a jet like structure which is very diffuse in the cooler 304 Å images, and visible as a thin line of intensity in 171 Å and 193 Å between the e1 and e2 labels that matches the location of the faint blue shifted structure visible in Level 3 difference images. Animations of these AIA channels, included with Figure 4.11, show material traveling along this line and being ejected away from location e1.....	110
4.13 MART inverted results for event c in Figure 4.9. The integrated intensity (top row) and corresponding Level 3 difference image (second row) are shown at 4 different times. The red box marks the FOV used in the top row. The O v 629.7 Å line profile at each position marked with a red dot is plotted in the matching 3x3 grid in a different color for each time (in order red, green, blue, black). Each MART line profile (dots) is overplotted with a double gaussian fit (solid line). Bulk shifts in km/s for each component of the fit are provided in the legend for each time in their respective color. ....	112
4.14 MART inverted results for event d in Figure 4.9 presented in the same fashion as Figure 4.13.....	113
B.1 Comparison of MART outputs for a single timestamp in Event c (Figure 4.9 and 4.13) with different amounts of filtering. The top row shows the total inverted intensity at a single timestamp each using a different number of MART filtering steps (steps B2 and B3). The lower grid shows the inverted O v spectral line at each red dot for 0, 25, and 75 filtering steps in red, green, and blue respectively. ....	137

## ABSTRACT

The solar atmosphere is an energetic and violent place capable of producing eruptions that affect us on earth. In order to better understand these events, so that we might improve our ability to model and predict them, we observe the sun from space in order to diagnose the local plasma conditions and track its evolution. The transition region, a thin region of the solar atmosphere separating the chromosphere from the corona, is where the solar atmosphere transitions rapidly from ten thousand, to one million degrees and is therefore thought to play an important role in the transfer of mass and energy to the hot corona. The sun's magnetic field, and magnetic reconnection, are thought to contribute to the increased temperature of the corona, since the cooler lower solar atmosphere cannot heat it via thermal processes. Smaller solar eruptions, likely driven by magnetic reconnection, are frequent in the transition region, making it an attractive area of the atmosphere to study and gather information on the processes. Using Computed Tomography Imaging Spectrographs (CTIS), capable of measuring spectral line profiles over a wide fields of view at ever exposure, we find many eruptive events in the transition region to be spatially complex, three dimensional, and to evolve on rapid timescales. I believe this demonstrates the utility of, and need to continue developing, CTIS style instruments for solar study since they provide a more complete picture of solar events, allowing us to improve our understanding of, and ability to predict the activity of, our closest star.

## INTRODUCTION

How does the sun affect us and why do we care?

The Sun is arguably the most relevant astrophysical object to humanity. Its distance from the earth defines a Goldilocks zone (not too hot, not too cold) in which human life can exist. Most of the energy that we use daily can be attributed to the sun, from the obvious solar power, to wind and hydro power (driven by weather created by the sun), to fossil fuels formed from the decay of organic organisms of the past. The rising and setting of the sun defines the daily human experience. Despite our reliance on the sun it is often underappreciated by us and overlooked by physicists who choose to study supposedly more ‘sexy’ astrophysical objects much further away.

In addition to being essential to life on earth, the sun is very violent and energetic. The sun is constantly blasting the earth with radiation and high energy particles. Luckily the earth’s atmosphere and magnetic field protects us from both. The earth’s atmosphere absorbs a large portion of the solar radiation, some of which (x-ray and ultraviolet) can be quite harmful to humans. The earth’s magnetic field steers most energetic particles around earth. Despite these protections we are not immune to the sun’s effects. Satellites are vulnerable to the shower of energetic particles from the sun, which can damage computer chips and lead to charge build up that affects the electronics within. Periods of intense solar activity can heavily perturb the earth’s magnetic field, causing geomagnetic storms. These geomagnetic storms can cause variations in the Ionosphere, a charged layer of our atmosphere, that can negatively effect radio communication and GPS. Astronauts beyond the protection of the earth’s magnetic field exposed to solar energetic particles produced during solar flares would receive large doses of radiation, equivalent to hundreds of dental

x-rays, that can lead to radiation poisoning (Temmer, 2021, and references therein) As our technology advances, and our society becomes less confined to the surface of the earth, it is becoming increasingly important that we improve our understanding of, and our ability to predict, the activity of our closest star.

### Where does the sun's energy and magnetic field come from?

Energy produced in the sun originates from nuclear fusion in the core, where temperatures reach approximately 15 million kelvin (K). From there energy moves outward through the solar interior until reaching the solar surface which has an average temperature of approximately 6600 K (Priest, 2020). The solar interior consists of three layers: the core, the radiation zone, and the convection zone (Figure 1.1). The *radiation* and *convection* zones are each named after their dominant mode of energy transfer. The transition between the two zones, referred to as the tachocline, is where temperature gradient becomes steep enough that the solar plasma becomes unstable to convection, and is likely where the solar magnetic field originates (Priest, 2020). At the solar surface, and within the convection zone, the sun undergoes differential rotation, with plasma rotating more quickly near the equator than the poles. It is the combination of convective motions, and differential rotation, that are understood to generate the sun's global magnetic field (Judge, 2020; Parker, 1979; Priest, 2014). Magnetic field lines produced in the convection zone rise through the solar surface, up into the solar atmosphere, where they become the dominant player and contribute to a host of spectacular solar events, including those studied in this thesis.

### The Solar Atmosphere

The solar surface, referred to as the photosphere, is the base of the solar atmosphere and is defined as the point where photons can escape into space without being reabsorbed by

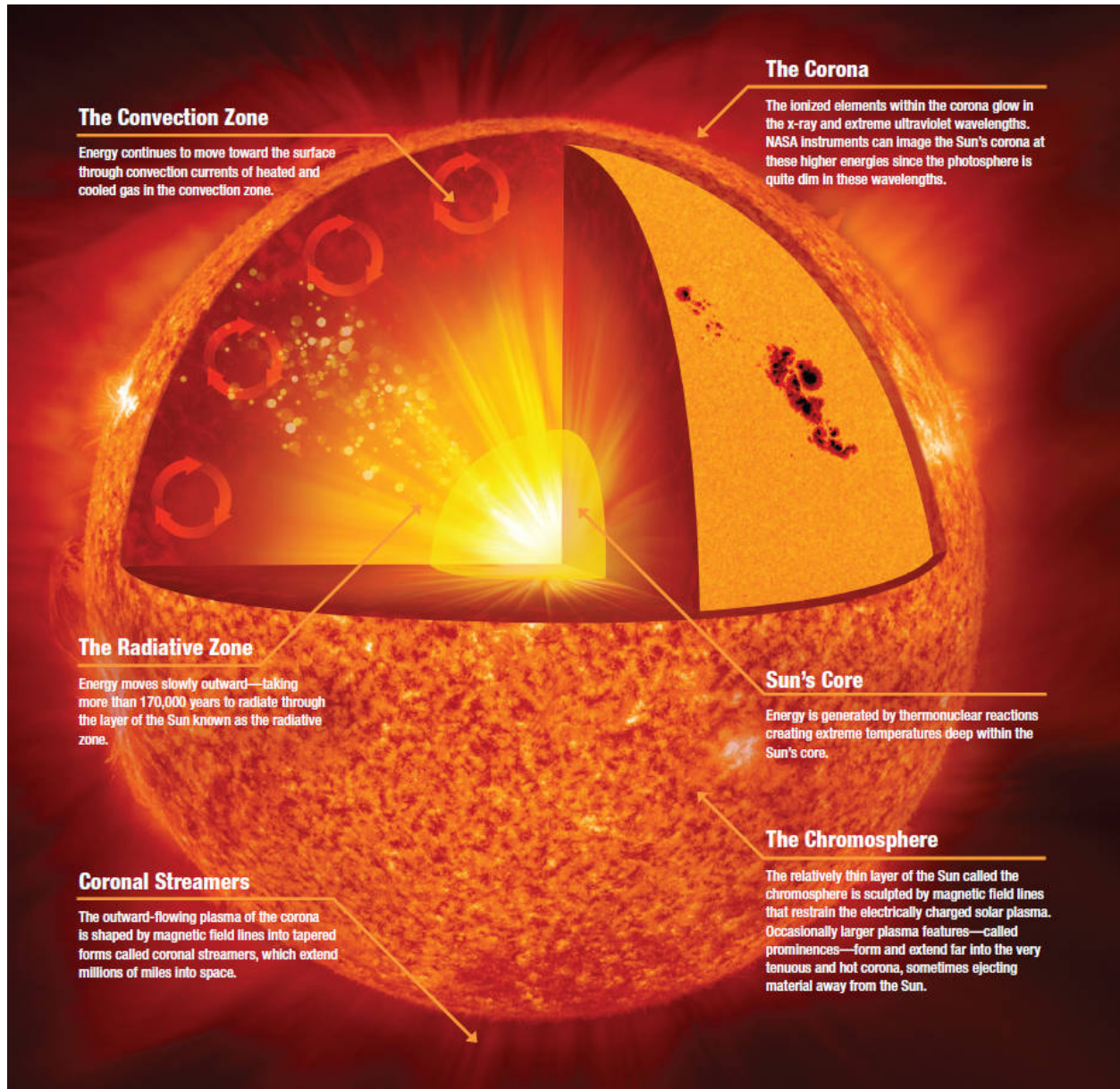


Figure 1.1: The anatomy of the sun from core to corona. Credit: NASA, Mysteries of the Sun

surrounding plasma (Priest, 2014). It is important to note that the photosphere isn't really a surface, but a thin region of plasma with steadily decreasing density and temperature. The height of the photosphere is very thin in comparison to the solar radius,  $\approx 300$  km compared to the  $\approx 700,000$  km solar radius, and therefore looks very crisp when observed from earth (Judge, 2020). It is at the edge of the photosphere where the sun reaches an average temperature minimum of  $\approx 4400$  K (Priest, 2020). The rest of the solar atmosphere consists of (in order of increasing radius) the chromosphere, transition region, and corona (Figure 1.1). The chromosphere, named for the red light it produces that is visible with the naked eye during total solar eclipses, extends approximately 1500 km in height (Priest, 2020). Within the chromosphere the average temperature rises from the temperature minimum to approximately 10,000 K. At the edge of the chromosphere the average temperature increases rapidly to average temperature of approximately 1 million K in the outer most layer of the atmosphere, called the corona (Priest, 2020). The thin region, less than 100 km thick (Priest, 2014), where this transition occurs is appropriately named the transition region.

While it is easiest to think of the solar atmosphere as occurring in one dimensional static layers, in reality it is very structured and dynamic. Above the photosphere, the magnetic field generated in the convection zone expands into a vast canopy of closed loops, with their ends anchored down in the photosphere, as well as open field lines extending out into space. Hotter plasma traces these field lines, allowing us to visualize the complex magnetic field. These magnetic structures have been assigned a whole zoo's worth of names by solar physicists, and are subject to continuous study and debate. Regardless their presence and evolution in images of the solar atmosphere indicate the dynamic and three dimensional nature of the solar atmosphere and make it a very rich area of study.

## What are we looking for when we study the solar atmosphere and why?

The solar atmosphere is very hot and violent. As is described above, the solar atmosphere is hotter than the solar surface! Since the roughly 6000 K photosphere does not have sufficient thermal energy to heat the corona to a million degrees, the energy has to come from somewhere else. A likely source of this energy is the sun's magnetic field (Priest, 2014). The solar plasma, being an almost perfect conductor, is frozen into the magnetic field (Priest, 2014). Therefore, depending on the local plasma conditions, the magnetic field is either drug around by fluid motions, or the plasma is moved by motions in the magnetic field. Beyond the surface of the sun the solar plasma transitions from being fluid dominated, to magnetically dominated. Whether a plasma is fluid or magnetically dominated depends on the ratio of its fluid pressure,  $p$ , to its magnetic pressure,  $p_{\text{mag}}$ , or plasma beta, where,

$$\beta = \frac{p}{p_{\text{mag}}} = \frac{n k_B T}{B^2 / 2\mu_0}, \quad (1.1)$$

and  $n$  is the plasma density,  $T$  its temperature, and  $B$  the magnetic field strength. A plasma with  $\beta > 1$  can be manipulated by fluid motion, as is the case in the photosphere and below. As plasma density decreases in the chromosphere and beyond, areas with strong magnetic field strength have  $\beta < 1$ . In this portion of the atmosphere the magnetic field dominates and magnetic field motions begin to dictate plasma motion (Priest, 2014).

In the solar atmosphere, the magnetic field is complicated and continuously evolving. Fluid motions in the photosphere, driven by the convection and differential rotation, shuffle the base of magnetic loops and open filed lines, known as foot points, changing the field above. Also, new magnetic field lines are constantly being brought to the surface, a process called flux emergence, that interact with the field above. As the magnetic field is shuffled around, and interacts with emerging flux, it is twisted and tangled gaining energy, until, somewhat

suddenly instability sets in. These instabilities allow the magnetic field lines to reconfigure themselves into a lower energy state, a process referred to as magnetic reconnection (Parker, 1957; Petschek, 1964). When field lines reconnect, energy stored in the magnetic field is quickly converted to kinetic energy, and plasma is accelerated to velocities much greater than would be possible through thermal means. The velocity at which waves travel along magnetic field lines, which occurs post reconnection, is known as the Alfvén speed. In areas of strong magnetic field the Alfvén velocity can be an order of magnitude faster than the local sound speed in the plasma (Priest, 2014), which is the fastest speed a wave can travel via fluid processes. Observations of velocities much greater than the sound speed during solar eruptions indicate the important role of the magnetic field and magnetic reconnection. Also, the correlation between areas of strong magnetic field and eruptive activity, with the hotter parts of the corona, make the solar magnetic field a strong candidate for the excess temperature of the solar atmosphere.

### How do we study the solar atmosphere?

Much of what we know about the sun comes from examining the light it produces. We collect light from the sun using a variety of techniques, and from it can determine things like plasma temperature, density, velocity, and elemental content, as well as the magnetic field strength. All of this information can then be pieced together to form a more complete picture of solar events so that we can better inform and test our models and understanding.

The solar atmosphere, being a plasma, consists of charged particles including free electrons and ions. As electrons and ions interact and collide, they experience changes in kinetic energy. These collisions conserve energy, so any energy not stored in the kinetic energy of the particles is either stored, by exciting bound electrons to higher energy states, or released in the form of radiation. Energy is radiated away as a photon, a discrete packet

of light, with a specific wavelength,  $\lambda$ , where the energy,

$$E = \frac{hc}{\lambda}, \quad (1.2)$$

$h$  is Plank's constant, and  $c$  is the speed of light. Therefore, by measuring the wavelength of a photon, we know its energy. Energy stored in an ion's bound electron is also eventually emitted as a photon when the bound electron transitions from an excited state, to a more stable one. Since these transitions occur in distinct steps, the wavelength of a measured photon can also tell us what kind of ion produced it. Since ions in the solar plasma are often moving, either because of thermal motions or changes in the magnetic field, the wavelength of emitted photons are often Doppler shifted. Just as train whistle sounds higher or lower pitched depending on if the train is moving toward or away from you, emitted photons have shorter or longer wavelengths depending on the ions velocity. Slight deviations from a photons expected wavelength tell us the ion's velocity,

$$v = c \frac{\lambda - \lambda_0}{\lambda_0}, \quad (1.3)$$

where  $\lambda$  is the measured wavelength and  $\lambda_0$  is the emitted wavelength at zero velocity. Photons of shorter wavelength are referred to as blue shifted, an analogy to visible light, and longer wavelengths red shifted. In solar physics the convention is to define the positive direction as away from us and toward the sun, therefore blue shifted photons have negative velocity and are traveling toward us, and red the opposite.

Radiation emitted from the sun, referred to as the solar spectrum, spans a massive range of wavelengths from gamma rays (picometers) to radio waves, with it's peak emission being visible light ( $\approx 400 - 700$  nm) (Judge, 2020). While the solar spectrum is broadly peaked around visible light, zooming in reveals many smaller peaks and dips at various wavelengths (Figure 1.2). These peaks and dips are from ions emitting or absorbing photons

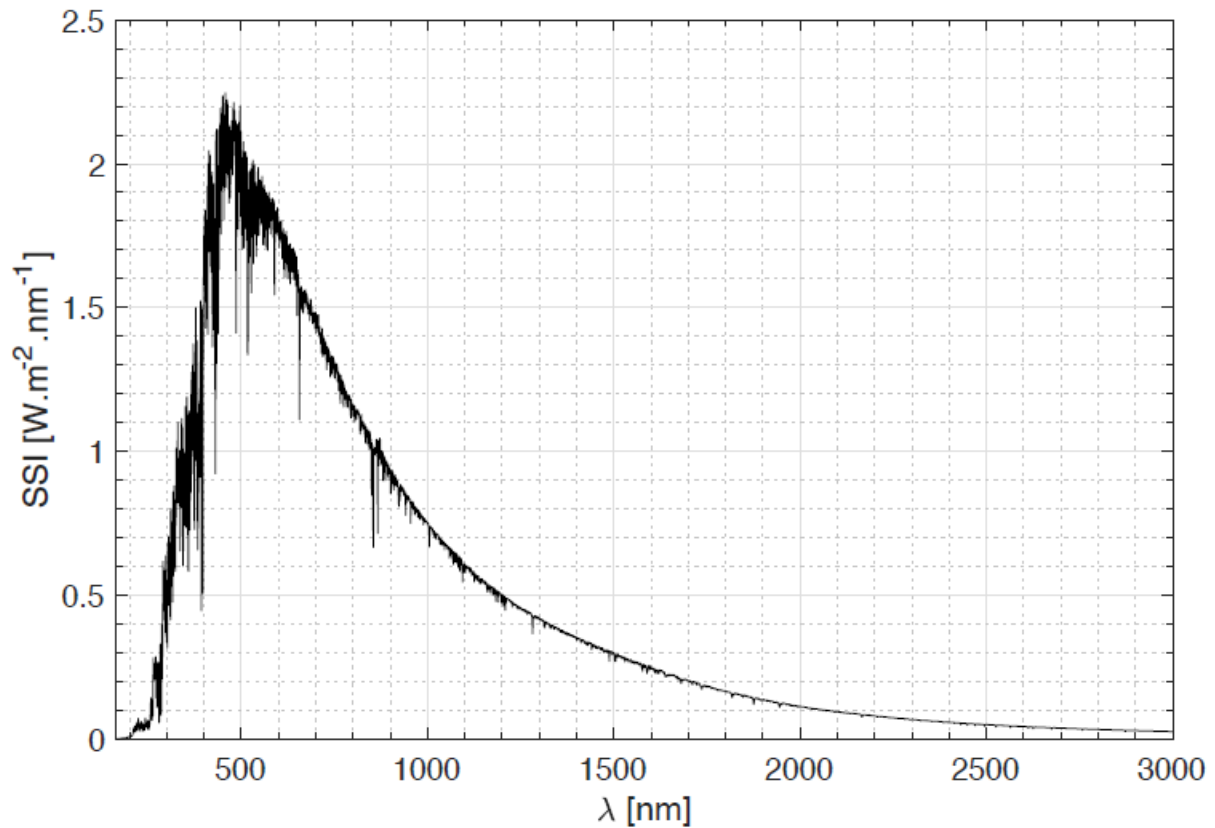


Figure 1.2: The solar spectrum captured in April 2008 by the Solar instrument onboard the International Space Station. ©CNRS

at specific wavelengths, referred to as spectral lines, are the key to isolating and studying different portions of the solar atmosphere. Using filters we can isolate and image narrow wavelength ranges. Images of the photosphere can be captured from earth, since visible light easily passes through the Earth's atmosphere. In order to image the rest of the solar atmosphere, we image the sun in shorter wavelengths, in which the photosphere is very dim. Also, spectral lines in the ultraviolet and shorter wavelengths tend to be optically thin, meaning emitted photons aren't readily absorbed by adjacent ions once emitted. This allows us to image deeper layers in the solar atmosphere.

Shorter wavelengths, from ultraviolet to x-ray, are readily absorbed by the Earth's atmosphere, and therefore must be imaged from space. The currently operating Atmospheric Imaging Assembly (AIA: Lemen et al., 2012) on board the Solar Dynamics Observatory (a satellite with multiple solar instruments), uses narrow filters to image the sun in several different Extreme Ultraviolet (EUV) wavelength ranges aimed at isolating bright spectral lines emitted by the solar atmosphere. Figure 1.3 shows four of these images centered around 304 Å, 171 Å, 193 Å, and 335 Å wavelengths. From quantum mechanics we know the dominant spectral lines come from He II, Fe IX, Fe XII, and Fe XVII ions that occur most often at 0.05 MK, 0.63 MK, 1.2 MK, and 2.5 MK respectively. These filtered images allow us to image the solar atmosphere at various heights and temperatures so we can better understand the structure of solar features and events. Unfortunately most filters aren't narrow enough to truly isolate individual spectral lines or portions of them. Therefore in order to increase our spectral resolution we use a different instrument, the spectrograph.

The spectrograph is a fundamental tool for better understanding light coming from the sun. Spectrographs use diffraction gratings to disperse light based on its wavelength, allowing you to examine the spectral content. Typically light traveling through a spectrograph will be focused through a slit, a very narrow strip for light to travel through, prior to being dispersed by a diffraction grating. These are referred to as slit spectrographs. When used to image

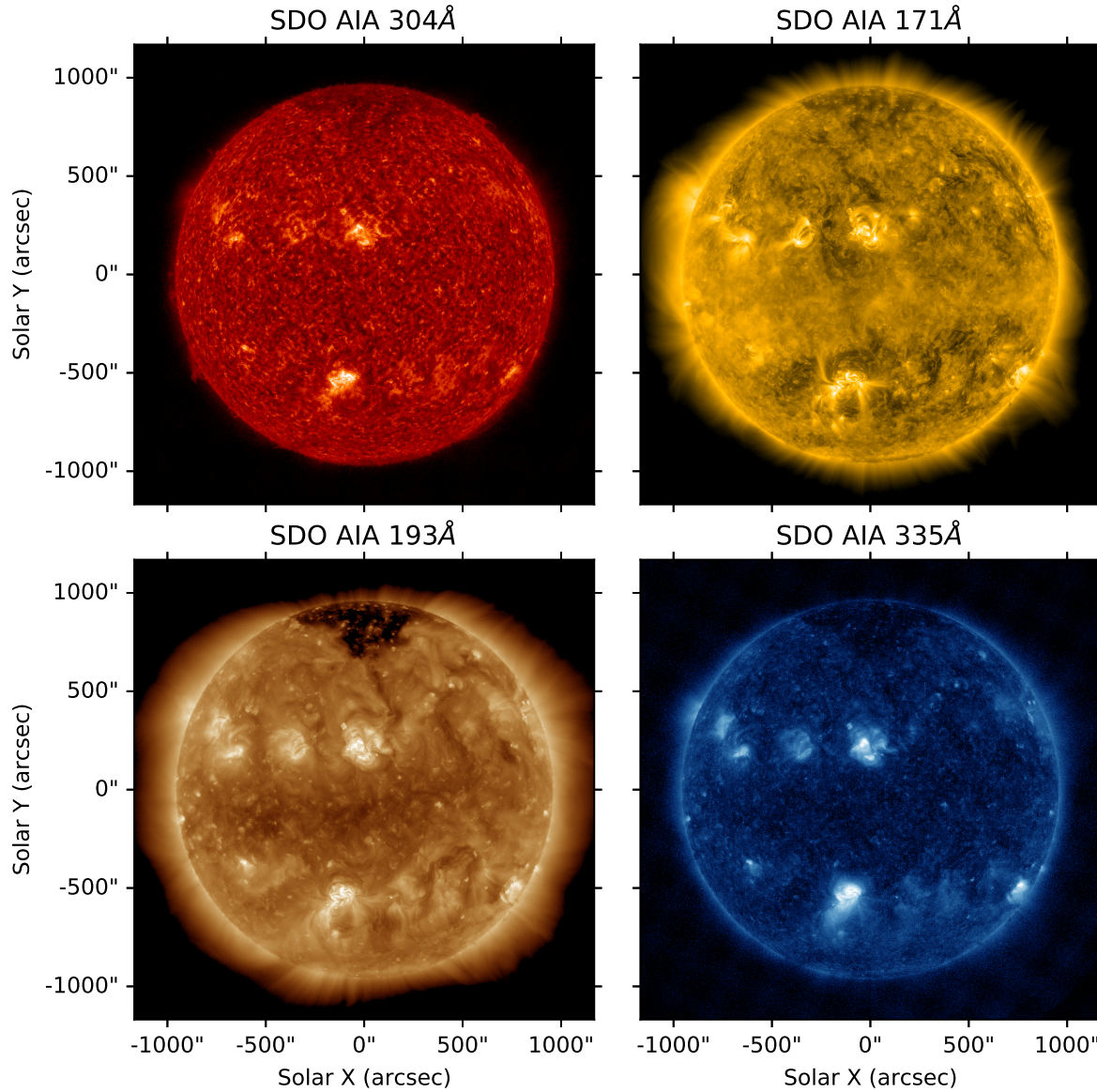


Figure 1.3: Extreme Ultraviolet images from four different AIA channels. Narrowband images of the sun allow us to study different layers of the solar atmosphere by isolating wavelengths from emission lines known to form most often at specific temperatures. These images are displayed in log scale to increase contrast and the color tables are synthetic (since these are not visible light images) and assigned by the instrument team.

the sun, this results in an image of practically pure spectral signal over taken from a very narrow strip of sun in the direction perpendicular to the slit. The Interface Region Imaging Spectrograph (IRIS: De Pontieu et al., 2014) is a currently operating satellite based slit spectrograph imaging the sun. Slit spectrographs like IRIS build spectrally resolved images, an image of the sun with spectral information at every pixel, by scanning the slit over a wider field of view, referred to as rastering. Images from a rastered slit spectrograph can achieve very high spatial and spectral resolution over a decent size field of few. For example, a large IRIS raster has a .33 arcsecond spatial resolution and  $\approx 3 \text{ km s}^{-1}$  per pixel spectral resolution over a  $\approx 2 \times 3$  arcminute field of view (De Pontieu et al., 2021). The down side of rastering a slit spectrograph is that a full exposure is required at every position, which with the current sensitivity of IRIS, takes  $\approx 10$  s per exposure. This results in a spectrally resolved image taken over the course of  $\approx 50$  minutes for a 320-step raster. For more static solar scenes, with less activity, this trade off can have little effect. Unfortunately, many solar eruptions evolve on second timescales, causing the scene to constantly change as you try to image it, often resulting in the slit being pointed away from an area of interest.

An alternate approach is to remove the slit, and disperse an image over a much larger field of view using a diffraction grating, often referred to as a slitless spectrograph. Images from a slitless spectrograph have overlapping spatial and spectral information in every pixel. Therefore, in order to capture a spectrally resolved image of the sun, images from multiple slitless spectrograph channels need to be combined and ‘inverted’ (e.g. Kak & Slaney, 2001). These instruments, referred to as Computed Tomography Imaging Spectrographs (CTIS: Descour & Dereniak, 1995), use the same principle as a CT (Computed Tomography) scan in a doctors office that combine a series of unique two dimensional images taken from different angles, to form something three dimensional. The primary difference between a CTIS instrument and a CT scan is that the goal of a CT scan is the capture a data cube with three spatial dimensions,  $I(x, y, z)$ , whereas a CTIS instrument returns a cube with two

spatial dimensions and one spectral dimensions,  $I(x, y, \lambda)$ . Compared to slit spectrographs, CTIS instruments can capture spectrally resolved images over wide fields of view at much a much faster cadence, but introduce spatial-spectral ambiguity in each image which can be difficult to disentangle. The Multi-Order Solar Extreme Ultraviolet Spectrograph (MOSES: Fox et al., 2010) and Extreme ultraviolet Snapshot Imaging Spectrograph(ESIS: Smart et al., 2021), are two CTIS instruments developed at Montana State University. Data from both instruments are used in this thesis.

### Thesis Outline

The content of this thesis is divided into three chapters. While the projects described in each chapter are unique, they all share a common thread, the transition region. The transition region is a fascinating area of solar study for a couple reasons. First, all mass and energy moving between the chromosphere and corona travels through the transition region. By tracking mass and energy flux between the upper and lower solar atmosphere we can better track how the corona is heated and observe the types features and events associated with that heating. Second, the transition region is where the solar atmosphere becomes magnetically dominated and is littered with magnetically driven phenomena. Eruptions of the transition region are often much smaller than the large flares of the corona, which makes them more difficult to spatially resolve, but they are also more frequent, making it easier to capture them with limited field of view instruments, and build statistics on their nature. Also, since these events occur more frequently, it is much easier to capture them with a sounding rocket based instrument that only has five minutes to image the sun. The transition region is also very thin, making it easier to pinpoint the location of photon emission and form a clearer picture of the geometry of a spatially resolved event. The primary instruments used in the following studies (IRIS, MOSES, and ESIS) all aim measure intensity and velocity at various heights in the transition region. The following chapters describe unique measurements of the

transition region and discuss their possible implications on our understanding of the sun.

The first chapter develops a model of magnetic reconnection used to describe the observation of elliptical motion in a flare ribbon observed by Brannon et al. (2015). On April 18, 2014 IRIS observed an M-class flare with a sit-and-stare that captured one of two flare ribbons. Brannon et al. (2015) observed a sawtooth pattern that propagated along the ribbon with a phase velocity of  $\approx 15 \text{ km s}^{-1}$ . This motion resulted in oscillations in both velocity ( $\pm 20 \text{ km s}^{-1}$ ) and intensity along the slit ( $\pm .5 \text{ arcseconds}$ ) that were 180 degrees out of phase. Using a model of the Tearing Mode instability (Furth et al., 1963a) occurring in a reconnecting current sheet across which there is also velocity shear, we were able to reproduce the oscillations in velocity and intensity, as well as the phase velocity of the wave. We also propose a magnetic geometry and local plasma conditions for the flare that support this hypothesis.

The second chapter describes a method used to quantify the total spectral content in images from the first flight of MOSES. Early work on MOSES data revealed solar features that could not be attributed to the principal wavelength in the passband, He II 304 Å, or other obvious sources of contamination. We also found signatures of this contamination in the mean cross-correlation of MOSES difference images. In order to identify and quantify this contamination, we fit synthetic MOSES images with known spectral content to the actual MOSES images. Synthetic MOSES images were formed from images captured by the Extreme-ultraviolet Imaging Telescope (EIT: Delaboudinière et al., 1995) and synthetic spectra from the Chianti database (Del Zanna & Young, 2020; Dere et al., 1997). The best fit synthetic data was found by varying the average Differential Emission Measure (DEM) over the MOSES field of view used to create the synthetic spectra until the difference between the MOSES and synthetic difference image cross-correlation was minimized. We also comment on the elements of the MOSES design that led to this contamination and confusion, and how it might be improved for similar instruments in the future.

The third chapter explores data from the first flight of the ESIS sounding rocket launch. ESIS improves on the design of MOSES by adding an additional channel (with room for up to six in future flights), and an intermediate focal plane with a field stop that more clearly defines its field of view. During its roughly 5 minutes of observing time ESIS captured tens of small solar eruptions, referred to as explosive events (Dere et al., 1989), and one larger jet ( $\approx 20'' \times 40''$ ) over the  $\approx 11.5$  arcminute field of view. We describe how the unique images were prepared into multiple data levels, and both a qualitative and quantitative approach to understanding the data. Using the dominant spectral line in the ESIS passband, O V 630 Å, we demonstrate how the difference between features in O V captured by different ESIS channels can be used to “read off” qualitative information about an event’s velocity, and its evolution in time. We also use a Multiplicative Algebraic Construction Technique (MART: Okamoto & Yamaguchi, 1991; Verhoeven, 1993) to combine data from all four ESIS channels and invert two different explosive events and show their evolution.

Finally, following these three chapters, I summarize the discussion and conclusions from each chapter and offer some thoughts on the impact of this work, and implications for future studies in solar physics.

MODELING A PROPAGATING SAWTOOTH FLARE RIBBON AS A TEARING  
MODE IN THE PRESENCE OF VELOCITY SHEAR

Contribution of Authors and Co-Authors

Manuscript in Chapter 2

Author: Jacob Parker, Montana State University

Contributions: Implemented and applied model, wrote sections two and three as well as contributed to the introduction and conclusion.

Author: Dana Longcope, Montana State University

Contributions: Proposed the model for this observation and assisted in constructing the model, as well as contributed to the introduction and conclusion.

Manuscript Information

Jacob Parker and Dana Longcope

Status of Manuscript:

- Prepared for submission to a peer-reviewed journal
- Officially submitted to a peer-reviewed journal
- Accepted by a peer-reviewed journal
- Published in a peer-reviewed journal

Astrophysical Journal, Volume 847

DOI: 10.3847/1538-4357/aa8908

Abstract

On April 18, 2014 (SOL2014-04-18T13:03) an M-class flare was observed by IRIS. The associated flare ribbon contained a quasi-periodic sawtooth pattern that was observed to propagate along the ribbon, perpendicular to the IRIS spectral slit, with a phase velocity of  $\sim 15 \text{ km s}^{-1}$  (Brannon et al., 2015). This motion resulted in periodicities in both intensity and Doppler velocity along the slit. These periodicities were reported by Brannon et al. (2015) to be approximately  $\pm 0.5$  arcseconds in position and  $\pm 20 \text{ km s}^{-1}$  in velocity and were measured to be  $\sim 180^\circ$  out of phase with one another. This quasi-periodic behavior has been attributed by others to bursty or patchy reconnection (Brosius & Daw, 2015; Brosius et al., 2016) and slipping occurring during three-dimensional magnetic reconnection (Li et al., 2016; Li & Zhang, 2015). While able to account for periodicities in both intensity and Doppler velocity these suggestions do not explicitly account for the phase velocity of the entire sawtooth structure, or for the relative phasing of the oscillations. Here we propose that the observations can be explained by a tearing mode instability occurring at a current sheet across which there is also a velocity shear. Using a linear model of this instability we reproduce the relative phase of the oscillations, as well as the phase velocity of the sawtooth structure. We suggest a geometry and local plasma parameters for the April 18 flare which would support our hypothesis. Under this proposal the combined spectral and spatial IRIS observations of this flare may provide the most compelling evidence to date of a tearing mode occurring in the solar magnetic field.

Introduction

Chromospheric flare ribbons, observed in many flares, are believed to provide indirect evidence of magnetic reconnection occurring in the corona above. The most widely cited interpretation of these elongated ribbons of chromospheric emission is the CSHKP model

(Carmichael, 1964; Hirayama, 1974; Kopp & Pneuman, 1976; Sturrock, 1968). It holds that an eruption has opened magnetic field lines in regions of opposite sense, and the resulting regions are temporarily separated by a current sheet (CS). Reconnection at this CS creates closed field lines which subsequently retract downward to form the post-flare arcade. The reconnection and retraction energizes those field lines which have been reconnected, and that energy is deposited into the chromosphere to produce the observed emission. The elongated ribbon-like structure thereby maps out, in the chromosphere, the locus in the corona at which reconnection is occurring; it is an image of the CS.

The structure and motions of flare ribbons have provided great insight into the manner in which magnetic reconnection occurs in solar flares. Spreading motion perpendicular to the CS has been used to infer the progress of reconnection and to measure the reconnection electric field (Forbes & Priest, 1984; Isobe et al., 2005; Poletto & Kopp, 1986; Qiu et al., 2002, 2004). Other motions, either parallel to the ribbon, or less orderly, provide evidence of reconnection more complicated than in simple two-dimensional models (Fletcher et al., 2004; Li & Zhang, 2015; Qiu, 2009; Warren & Warshall, 2001). The detailed, fine structure of the flare ribbons has also been used as evidence of complex structure within the CS itself (Nishizuka et al., 2009).

Recent UV spectral and imaging observations of flare ribbons at extremely high spatial resolution, made by IRIS (De Pontieu et al., 2014), have revealed distinctive quasi-periodic, sawtooth patterns in certain flare ribbons (Brannon et al., 2015; Brosius & Daw, 2015; Brosius et al., 2016; Li & Zhang, 2015). These may offer a new clue to some facet of magnetic reconnection. At the moment, however, there are several competing hypotheses about the cause of these small-scale sawtooth patterns in the flare ribbon. The pattern was first reported by Li & Zhang (2015) based on IRIS observations of the ribbons of the 2014 Sep 10 flare (SOL2014-09-10T17:45). They interpreted it as a signature of quasi-periodic slipping, generated by a mode of three-dimensional reconnection (Aulanier et al., 2006).

A similar pattern was observed by Brannon et al. (2015) and Brosius & Daw (2015) in the ribbons of the 2014 April 18 flare (SOL2014-04-18T13:03). Brosius & Daw (2015) and subsequently Brosius et al. (2016) noted that individual pixels on the IRIS slit exhibited quasi-period brightenings and Doppler shifts at  $\sim 3$  minute intervals in a number of spectral lines observed by IRIS as well as *Hinode* EIS. They attributed this quasi-periodic behavior to a bursty or patchy mode of magnetic reconnection.

Brannon et al. (2015, hereafter called BLQ) studied the same flare as Brosius & Daw (2015) but reached a different conclusion about the cause of the quasi-periodic phenomena. They studied both the 1394Å and 1403Å spectral lines of Si IV ( $T \simeq 80,000$  K), over a range of positions along the spectral slit, as well as the sequence of 1400Å slit-jaw images (SJIs), showing mostly the same Si emission. The SJIs clearly revealed the sawtooth pattern in the flare ribbon with a spatial period of approximately  $\lambda_{\text{st}} = 1.8$  Mm (roughly 2 arc seconds) shown here in Fig. 2.1. They also reported that the pattern seemed to propagate *along the ribbon* with apparent speed of  $v_{\text{st}} \simeq 15 \text{ km s}^{-1}$  (denoted in Fig. 2.1 as  $v_0/2$ ). This parallel pattern speed was super-imposed on the much slower,  $1\text{--}2 \text{ km s}^{-1}$ , outward motion of the ribbon itself (southward in Figure 2.1). As the pattern moved across the slit, it caused the point of peak intensity to move up and down at  $\sim 20 \text{ km s}^{-1}$ , with the  $\sim 3$  minute period. This apparent motion of the bright ribbon along the slit resulted in the quasi-periodic brightening *of a fixed pixel position* reported by Brosius & Daw (2015).

BLQ successfully fit each Si IV spectral line with two Gaussians in about about 80% of the ribbon's pixels. The central positions of each Gaussian component oscillated in time, redward and then blueward. The bluer of the two components oscillated about a small mean velocity, and therefore showed red shifts followed by blue shifts of  $\pm 20 \text{ km s}^{-1}$ . The measurement of this secondary bluer component, as well as the phase velocity of the sawtooth feature, is the fundamental difference between the interpretation in this work and previous studies. Brosius & Daw (2015) calculated Doppler velocities by finding the centroid of

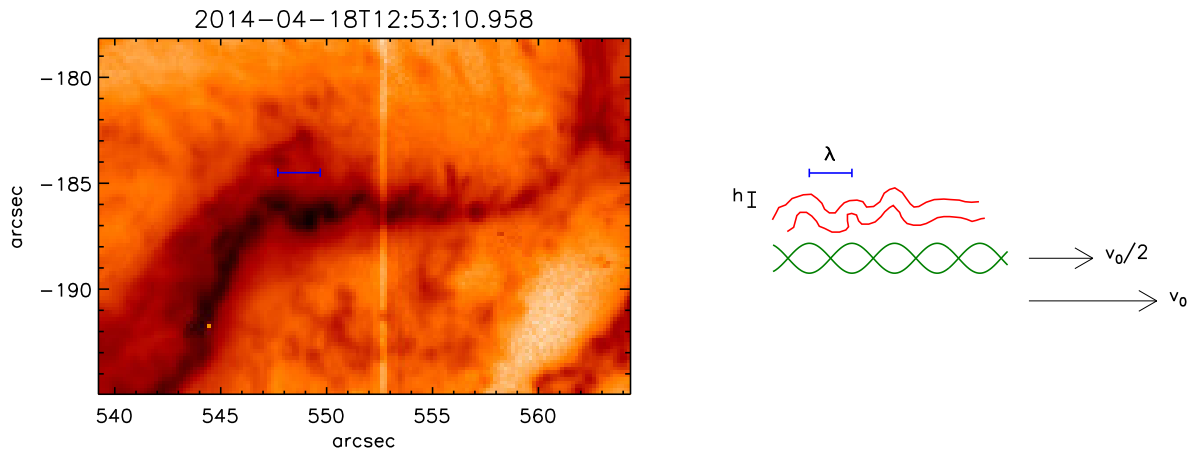


Figure 2.1: A frame from the IRIS 1400Å SJI showing the flare ribbon from the 2014 Apr 18 flare. A subsection of the full SJI is shown on the left using inverse log-scale, with axes marked in arcseconds from disk center. The dark horizontal band is the flare ribbon, and a lighter vertical line at  $x = 552.7$  arcseconds is IRIS's spectrographic slit. An outline of the ribbon is reproduced in red on the right, along with notations showing the spatial period,  $\lambda$ , amplitude,  $h$ , and pattern velocity,  $v_0/2$ . A green island-chain shows the proposed orientation of the tearing mode instability, displaced southward for clarity by a distance greater than proposed in the model. A second velocity arrow shows the direction of the proposed shear velocity,  $v_0$ , which causes the island chain to move at  $v_0/2$ .

various line profiles, a procedure that might mask the Doppler velocities of the separate components. The redder component oscillated about central value  $\sim 40 \text{ km s}^{-1}$ , presumably from explosive chromospheric evaporation (Fisher et al., 1985). In both cases the velocity shift was approximately  $180^\circ$  *out of phase* with the position shift: it was bluest when the pattern had reached its northern most point on the slit. This phase relation is depicted in Fig. 11 of BLQ, which we reproduce here in Fig. 2.2. It is especially clear in a single oscillation, highlighted in the bottom panel, that the velocity *vs.* position curve forms a diagonal line ( $180^\circ$  phase difference) rather than an ellipse ( $90^\circ$  phase difference).

Since the Apr 18 flare occurred some  $40^\circ$  from disk center, plasma motion which is horizontal at the solar surface would produce Doppler shifts as well as motion along the slit (BLQ). Kinematics of linear motion dictate that position and velocity oscillate  $90^\circ$  out of phase from one another. To explain the observed phasing BLQ proposed that the plasma was moving in *horizontal ellipses*, so its two orthogonal components were  $\sim 90^\circ$  out of phase with one another. In that case the velocity of one component (the line-of-sight) would be  $\sim 180^\circ$  out of phase with the *position* of the other (position along the slit), in agreement with the observations.

BLQ went on to observe that elliptical fluid motions occur in a number of well-known, large-scale instabilities occurring at some kind of surface or interface. The classic Kelvin-Helmholtz instability (KH, Chandrasekhar, 1961) and the tearing mode (TM, Furth et al., 1963b), both occur at interface surfaces (a velocity shear layer and a CS respectively) and therefore have eigenmodes which are periodic along the interface and decay exponentially away from it. Such a structure in the velocity stream function naturally produces elliptical fluid motions. Indeed, a simple surface gravity wave (a.k.a. an *f*-mode) is well-known for its elliptical motions. BLQ therefore proposed that the quasi-periodic oscillation they observed in the flare ribbon was a manifestation of some form of surface-confined instability such as the KH or TM.

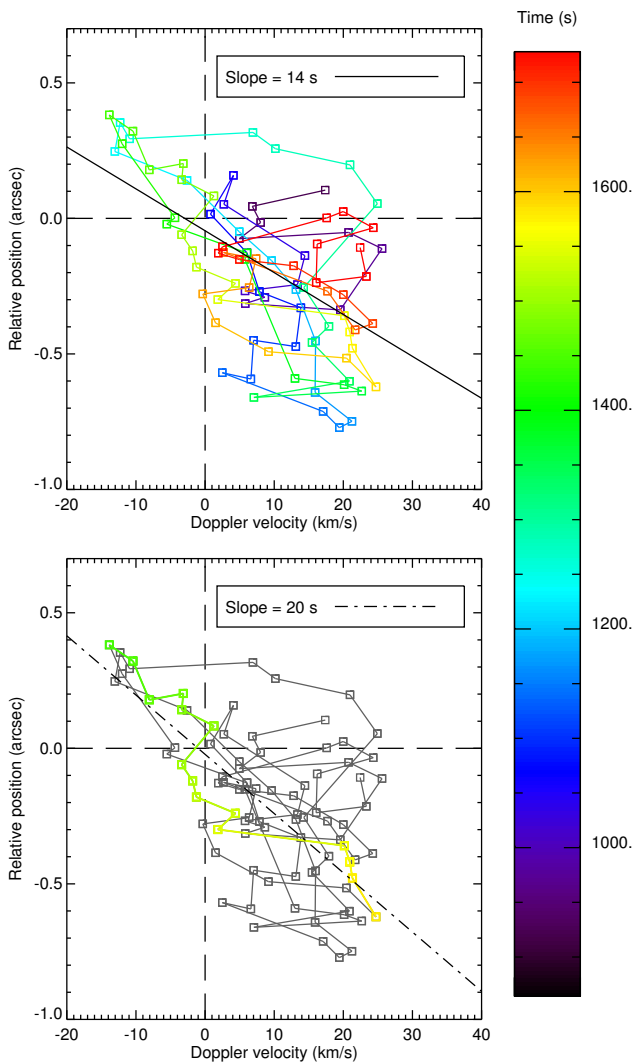


Figure 2.2: Figure 11 from BLQ reproduced with permission. The upper panel shows the mean Doppler velocity of the blue component of the Si IV lines, plotted against the mean position of the sawtooth pattern along the slit. Time is indicated by color, coded in the bar along the right. The bottom panel repeats this, but highlights in color one of the best defined oscillations.

Both the KH and TM instabilities have been the subjects of extensive study, and have been previously invoked in numerous roles in solar phenomena. Si IV line profiles with bright cores and broad wings have been associated with TM island formation, “plasmoids”, during small scale reconnection and transition region explosive events (Innes et al., 2015). Plasma blobs imaged by AIA (Lemen et al., 2012) have been observed to occur in the current sheet above a flare arcade (Takasao et al., 2012; Takasao et al., 2016) and in coronal bright points (Zhang et al., 2016). These plasma blobs are thought to be the result of magnetic islands generated by the TM instability. Wave-like structures observed on the edge of erupting coronal structures (Foullon et al., 2011, 2013; Ofman & Thompson, 2011) with various phase velocities have been attributed to the KH instability. Most attributions to the TM and KH instability rely on appearance alone. While we trust that those attributions are correct, we hope to show that the spatial and spectral IRIS observations of April 18 provide a more quantitative link between observation and model.

Either instability, in its distinct, traditionally-studied form, faces significant challenges in explaining the quasi-periodic pattern observed in the Apr 18 flare ribbon (BLQ). For shear in a magnetized plasma to undergo KH instability the velocity difference across the shear layer must exceed the component of Alfvén speed parallel to the flow difference (Chandrasekhar, 1961). The magnetic field strength near the ribbon was  $\simeq 150$  G, leading to an Alfvén speed  $v_A \sim 10,000 \text{ km s}^{-1}$ , some 500 times greater than any of the observed flow speeds. While only a fraction of that field strength will be directed parallel to the flow, it seems extremely unlikely that the fraction could be as small as 0.2%.

Tearing modes, on the other hand, are well known features in CSs. They will be unstable if the plasma resistivity is low enough that the Lundquist number, computed with respect to the thickness of the CS, exceeds  $S \sim 10^4$  (Biskamp, 1986). Classical resistivity and a Sweet-Parker CS result in values as large as  $S \sim 10^8$ . The instability will produce elliptical motions, but at speeds lower than the Alfvén speed by an inverse fractional power of  $S$ .

Depending on the value of  $S$ , and on the value of the inverse power (this depends on other factors as well), that might be well below the  $20 \text{ km s}^{-1}$  flow speeds observed. Furthermore, the traditional TM analysis, set in an otherwise stationary CS, does not predict a phase velocity with which we might associate the observed pattern speed of  $v_{\text{st}} \simeq 15 \text{ km s}^{-1}$ .

In the present work we show that when a steady sub-Alfvénic velocity shear occurs across a CS the modified TM instability can achieve higher flow speeds *and* exhibit a significant phase velocity. Indeed, the two speeds will generally be comparable, as they were observed to be in the Apr 18 flare. We find that such a combined KH/TM instability is compatible in many respects with the observations reported by BLQ. We therefore propose that the flare of 2014 Apr 18 provides evidence of a TM-like instability occurring at its CS.

While many previous studies of the TM have been set at a static CS (Furth et al., 1963b; Pucci & Velli, 2014; Steinolfson & van Hoven, 1983; Velli & Hood, 1989), several notable exceptions did include an equilibrium shear flow (Chen et al., 1997; Doss et al., 2015; Einaudi & Rubini, 1986; Li & Ma, 2010; Ofman et al., 1991; Ofman et al., 1993; Zhang et al., 2011). Those analyses focused their attentions on effects the shear had on the growth rates of the instabilities. We repeat these previous analyses here in order to compute the amplitude and structure of the eigenmode's velocity field. A simple linear model allows us to easily generate flow structures while minimizing free parameters thereby permitting us to explore a wide swath of parameter space. From this we are able to synthesize the position and Doppler signature of a plasma element. We find these reproduce reasonably well the aspects of the Apr 18 observation described above. We propose that there was a horizontal bulk plasma motion of  $v_0 \simeq 37 \text{ km s}^{-1}$  on the open-field (unreconnected) side of the flare ribbon and no flow on the other (post-reconnection) side, as indicated in Fig. 2.1. In this configuration any tearing mode in the CS will propagate with a phase speed of  $v_0/2 \simeq 18.5 \text{ km s}^{-1}$ , the average of the far field equilibrium shear flows, as observed (Doss et al., 2015). The fluid elements on the stationary side of the CS will then undergo elliptical motion, with similar

velocity, about a fixed central point. Since this is the post-reconnection side, it harbors the energized ribbon and is the plasma whose emission we observe. This, we believe, was what occurred and was observed by IRIS on 2014 Apr 18. If so, it provides a novel observational characterization of a tearing mode and the CS hosting it. It may offer the most compelling evidence to date of a tearing mode occurring in the solar magnetic field.

We present our analysis and support our conclusion as follows. In the next section we reprise the linear eigenmode calculation for tearing modes at a CS at which there is also an equilibrium shear flow (Einaudi & Rubini, 1986; Ofman et al., 1991); they are a form of combined TM/KH mode. We forgo discussion of growth rates and focus instead on the structure of the velocity fields of the eigenmodes which were not thoroughly presented by previous investigators. Then in Sec. 3 we propose a geometry in which such an instability might have occurred in the 2014 Apr 18 flare. We synthesize the observations which would result from such a scenario. The synthesized observation compares favorably to the observations reported by BLQ, and to Fig. 2.2 in particular. Finally, in Sec. 4 we discuss the significance of our proposed explanation.

### Linear Tearing Mode Instability with Shear Flow

Since the first publication on the linear tearing mode instability in resistive plasmas (Furth et al., 1963b, FKR) many investigators have found solutions to the eigenvalue problem numerically. These numerical studies tested the validity of assumptions used to find the instability growth rates and scaling relations analytically (Steinolfson & van Hoven, 1983). They also examined the effects of extra terms in the governing equations, different coordinate systems, and boundary conditions on instability growth (Ofman et al., 1991; Velli & Hood, 1989). We repeat this analysis in order to verify the observational effects the TM instability with an asymmetric shear flow. The following solution method has been used in many of those previous investigations (Killeen, 1970; Ofman et al., 1991; Steinolfson & van Hoven,

1983) and is included here for completeness.

For our analysis we use the two-dimensional, incompressible, resistive magnetohydrodynamic (MHD) equations. The TM instability is governed by the resistive induction equation,

$$\frac{\partial \mathbf{B}}{\partial t} = \nabla \times (\mathbf{u} \times \mathbf{B}) - \nabla \times (\eta \nabla \times \mathbf{B}) , \quad (2.1)$$

vorticity equation,

$$\frac{\partial(\nabla \times \mathbf{u})}{\partial t} = \nabla \times \left\{ \frac{1}{4\pi\rho_0} (\nabla \times \mathbf{B}) \times \mathbf{B} - (\nabla \times \mathbf{u}) \times \mathbf{u} \right\} , \quad (2.2)$$

and condition of incompressibility,

$$\nabla \cdot \mathbf{u} = 0 . \quad (2.3)$$

We also take resistivity,  $\eta$ , and density,  $\rho_0$ , to be uniform.

We linearize these equations about an initial magnetic field,  $\mathbf{B}_0(y)$ , given by the Harris current sheet (Harris, 1962), along with an initial velocity shear profile  $\mathbf{u}_0(y)$ . For simplicity we give the shear profile the same functional form as the magnetic field. In Section 3 we consider an asymmetric velocity shear, however, to simplify analysis in this section we move to a reference frame in which the velocity shear is symmetric: the flow is equal and opposite across the current sheet. In this reference frame, for sufficiently small shear velocity  $V$ , the phase velocity of any instability will be zero. The instability will then be given a phase velocity when, in Sec. 3, we return to the stationary frame of reference. For further simplicity, the thickness,  $a$ , of the current sheet and velocity shear are taken to be the same

$$\mathbf{B}_0(y) = B_0 \tanh(y/a) \hat{\mathbf{x}} , \quad (2.4)$$

$$\mathbf{u}_0(y) = V \tanh(y/a) \hat{\mathbf{x}} , \quad (2.5)$$

where  $B_0$  and  $V$  are the far-field magnitudes of the field and velocity respectively.

We perturb all quantities with first order terms of the form  $f_1(x, y, t) = f_1(y, t) e^{ikx}$ . Using incompressibility to eliminate the  $\hat{x}$  component of  $\mathbf{u}_1$ , the solenoidal magnetic field condition to eliminate the  $\hat{x}$  component of  $\mathbf{B}_1$ , and taking only the  $\hat{z}$  component of the vorticity equation gives a coupled set of second-order linear differential equations. We non-dimensionalize the equations by scaling magnetic field to the asymptotic field strength,  $B_0$ , velocity to the asymptotic Alfvèn speed,  $v_a = B_0/\sqrt{4\pi\rho_0}$ , and lengths to the thickness of the current sheet,  $a$ . The resulting non-dimensional quantities are denoted with over-bars

$$\bar{u} = u_{1y}/v_a, \quad \bar{B} = B_{1y}/B_0, \quad \bar{t} = \frac{tv_a}{a}, \quad (2.6)$$

$$\bar{k} = ka, \quad S = \frac{av_a}{\eta}, \quad \bar{y} = y/a. \quad (2.7)$$

The non-dimensionalized profiles are denoted

$$F(\bar{y}) = \frac{B_{0x}}{B_0} = \tanh(\bar{y}), \quad G(\bar{y}) = \frac{u_{0x}}{v_a} = \bar{V} \tanh(\bar{y}), \quad (2.8)$$

In terms of these, the non-dimensional linearized equations are,

$$\frac{\partial \bar{B}}{\partial \bar{t}} = i\bar{k}(F\bar{u} - G\bar{B}) + S^{-1}\mathcal{L}\bar{B} \quad (2.9)$$

and

$$\frac{\partial \bar{u}}{\partial \bar{t}} = i\bar{k}\{F\bar{B} - G\bar{u} + \mathcal{L}^{-1}(G''\bar{u} - F''\bar{B})\} \quad (2.10)$$

where primes denote derivatives with respect to  $\bar{y} \equiv y/a$ , and we have introduced the linear operator

$$\mathcal{L} = \frac{\partial^2}{\partial \bar{y}^2} - \bar{k}^2, \quad (2.11)$$

whose inverse is denoted  $\mathcal{L}^{-1}$ .

Our velocity variable,  $\bar{u}$ , differs from other presentations of TM eigenfunctions (Ofman et al., 1991; Velli & Hood, 1989) by a factor of  $i$ . Their definition is preferable in the absence of shear flow because our version of  $\bar{u}$  becomes purely imaginary in that case. When shear is present ( $V \neq 0$ ) we find the more symmetric definition of  $\bar{B}$  and  $\bar{u}$ , given in Equation (2.6), to be preferable.

Considering separately the real and imaginary parts of Equations (2.9) and (2.10) gives four equations to advance four independent fields: the real and imaginary parts of  $\bar{u}$  and  $\bar{B}$ . We solve these equations numerically by implicitly integrating all four components forward in time until the fastest growing unstable mode dominates and pure exponential growth sets in at a single, real growth rate  $\bar{\gamma} = \gamma a/v_a$ . At every time step the eigenfunctions are re-scaled to make the largest value of the largest field (typically the real part of  $\bar{B}$ ) unity. The growth rate for that time step is calculated to be

$$\bar{\gamma} = \frac{\ln(\max([\bar{B}, \bar{u}]))}{\Delta t}, \quad (2.12)$$

prior to the solutions being re-scaled.

The solution is said to have converged on the fastest growing mode when

$$\frac{\sum_i |\bar{u}_{i,j} - \bar{u}_{i,j-1}|^2}{\sum_i |\bar{u}_{i,j-1}|^2} < 1 \times 10^{-9}, \quad (2.13)$$

where  $i$  is a spatial index and  $j$  is the time step. The velocity eigenfunction,  $\bar{u}$ , is used to test convergence because it is found to change more over the course of simulation and therefore takes longer to converge. At the point of convergence the last calculated value of  $\bar{\gamma}$  is the growth rate for that mode.

A purely real  $\bar{\gamma}$  and odd equilibrium functions  $F$  and  $G$  mean that the real parts of  $\bar{B}$

and  $\bar{u}$  will be even in  $\bar{y}$  while the imaginary parts will be odd,

$$\text{Re}[\bar{u}(y)] = \text{Re}[\bar{u}(-y)], \quad \text{Im}[\bar{u}(-y)] = -\text{Im}[\bar{u}(y)], \quad (2.14)$$

$$\text{Re}[\bar{B}(y)] = \text{Re}[\bar{B}(-y)], \quad \text{Im}[\bar{B}(-y)] = -\text{Im}[\bar{B}(y)]. \quad (2.15)$$

To enforce these symmetries we set to zero the values of the imaginary parts and derivatives of the real parts of both  $\bar{u}$  and  $\bar{B}$  at  $\bar{y} = 0$ . This permits us to solve in the half space  $\bar{y} \geq 0$ . Any normal modes with a complex growth rate (i.e. non-vanishing phase velocity) will not have these symmetries. In this case all four components of the solution will have both odd and even parts and a solution in full space would be necessary. We do not attempt this in the current study.

Spatial derivatives are computed using a second-order finite differencing scheme on a nonuniform grid. We use a grid from Steinolfson & van Hoven (1983) with spacing prescribed as

$$\Delta\bar{y}_i = \bar{y}_{i+1} - \bar{y}_i = \Delta\bar{y}_{\max} \left\{ \frac{\Delta\bar{y}_{\min}}{\Delta\bar{y}_{\max}} \right\}^{(i_m-i)/(i_m-1)}. \quad (2.16)$$

For our purposes we used a minimum spacing near the origin,  $\Delta\bar{y} = 1 \times 10^{-4}$ , that increases to a max spacing,  $\Delta\bar{y} = .5$ , at grid point  $i_m = 300$ . Beyond this point a spacing of  $\Delta\bar{y}_{\max}$  is maintained to the outer boundary  $\bar{y} = 1000$ .

Our outer boundary condition is set to match the solutions onto the asymptotic analytic solutions to Equations (2.9) and (2.10). There are four asymptotic solutions to these equations, two exponentially growing and two exponentially decaying. One exponential decay solution has a decay rate that is proportional to  $S$  and therefore decays much faster than the other for the large Lundquist number. We assume that this mode is absent far from current sheet and impose the more slowly decaying asymptotic solution as a boundary

condition. This gives

$$\lim_{y \rightarrow \infty} \bar{u}(|y|) \propto e^{-k|y|}, \quad (2.17)$$

$$\lim_{y \rightarrow \infty} \bar{B}(|y|) \propto e^{-k|y|}. \quad (2.18)$$

We implement this numerically by enforcing

$$f(\bar{y}_n) = f(\bar{y}_{n-1})e^{-\bar{k}(\bar{y}_n - \bar{y}_{n-1})} \quad (2.19)$$

at the outer most grid point,  $n$ , for both  $\bar{u}$  and  $\bar{B}$ .

To obtain a single solution we fix  $S$ ,  $\bar{k}$ , and  $V$  and integrate forward in time using a backward Euler method. The time evolution operator for this method does not have explicit time dependence and therefore only needs to be inverted once for every run. Since we are not interested in the time dependent behavior of these solutions a low order integration scheme can be used without loss of accuracy. The stability that comes from integrating implicitly allows for large time steps,  $\Delta \bar{t} \sim 100$ , and leads to very fast convergence in roughly a hundred time steps. The choice of time step and convergence time depend mostly on the choice of  $S$ . Larger time steps can be taken when the growth rate is slower, or for larger  $S$ .

Figure 2.3 shows an example of the eigenfunctions for the TM instability with an equilibrium shear flow  $\bar{V} = 1.5 \times 10^{-3}$ ,  $\bar{k} = \bar{k}_{\max} = 0.0234$ , and  $S = 1 \times 10^7$ . Here  $\bar{k}_{\max}$  is the wavenumber leading to a maximum growth rate for the given value of  $S$ . The magnetic eigenmode is fairly uniform ( $\bar{B} \simeq 0.03$ ) out to about  $\bar{y} \simeq 0.03$ . The velocity eigenmode has structure outside this region, and thus does not conform the the so-called constant- $\psi$  approximation (FKR) frequently used to solve for eigenmodes analytically. This is consistent with the findings of Steinolfson & van Hoven (1983) who found that the maximum growth

rate for a given  $S$  always occurs in an area of parameter space where this approximation is not valid.

To visualize these eigenfunctions we contour the flux function,  $A$ , and stream function,  $\Phi$ , defined to produce the magnetic field and velocity fields

$$\mathbf{B} = \nabla \times A(x, y) \hat{\mathbf{z}} , \quad (2.20)$$

$$\mathbf{u} = \nabla \times \Phi(x, y) \hat{\mathbf{z}} . \quad (2.21)$$

The full value of each consists of an equilibrium and a perturbed contribution

$$A_0 = \ln(\operatorname{sech}(y)) , \quad A_1 = \frac{1}{\bar{k}} \{ \operatorname{Re}(\bar{B}) \sin(\bar{k}\bar{x}) + \operatorname{Im}(\bar{B}) \cos(\bar{k}\bar{x}) \} , \quad (2.22)$$

$$\Phi_0 = \bar{V} \ln(\operatorname{sech}(y)) , \quad \Phi_1 = \frac{1}{\bar{k}} \{ \operatorname{Re}(\bar{u}) \sin(\bar{k}\bar{x}) + \operatorname{Im}(\bar{u}) \cos(\bar{k}\bar{x}) \} . \quad (2.23)$$

The full flux function and stream function consist of the equilibrium contributions added to these perturbations, times a small amplitude  $\alpha$ ,

$$A(x, y) = A_0 + \alpha A_1 , \quad (2.24)$$

$$\Phi(x, y) = \Phi_0 + \alpha \Phi_1 . \quad (2.25)$$

These functions are contoured in Figure 2.4 for  $\alpha = 0.0025$  and three different values of  $\bar{V}$ :  $\bar{V} = 0$ ,  $\bar{V} = 1 \times 10^{-3}$ , and  $\bar{V} = 0.1$ . We choose these model parameters to illustrate the transition of the eigenmodes from zero shear flow to shear flow that is a significant fraction of the Alfvén speed.  $\Phi$  is contoured in red and  $A$  in black. Magnetic field lines follow the black

contours and velocity flow follows the red. Contour spacing is greatly exaggerated and chosen to highlight key features. The magnetic structure in all three cases consists of large magnetic islands separated into two lobes each, with O-points at the lobe centers. These double-lobed islands are separated from one another by X-points located at  $\bar{k}\bar{x} = (4n + 3)\pi/2$ . There is also an X-point at the center of each island,  $\bar{k}\bar{x} = (4n + 1)\pi/2$ , separating the two lobes and their central O-points. Remarkably, the flux functions are virtually indistinguishable in these three cases in spite of their very different shear flows. This is because the imaginary part of  $\bar{B}$  is extremely small compared to its real part, for all values of  $\bar{V}$  we have considered.

With no background shear velocity (Figure 2.4a) flow is into the magnetic X-point on either end of the island along straight vertical paths and out along straight horizontal paths. The horizontal flows then converge on the X-points inside each island. They exit these along vertical paths, filling the separated lobes composing each island. This flow pattern brings new flux into the X-points, where it reconnects, and then moves into the island. Once in the island lines are reconnected a second time to form the two interior island lobes. This flow pattern forms closed stream lines above and below the mid-plane of the current sheet.

In Figure 2.4c  $\text{Im}(\bar{u})_{\max} \ll \bar{V} \ll v_a$ . Shear flow of this speed is incapable of perturbing the magnetic field and is therefore forced to trace the perturbed magnetic field lines over most of eigenmode. This behavior comes out of Equations (2.9) and (2.10) in the limit  $\text{Im}(\bar{B}) \ll 1$  and  $\bar{V} \gg \text{Im}(\bar{u})_{\max}$  where  $\text{Re}(\bar{u}) \rightarrow (G/F) \text{ Re}(\bar{B})$ .

Figure 2.4b shows an intermediate regime,  $\bar{V} \approx \text{Im}(\bar{u})$ , in which streamlines occur in two distinct classes. Far enough from the current sheet streamlines form open contours, following the perturbed field lines and not crossing the current sheet. Closer streamlines, on the other hand, are closed and circulate through magnetic X-points in distorted versions of the closed vortices in the shear-free case (2.4a). The distance from the current sheet where the streamlines transition from open to closed depends on the magnitude of the perturbation  $\alpha$ .

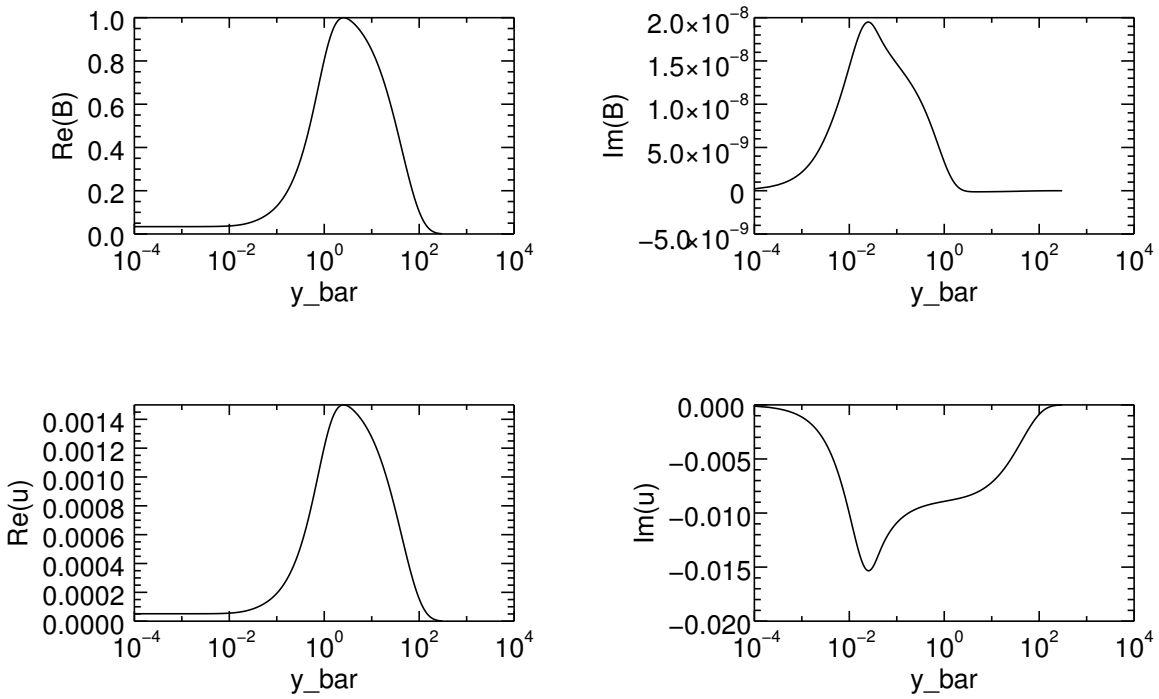


Figure 2.3: The eigenfunction for the most unstable mode with parameters  $S = 1 \times 10^7$ ,  $V = 1.5 \times 10^{-3}$ , and  $\bar{k} = .0234$  plotted along a logarithmic spatial coordinate. This mode has a growth rate  $\bar{\gamma} = 2 \times 10^{-4}$ .

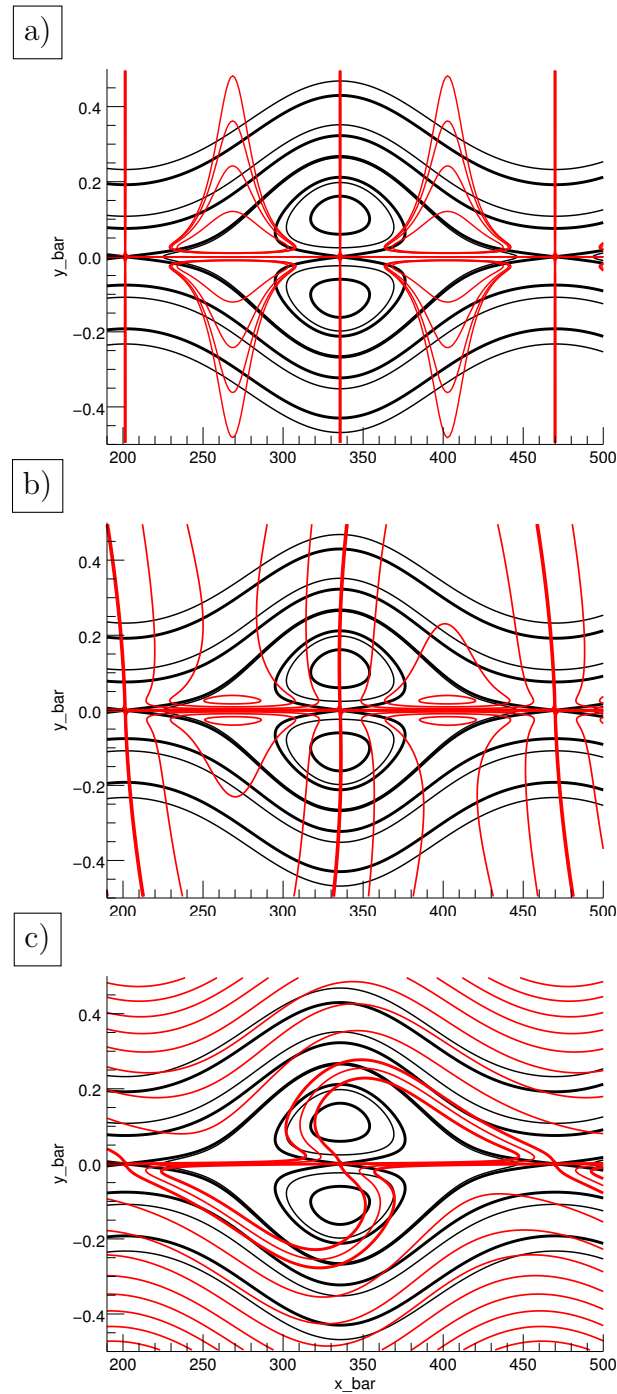


Figure 2.4: Contours of  $\bar{B}$  (black) and  $\bar{u}$  (red) with shear flow  $V = 0, 1.5 \times 10^{-3}, 0.1$  in a,b,c respectively.

The linear model of the TM/KH mode instability outlined above is not new. However, we hope that a more detailed view of the instability eigenmodes, for various values of background shear flow, help illuminate the nature of this combined instability. Repeating the analysis has also allowed us to confirm our conjecture in the following section that the combined TM/KH instability can reproduce the behavior observed by Brannon et al. (2015)

### Modeling Observations

#### Geometry

During the flare observed by IRIS on April 14, 2014 a periodic sawtooth pattern was observed by Brannon et al. (2015) (BLQ) to propagate with a phase velocity of  $15 \text{ km s}^{-1}$  parallel to the ribbon and therefore perpendicular to the IRIS slit. Line of sight (LOS) Doppler measurements of the fluid composing this sawtooth pattern found oscillations with an amplitude of  $\approx \pm 20 \text{ km s}^{-1}$ . These velocities were found to be  $\approx 180^\circ$  out of phase with the position on the slit. The observed behavior is best captured in Figure 2.2. It can also be seen in this figure that the amplitude of the oscillations along the slit are roughly 1 arcsecond. The Tearing/Kelvin-Helmholtz modes described above can produce features consistent with described observation.

We propose that a tearing mode had occurred within a secondary current sheet that had formed along the separatrix legs of the flare arcade. A schematic version of the proposed geometry is shown in Fig. 2.5. This differs from the geometry first put forth by BLQ, who expected the TM to occur within the main current sheet beneath the erupting flux rope. We find that our geometry is able to better match all aspects of the observation.

The secondary current sheet separates newly reconnected arcade field lines from still-open flux connected to the flux rope above. We propose that horizontal motion in this open flux, perhaps persisting from the eruption, creates the the velocity shear as well the magnetic shear which is the current sheet itself. The flux on the other side of this layer, consisting of

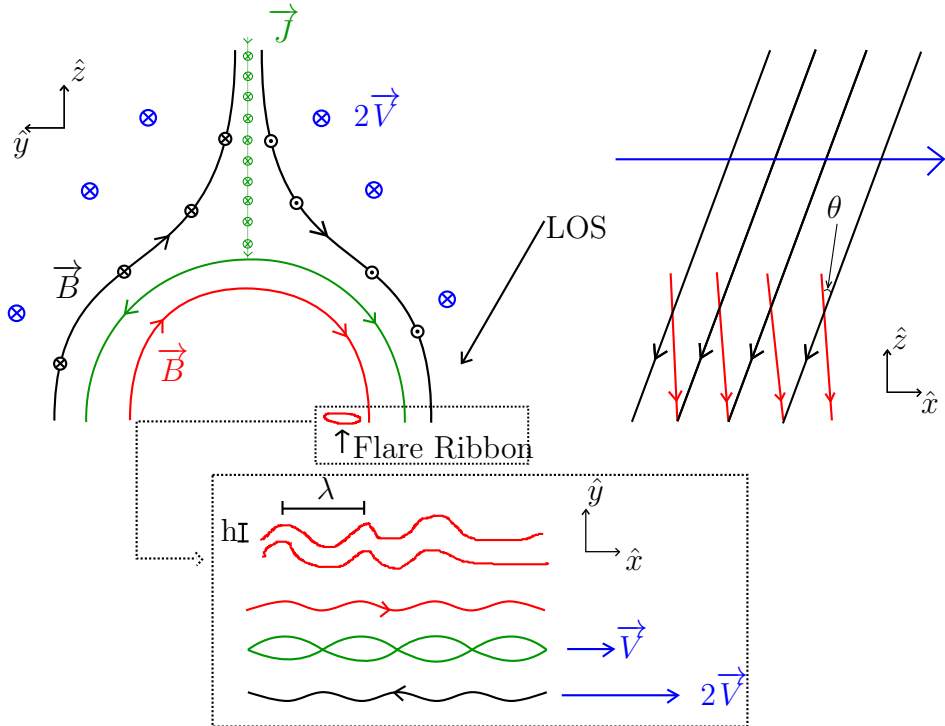


Figure 2.5: In the proposed magnetic field configuration a flow in the  $\hat{x}$  direction,  $\vec{V}$  (blue), deflects overlying magnetic field,  $\vec{B}$  (black), at some angle  $\theta$  to the inner recently reconnected magnetic field,  $\vec{B}$  (red). This results in the labeled currents,  $\vec{J}$  (green). The dashed box shows a blown up region of the secondary current sheet where we model the TM/KH Instability. We also show the LOS of the observation to demonstrate how motion in the x-y plane translates to LOS Doppler velocities.

newly closed arcade field lines, is expected to be stationary and undeflected. These are the field lines in which energy has been deposited, so the ribbon itself should occur *within* this stationary flux, rather than at the secondary current sheet.

The current in the secondary sheet flows *vertically*, so the tearing mode in it will produce a *horizontal* chain of islands, as illustrated in Fig. 2.5. These will deform the magnetic field outside the sheet, and therefore the ribbon. If the tearing mode propagates along the sheet, so will this deformation. We propose that it is this propagating deformation which produces the moving sawtooth pattern in the ribbon.

### Introducing Dimensions

To help constrain parameters we assume that the linear instability has had sufficient time for  $\sim 10$  *e-foldings* during the typical flare time scale of  $t \simeq 100$  s. We therefore set  $\bar{\gamma}\bar{t} \propto 10$ , to obtain the constraint

$$\bar{\gamma} \geq \frac{10a}{(100\text{s})v_a} = \frac{\bar{k}\lambda}{2\pi v_a (10\text{s})} . \quad (2.26)$$

Here  $\lambda$  is the wavelength of the sawtooth pattern from Figure 2.1 along the solar surface. We have no direct measurement of the sheet's thickness,  $a$ , but we can use the observed wavelength,  $\lambda$ , to dimensionalize our expressions. It is thus, in Eq. (2.26), that we use  $\bar{k} = ka = 2\pi a / \lambda$  to formally eliminate  $a$ .

We assume that the horizontal motion of the open flux has deflected it by some small angle, say  $10^\circ$ , relative to the stationary, and undeflected arcade flux. This angular difference,  $\pm 5^\circ$ , produces the tangential discontinuity which is the secondary current sheet. The field strength in the vicinity of the flare ribbon region was estimated by BLQ to be 150 G. The single-sided  $10^\circ$  deflection will therefore produce a reconnecting component of  $150 \sin(5^\circ) = 13$  G. Assuming a typical electron density of  $3 \times 10^9 \text{ cm}^{-3}$ , gives the value  $v_a = 500 \text{ km s}^{-1}$ , which was used in our non-dimensionalization.

The sawtooth pattern is observed to propagate with phase velocity perpendicular to the IRIS slit of  $V' = 15 \text{ km s}^{-1}$ . This was found in the plane-of-the sky (primed coordinates), but applied to motion horizontal motion some  $40^\circ$  from disk center. Foreshortening effects will reduce velocity  $V$ , in the horizontal  $x$  direction, to an apparent velocity

$$V' = V \cos \theta_x . \quad (2.27)$$

where  $\theta_x \simeq 33^\circ$  is the horizontal distance from disk center. The observed phase velocity of  $15 \text{ km s}^{-1}$  thus corresponds to a real horizontal velocity of  $V \simeq 18.5 \text{ km s}^{-1}$ . Scaling this to the reconnection-component Alfvén speed,  $v_a = 500 \text{ km s}^{-1}$  yields  $\bar{V} = 0.037$ .

### The Saturated State

We use these dimensions to construct a synthetic observation from the velocity structure of our model. We do so first using the velocity structure given by the linear eigenmode,  $\Phi_1(x, y)$ , discussed above. We construct the stream function by superposing this using the amplitude,  $\alpha = 1$ , in eqs. (2.24) and (2.25). Figure 2.6 shows magnetic field lines (black) and streamlines (red) of the resulting construction. This specific eigenfunction results from  $S = 10^4$  and  $\bar{k} = .1315$ , which has a growth rate of  $\bar{\gamma} = .00928$  in agreement with (2.26). The green contour shows the trajectory of a fluid element that begins at  $[x, y] = [86, 18]$ .

Because the growing linear eigenmode has been used in the non-linear regime, the stream lines (red) cross the field lines (black) in this construction. The magnetic field evolution implied by continuing island growth requires this cross-field flow in the regions outside the diffusion region. This cross-field flow will naturally cease when the linear phase ends and the island growth ends.

Fully non-linear treatments of the tearing mode, in which island saturation occurs self-consistently, have found magnetic structures very similar to those produced by the linear modes with  $\alpha = 1$  (Chen et al., 1997; Doss et al., 2015; Li & Ma, 2010; Ofman et al.,

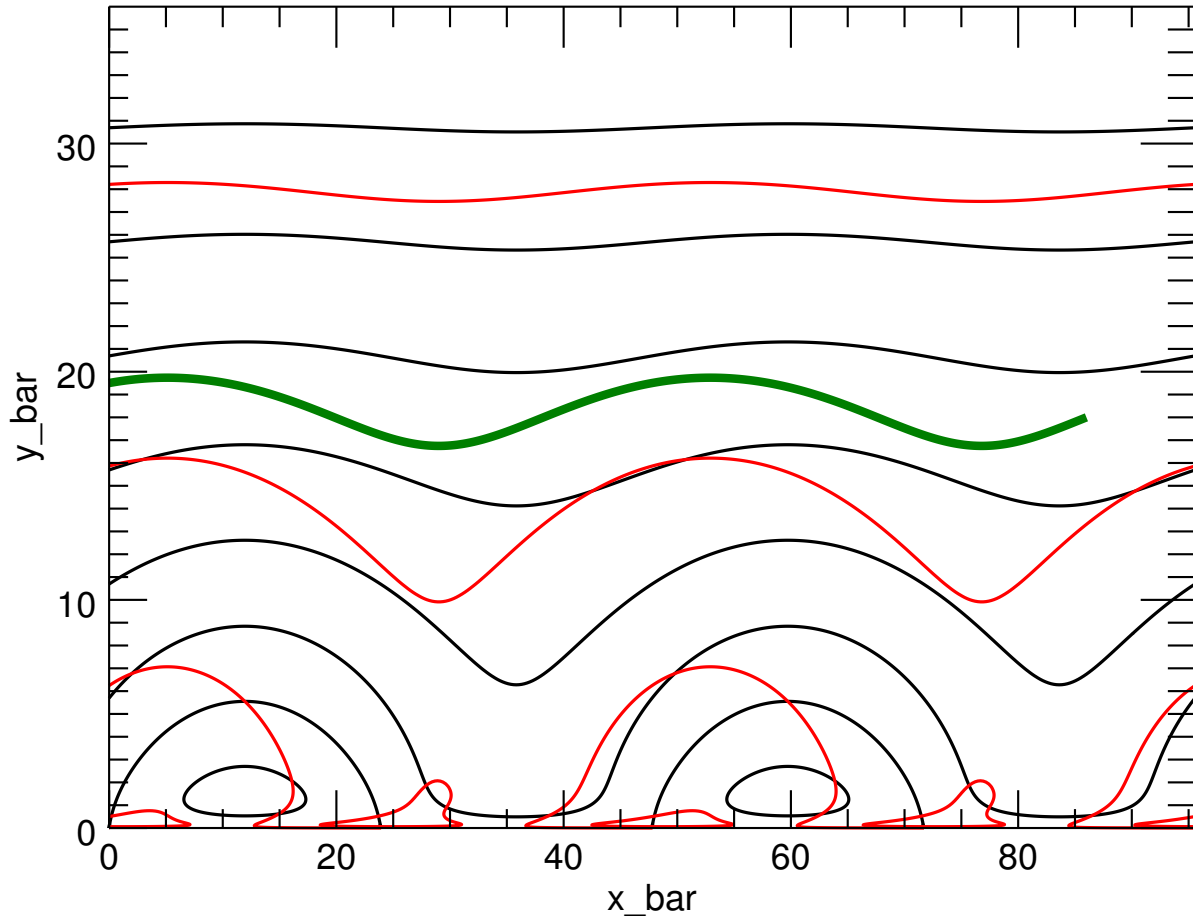


Figure 2.6: Contours of TM/KH eigenfunctions for  $S = 10^4$ ,  $\bar{k} = .1315$ , and  $V' = .037$  with  $\alpha = 1$ . The thick green line shows the trajectory of a particle that started at  $[\bar{x}, \bar{y}] = [86, 18]$ .

1993; Zhang et al., 2011). However, these treatments find a velocity field very different from the linear eigenmode. In particular, the velocity must align with the magnetic field outside the diffusion region which is not the case with the unsaturated linear eigenmode, as seen in Fig. 2.6. Non-linear studies of island saturation in the presence of external shear have shown the saturated stream-function assumes, instead, a form  $\Phi(x, y) \simeq (V_0/B_0)A(x, y)$ . In this case the flow follows magnetic field lines exactly and matches the external shear flow asymptotically. Such a structure is clear in the non-linear simulation of Ofman et al. (1993). Using this instead of the linear eigenmode results in the stream lines (red) shown in Figure 2.7. A particular fluid element is traced in green, as it was in Figure 2.6. While the inter-relations of the magnetic field and stream functions differ significantly between these two constructions, it is noteworthy how similar the green flow lines appear. In both cases the flow is made to oscillate by the magnetic field distortions produced by the islands

### Transformation to Observed Quantities

The analysis of the previous section was performed in a reference frame moving so as to make the velocity shear symmetric, thereby endowing the TM with zero phase velocity. In our proposed model one side of the CS is stationary, while the other is moving horizontally at some speed  $v_0$  (see Fig. 2.1 and 2.5). This means the analysis references frame is translating at  $V = v_0/2 = 18.5 \text{ km s}^{-1}$  to produce the phase velocity observed in the flare ribbon. Solutions for an asymmetric shear flow are found through a Galilean transform of the horizontal dimension,

$$\bar{X} = \bar{x} - \bar{V} \bar{t} . \quad (2.28)$$

Note again that  $\bar{V}$  is not the observed speed, but the speed of propagation along the solar surface. The transform is such that flow below the current sheet is  $2\bar{V} = .074$  and zero above just as in Figure 2.1. In this reference frame an observer would see the train of islands propagating in the direction of the non-zero shear flow, positive  $\bar{X}$ , with a velocity equal to

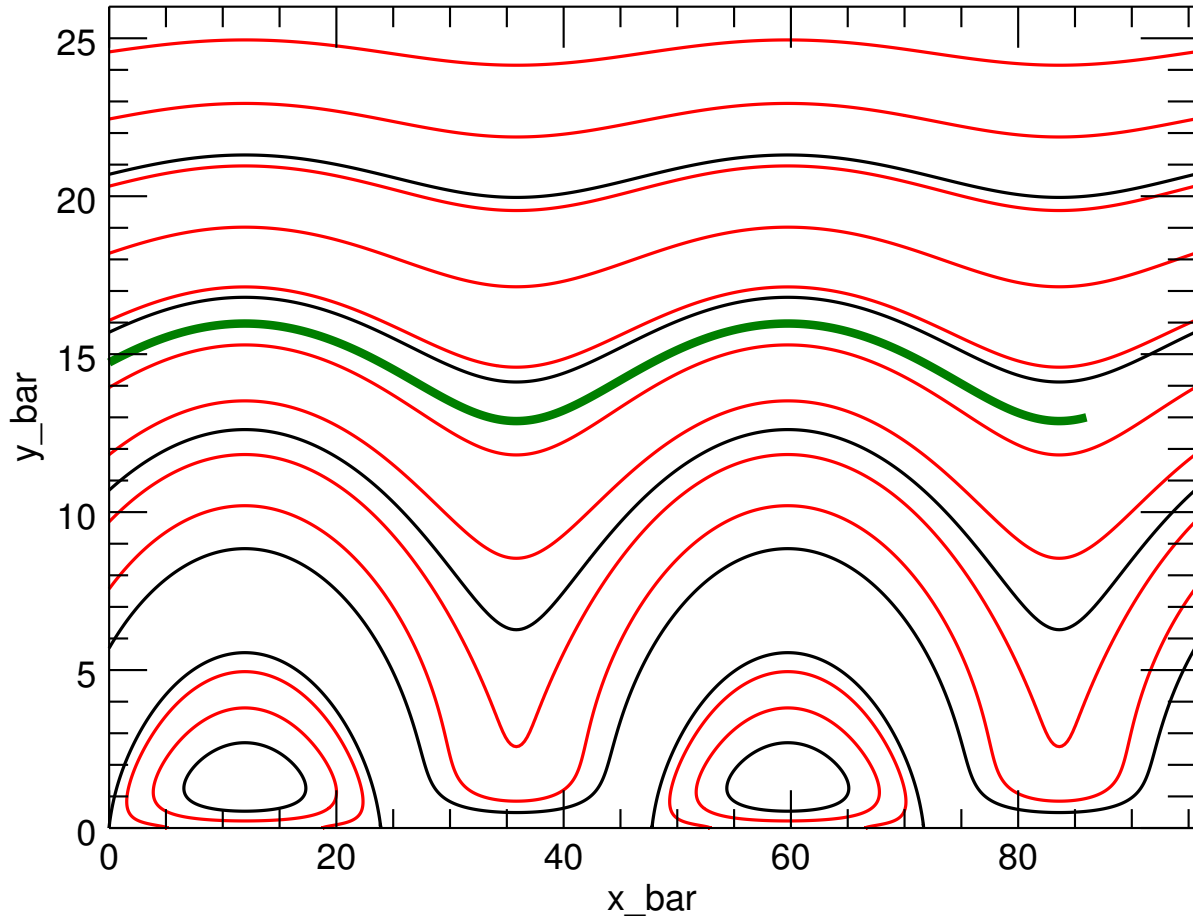


Figure 2.7: Contoured eigenfunctions of an approximated saturated state. Here the instability growth has stopped and the reconnection inflow/outflow has gone to zero. The green contour shows the trajectory of a fluid element beginning at  $[\bar{x}, \bar{y}] = [86, 13]$

$\bar{V}$ . A fluid element following the green trajectories in either Figures 2.6 or 2.7, loses most of its net velocity along the current sheet. Instead it undergoes elliptical motion, Figures 2.8a and Figures 2.8c respectively, as the the islands move past.

To construct the flows in Figure 2.8 we move from our non-dimensional model to physical units and observed quantities in the *Plane-Of-Sky* (POS) frame. Model quantities are foreshortened through the following transformations to observed quantities (denoted by primes):

$$y' = \bar{y} \cos(\theta_y) , \quad (2.29)$$

$$X' = \bar{X} \cos(\theta_x) , \quad (2.30)$$

where viewing angles are

$$\theta_x = \sin^{-1}(x_{\text{POS}}/R_\odot) = 33^\circ , \quad \theta_y = \sin^{-1}(y_{\text{POS}}/R_\odot) = -11^\circ , \quad (2.31)$$

for our region located at  $x_{\text{POS}} = 553''$ ,  $y_{\text{POS}} = -188''$ , when the apparent semi-diameter is  $R_\odot = 956''$ .

Spatial dimensions are scaled to arcseconds through current sheet thickness  $a$ . For each run of the model we specify  $\bar{k}$ , which with a fixed  $\lambda$  also specifies the current sheet thickness,  $a$ . This is done in the following way:

$$\bar{k} = ka = \frac{2\pi a}{\lambda} , \quad \lambda = \frac{\lambda'}{\cos(\theta_x)} , \text{ and } \lambda' = 2.3'' . \quad (2.32)$$

In this tilted frame a portion of the motion in both the  $X$  and  $y$  dimension are along the IRIS line of sight.

$$V_{\text{LOS}} = \sin(\theta_x) \frac{d\bar{X}}{dt} + \sin(\theta_y) \frac{d\bar{y}}{dt} . \quad (2.33)$$

This velocity is scaled to physical units through  $v_a = 500 \text{ km s}^{-1}$ . These transformations and scalings allow for a direct comparison between Figure 2.2 and 2.8.

Figures 2.8b and 2.8d show our model's reproduction of Figure 2.2 using the parameters above. These use the fluid trajectories from Figure 2.6 or 2.7 respectively, and obtain very similar results for reasons already mentioned. For both constructions we find that we can produce similar results using a wide range of other parameters.

It is worth noting that in Figures 2.8b and 2.8d, as well as in the observations of Figure 2.2, line-of-sight velocities oscillate from roughly  $-15 \text{ km s}^{-1}$  to  $+25 \text{ km s}^{-1}$ . The DC offsets in the model versions come from the fact that oscillations are not perfectly elliptical as is seen in Figures 2.8a and 2.8c. The observational data is probably consistent with this behavior within the measurement uncertainties. It is also worth noting that the Doppler velocity is not perfectly  $180^\circ$  out of phase with relative  $y$  position. This is due to the fact that motion in the  $\bar{y}$  direction has a component of velocity along the LOS in the tilted reference frame of the observation. The measured amplitude of the oscillation along the slit is harder to reproduce. This we can attribute to the fact that our linear model is incapable of generating islands that are truly saturated in height.

The measured amplitude of the sawtooth pattern is roughly 1 arcsecond which is larger than  $\lambda/2$ . Therefore, our linear model would never be able to exactly match observation. Regardless, we are able to report that our simple model gets us within a factor of 5 from true measured values.

The amplitude of both position and velocity depend on how far the fluid element is from the sheet, which is the starting value of  $\bar{y}$ . Elliptic motion in the solar frame are produced from streamlines which are *open* in the analysis frame. Closed streamlines will produce motion moving with the analysis frame. Moving closer to the current sheet gives higher amplitudes in position and velocity but also deviates from the mostly elliptical trajectory. Regardless, the elliptical motion and resulting phase portrait of Figure 2.8 are achievable for

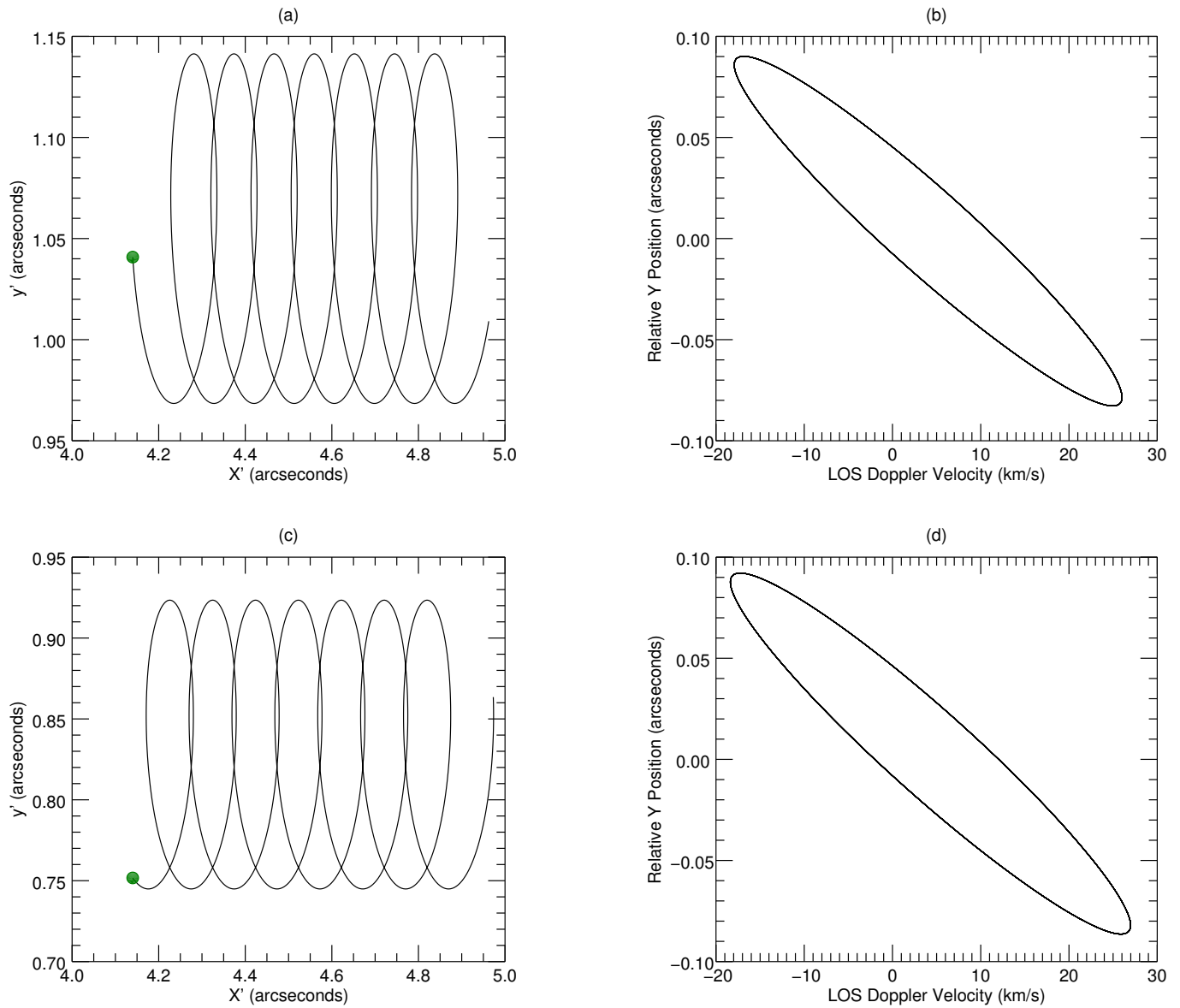


Figure 2.8: Panels a and b show the green trajectory from Figure 2.6 after undergoing the Galilean transform in Equation (2.28). Panels c and d show the same for the green trajectory in Figure 2.7. All displacements have been foreshortened to account for off disk observation and scaled to physical units. The green dot indicates the particles starting location.

a variety of initial conditions. Doppler velocities on order  $20 \text{ km s}^{-1}$  and elliptical trajectories with sufficient amplitude have been produced for  $S = 10^4$  to  $10^7$  and  $\bar{k} = .01$  to  $.5$ . The most limiting factor, and the reason we chose  $S = 10^4$  for producing Figures 2.6 – 2.8, was getting a growth rate high enough to satisfy Equation (2.26).

### Discussions and Conclusions

We have used a simple model of the tearing mode instability, defined in Section 2, to provide evidence that a tearing mode with asymmetric shear flow could produce the flare ribbon oscillations observed by Brannon et al. (2015). In our model asymmetric shear flow provides a net phase velocity to the instability, a key element of the findings. It also produces elliptical horizontal motions of fluid elements of the kind inferred by BLQ on the basis of the phase relationship between oscillations in velocity and position. We propose a scenario in which a secondary current sheet develops at the separatrix of the flaring field. A tearing mode in that secondary current sheet produces fluid motions similar to those observed. We rely on the measurement of both the sawtooth pattern wavelength,  $\lambda' = 2.3''$ , and phase velocity of  $15 \text{ km s}^{-1}$  as well as a typical flare timescale of  $100 \text{ s}$  to re-dimensionalize our model. Under these constraints we are able to reproduce the observed behavior of Figure 2.2 in Figure 2.8b and 2.8d to a satisfactory level of accuracy.

Our model is constrained by observations of the parameters  $\lambda$ ,  $\Delta y$ ,  $\Delta v_{\text{LOS}}$ , and a phase velocity of  $15 \text{ km s}^{-1}$  as well as achieving a minimum growth rate to satisfy Equation (2.26). These constraints limit our solution to a small area of parameter space. Assuming that  $\bar{k} = \bar{k}_{\max}$  the only free parameters are  $S$  and the distance  $y$  from the CS. We can reasonably fit the observations for  $S = 1 - 1.25 \times 10^4$ , or subsequently  $\bar{k} = 1.22 - .1315$ . This range of  $\bar{k}$ , along with a measured wavelength  $\lambda = 2.3''$ , yields a current sheet thickness  $a \simeq 39 - 42 \text{ km}$ . This is considerably smaller than current sheets reported through other observations. Savage et al. (2010) observe a long, thin, bright structure above an arcade with a thickness of

several times  $10^3$  km. Others have measured current sheet thicknesses of similar magnitude (Seaton et al., 2016). Models have shown that these large observed thicknesses may be the result of a layer of hot dense plasma surrounding the current sheet rather than the current sheet itself (Reeves et al., 2010; Seaton & Forbes, 2009; Yokoyama & Shibata, 1998). This leads us to believe that a current sheet on order 10 km is a realistic estimate for the April 18 flare.

Resistivity sets a lower limit on the CS thickness given by the steady Sweet-Parker model:  $a = LS^{-1/2}$ , where  $L$  is the length of the CS. The entire flare ribbon, in this case, has a length  $L \sim 50$  Mm. Classical Spitzer resistivity, yields  $S \sim 10^{12}$  from which we would predict a lower limit of  $a = 50$  m. It is possible that the resistivity in the vicinity of the CS is enhanced, perhaps by turbulence or instability (Strauss, 1986) to a level where  $S \sim 10^6$  for which a Sweet-Parker CS would have the thickness we infer. It is also possible that the sheet has not fully collapsed, and its thickness is instead set by the dynamics of its formation. It is not, after all, the flare CS, and is only formed as a secondary consequence of the flare.

The geometrical scenario proposed in Figure 2.5, necessary for this observation, does not follow from the standard CSHKP model, and is not inevitable in a two-ribbon flare. The lack of sawtooth reports from the many other flare ribbon observations made by IRIS suggests that sheared, tearing-unstable secondary current sheets, are not a common to all flares. It would seem they have occurred at least twice – in the flares of 2014-04-18 and again on 2014-09-10. A survey of several other, seemingly suitable IRIS ribbon observations has shown that sawteeth are indeed uncommon, but other candidates seem to have occurred (Roegge & Brannon, 2017). Shear flows responsible for deflecting the overlying magnetic field must be fast enough and sustained long enough for a secondary current sheet to develop and become unstable. Furthermore, if the wavenumber or the amplitude were smaller than that of April 18, the pattern may be too small to resolve with IRIS. Indeed, the pattern pattern observed in that flare is marginally detectable in coincident AIA images (BLQ).

The proposed shear flow, embedding the CS, is essential for explaining the observed phase velocity of the sawtooth. It is plausible that the eruption, initially traveling at many hundreds of km/s, left a slower, but persistent, flow in its wake. We have not, however, seen any clear evidence for this proposed flow, aside from the propagation of the sawtooth itself, in any of the data we examined. It is possible that the shear flow and the tearing mode occur higher up the CS, away from the chromospheric ribbon. The line-tying effect of the lower boundary could suppress the flow, while still permitting the form of the instability to be imprinted on the chromosphere. A more complicated three-dimensional geometry of this kind would need to be explored in a model more sophisticated than our two-dimensional version of the standard TM model. Our model scenario calls for the horizontal shear flow just discussed, as well as a current sheet flowing vertically along the separatrix – this is the secondary current sheet. Such a secondary current sheet was reported by (Janvier et al., 2014) in vector magnetograms data from a much larger flare. In spite of the favorable orientation of that flare, measurement of this weak secondary current sheet proved extremely difficult. It is nevertheless possible that a similar careful analysis of SDO/HMI data could reveal the presence of the secondary current sheet in the 18 April, 2014 flare.

We have used a simple two-dimensional, analytic model of a tearing mode in order to demonstrate, as simply as possible, the viability of our explanation of the observation. An analytic model allows us to explore parameter space and to easily re-scale the results for comparison to observations. The simplified analytic model is, however, subject to limitations. We are unable to self-consistently describe non-linear phases including saturation. Instead we constructed velocities fields intended to represent two extreme limits. Figure 2.6 shows an unsaturated state produced from the velocity field of the growing linear eigenmode. Figure 2.7 approximates the fully saturated state, where flow must follow the magnetic field. Remarkably, both these approximate, limiting cases yield observational signatures, compared side by side in Figure 2.8, which are virtually indistinguishable from one another.

This is no coincidence. The basic feature revealed by the observation is flow near the current sheet being modulated by a moving chain of magnetic islands. This produces elliptical motion of the kind reported by BLQ, and our model implements the explanation original given in that work. A self-consistent non-linear model is beyond the scope of our exploratory study, but we believe it would produce velocity structures falling between the two extreme approximations we do consider. Observations synthesized from it would therefore probably resemble the indistinguishable versions produced by the extreme cases. It would therefore match the observations for the same reasons they do.

If our hypothesis stands up under further scrutiny, the April 18 observation provides novel evidence for a TM in the solar corona. Plasmoid observation, and the presence of a TM instability, provide insight into the onset of fast magnetic reconnection. It is also noteworthy that while the TM occurs during a flare, it does not occur in the flare's primary current sheet. The sawtooth would thus seem to be a secondary effect offering only limited insight into the flare itself.

#### Acknowledgements

The authors would like to thank Dr. Sean Brannon for his work with this observation. This work has been supported by NASA grants NNX14AD43G and NNX16AH04G as well as contract 8100002702 from Lockheed Martin to Montana State University. IRIS is a NASA small explorer mission developed and operated by LMSAL with mission operations executed at NASA Ames Research center and major contributions to downlink communications funded by ESA and the Norwegian Space Centre.

## DETERMINING THE SPECTRAL CONTENT OF MOSES IMAGES

Contribution of Authors and Co-Authors

Manuscript in Chapter 3

Author: Jacob D. Parker, Montana State University

Contributions: Built forward model, performed significance testing and final fitting, and prepared the manuscript

Author: Charles Kankelborg, Montana State University

Contributions: Helped to conceive the study and guided the analysis, also provided feedback on the manuscript

Manuscript Information

Jacob Parker and Charles Kankelborg

Astrophysical Journal

Status of Manuscript:

- Prepared for submission to a peer-reviewed journal  
 Officially submitted to a peer-reviewed journal  
 Accepted by a peer-reviewed journal  
 Published in a peer-reviewed journal

Abstract

The Multi-Order Solar Extreme Ultraviolet Spectrograph (MOSES) sounding rocket was launched from White Sands Missile Range on February 8th, 2006 to capture images of the sun in the He II 303.8 Å emission line. MOSES is a slitless spectrograph that forms images in multiple spectral orders simultaneously using a concave diffraction grating in an effort to measure line profiles over a wide field of view from a single exposure. Early work on MOSES data showed evidence of solar features composed of neither He II 303.8 Å or the nearby Si XI 303.3 Å spectral lines. We have built a forward model that uses co-temporal EIT images and the Chianti atomic database to fit synthetic images with known spectra to the MOSES data in order to quantify this additional spectral content. Our fit reveals a host of dim lines that alone are insignificant but combined contribute a comparable intensity to MOSES images as Si XI 303.3 Å. In total, lines other than He II 303.8 Å and Si XI 303.3 Å contribute approximately 10 percent of the total intensity in the MOSES zero order image. This additional content, if not properly accounted for, could significantly impact the analysis of MOSES and similar slitless spectrograph data, especially those using a zero order (undispersed) image. More broadly, this serves as a reminder that multilayer EUV imagers are sensitive to a host of weak contaminant lines.

Introduction

An essential tool used to study remote solar phenomena is the spectrograph. By more closely examining the wavelength of light emitted from the sun we gain access to a wealth of information (temperature, density, velocity, etc.) needed to more completely describe the solar plasma and properly inform our models. Slit spectrographs take a very narrow strip of the sun and disperse the light emitted using a diffraction grating, providing high spectral resolution over a very small spatial field of view. Spectrally resolved images are then built by

rastering the slit over a region of interest, requiring a full exposure at every position, which can take on the order of hours to cover a large portion of the solar disk.

An alternative approach is to remove the slit, a *slitless* spectrograph. Slitless spectrographs disperse an image over a larger field of view. The data from these instruments, sometimes called overlapograms, have spatial and spectral information overlapped in the dispersive direction. Slitless spectrographs often image in multiple spectral orders, each with a different blend of spatial and spectral information, that can be combined and “inverted” to form a spectrally resolved image of the sun at every exposure. By doing so these instruments trade spatial and spectral resolution for much higher cadence.

Slitless spectrographs have been used infrequently for decades to image the sun and have recently regained popularity. Only two satellite missions have routinely captured solar slitless spectrograph data: The S082A instrument on *Skylab* (Tousey et al., 1973) and the Res-K instrument of the Russian KRONOS-I mission (Zhitnik et al., 1998). These two instruments have informed the recent development and proposal of another full disk slitless spectrograph, the COronal Spectroscopic Imager in the EUV (COSIE: Golub et al., 2020; Winebarger et al., 2019). The currently operating Extreme-ultraviolet Imaging Spectrograph (EIS: Culhane et al., 2007)) on the *Hinode* mission (Kosugi et al., 2007) includes 40'' and 266'' slots that can produce overlapogram that has been used in a limited number of quantitative studies (Harra et al., 2020, 2017). In addition to these satellite missions several sounding rocket based slitless spectrographs have recently imaged the sun including The Multi-Order Solar Extreme ultraviolet Spectrograph (MOSES: Fox, 2011), the Extreme ultraviolet Snapshot Imaging Spectrograph (ESIS: Parker et al., 2021; Smart et al., 2021), and the recently launched Marshall Grating Incident X-ray Spectrometer (MaGIXS: Athiray et al., 2019) that was flown with a 12' × 33' slot.

MOSES was launched for the first time from White Sands Missile Range on February 8th, 2006. The primary science goal of MOSES was to measure line profiles in He II 303.8 Å

over a wide field of view ( $\approx 20' \times 10'$ ) at every exposure. By imaging in multiple orders simultaneously,  $m = -1, 0$ , and  $1$ , MOSES captures three different projections through a spatial-spectral cube,  $I(x, y, \lambda)$ , that can be combined and inverted to return a line profile at every pixel over its large field of view, at every exposure. Various inversion methods have been used to return line profiles thus far, mostly for small explosive events in He II 303.8 Å (Courrier & Kankelborg, 2018; Fox, 2011; Fox et al., 2010; Rust & Kankelborg, 2019).

Early work with MOSES images revealed faint solar features when subtracting different spectral orders, as well as in the residuals while inverting, that could not be attributed to He II 303.8 Å. These features could not be attributed to the most obvious sources of spectral contamination, including the nearby Si XI 303.3 Å, or two bright Iron lines, Fe XV 284 Å and Fe XVI 335 Å. The periodic multilayer coatings used on the MOSES primary and secondary optics were designed to allow for optimal throughput at 304 Å but to suppress the close Iron lines, Fe XV 284 Å and Fe XVI 335 Å, as much as possible (Owens et al., 2005) making them an unlikely source of contamination. Moreover, if much of the contamination were attributable to one of these strong lines, then the contaminant features should appear twice in the difference images: once at the correct location on the Sun, and then in inverted intensity at a predictable offset; yet such a pattern was not observed (Fox, 2011). Si XI 303.3 Å, which is too close in wavelength to be removed by the MOSES multilayer coating was always expected to be a contamination source in the data. With a spectral dispersion of  $\approx 29$  mÅ per pixel ( $\approx 30$  km s $^{-1}$  per pixel), features in Si XI 303.3 Å are dispersed roughly 15.7 pixels from He II 303.8 Å and therefore are easily distinguishable features in He II 303.8 Å. Therefore these unexpected solar features must be from emission at dimmer and less obvious wavelengths in the MOSES passband. In this paper we identify and quantify the sources of spectral contamination in the MOSES images. We also comment on the MOSES design decisions that led to this confusion, and how similar instruments can be adapted to better control spectral contamination.

In Section 3 we present a time averaged set of images from the 2006 MOSES flight, as well as 4 co-temporal and co-aligned images from SOHO EIT. We also discuss the unexpected solar features of unknown spectral content found in the MOSES data. Section 3 describes our methods for identifying and quantifying sources of spectral contamination. This includes using the cross-correlation of MOSES difference images as an indication of significant spectral contamination (Section 3 and 3) and how we combine data from EIT with synthetic spectra from the Chianti database (Del Zanna & Young, 2020; Dere et al., 1997) to generate synthetic MOSES images that can be fit to MOSES images (Section 3). Section 3 shows our best fit to the MOSES data, the resulting spectral content of the time averaged MOSES images. We discuss our results and their implications for future missions of this kind in Section 3.

### Data

#### MOSES

The MOSES sounding rocket launched from White Sands Missile Range on February 8th, 2006 at 18:44 UT. It recorded 27 exposures between 18:44:17 and 18:49:13 UT above  $\sim$  160 km in altitude, an altitude which roughly corresponds to 50% atmospheric transmission for 304 Å radiation. Exposure times ranged from .25 - 24 seconds with a roughly 6 second readout time in between. An exposure consists of three images, one for each of the three spectral orders  $m = -1, 0$ , and 1. For the rest of the paper we will refer to the  $m$ th order MOSES image as,  $I_m$ . All data was dark subtracted and co-aligned to exposure number 13 prior to our study (Fox et al., 2010).

To increase signal to noise, we form a single time averaged image in each spectral order. The wide range of exposure times obtained during the flight guarantees that well exposed, unsaturated intensities are available at every spatial location. Saturated pixels are replaced with IEEE NaN (Not a Number) and treated as missing data. Since MOSES observes through a time-varying column of atmosphere throughout its flight, we use the median of

each image as a proxy for exposure time, rather than the amount of time the shutter is open. At each spatial pixel, in each spectral order, the average intensity is the sum over time of unsaturated intensities divided by the sum of their proxy exposure times. This procedure also renormalizes the three MOSES spectral orders to the same sensitivity. The top row of Figure 3.1 shows the time averaged versions of  $I_1$  and  $I_0$ .

Identifying solar features in the MOSES data that originate at wavelengths different from He II 303.8 Å is simple. Subtracting  $I_0$  (that contains no spectral dispersion) from either outboard order ( $I_{+1}$  or  $I_{-1}$ ) eliminates 303.8 Å features. What remains are bipolar features of various spatial scales along the dispersion direction, which is horizontal. A feature in the principle spectral line, He II 303.8 Å, with a nonzero line-of-sight (LOS) velocity is translated along image rows. MOSES has a spectral dispersion of  $\approx 30 \text{ km s}^{-1}$  per pixel, leading to a less than ten pixel shift for even the fastest LOS velocities in He II. This results in a bipolar feature with an obvious positive and negative counterpart that are immediately next to one another. Events like these have been studied in detail by several authors (Courrier & Kankelborg, 2018; Fox, 2011; Rust & Kankelborg, 2019).

Features from other emission lines in the MOSES passband have shifts larger than 10 pixels and cannot be mistaken as Doppler shifted features in He II 303.8 Å. A feature in Si XI 303.3 Å, the next closest line, would be shifted by 15.7 pixels. Si XI features can be seen just above the solar limb, where He II has little to no contribution. The best example of this is region 3 boxed in red in Figure 3.1. Box 1 of Figure 3.1c has a large, coherent, negative feature dubbed the “wishbone”. The wishbone is very solar in appearance and has no obvious positive counterpart. Close inspection reveals a white smear to its left that is likely a shifted wishbone in the plus order. Unfortunately the positive portion of the wishbone is too blurry to quantify its shift by inspection. A previous study of these features by Rust (2017) used a wavelet transform to isolate large scale features prior to taking the difference. That procedure allowed Rust (2017) to roughly identify a contribution from Mg VIII 315 Å to regions 1 and

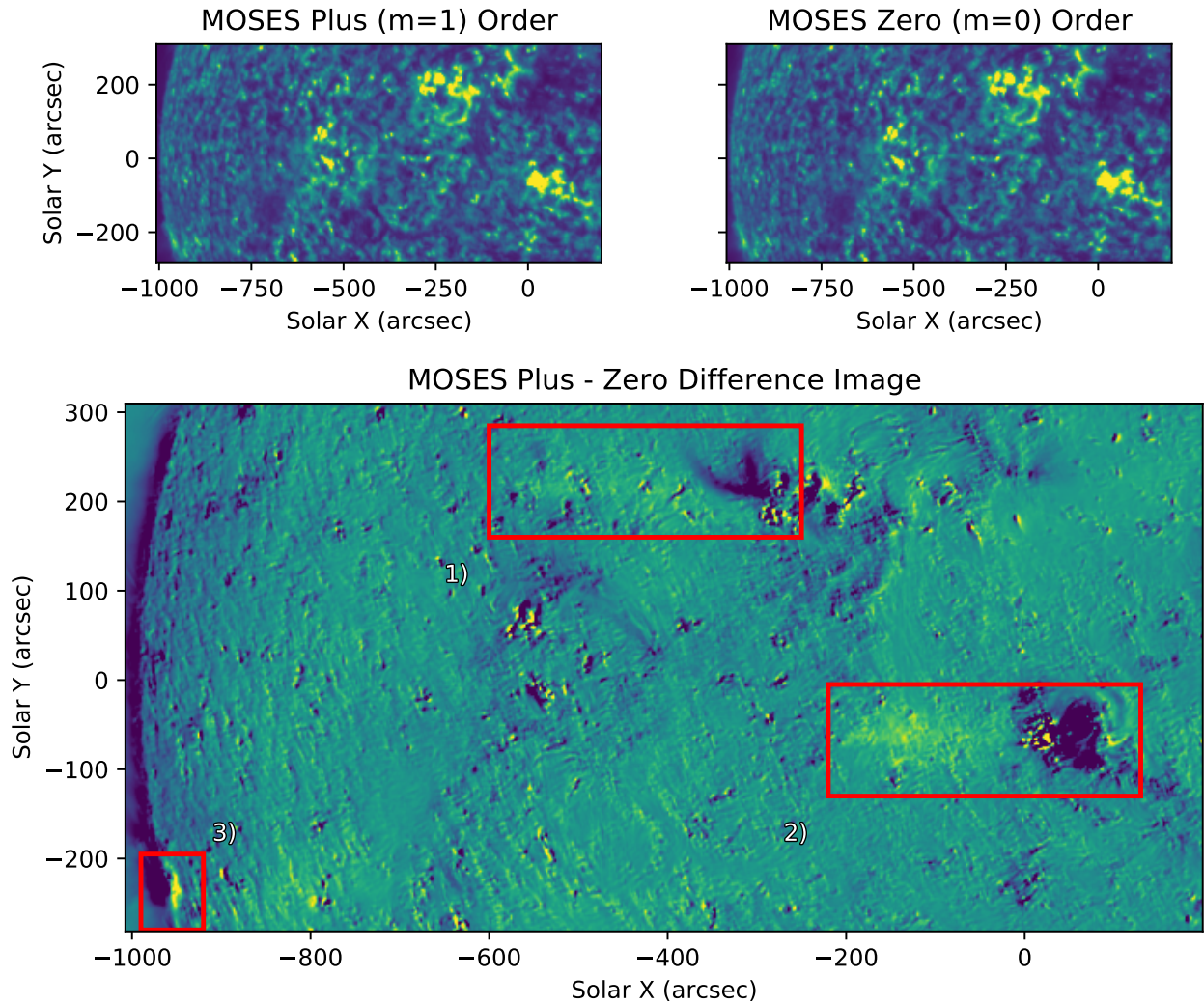


Figure 3.1: Time averaged images for the  $m = 0$  and  $1$  spectral orders (top row), followed by their difference,  $m = 1$  minus  $m = 0$ . Regions one through three, boxed in red, show regions of high spectral contamination. Dark features from the  $m = 0$  order are adjacent to white smears with pixel shifts too large to be Doppler shifts.

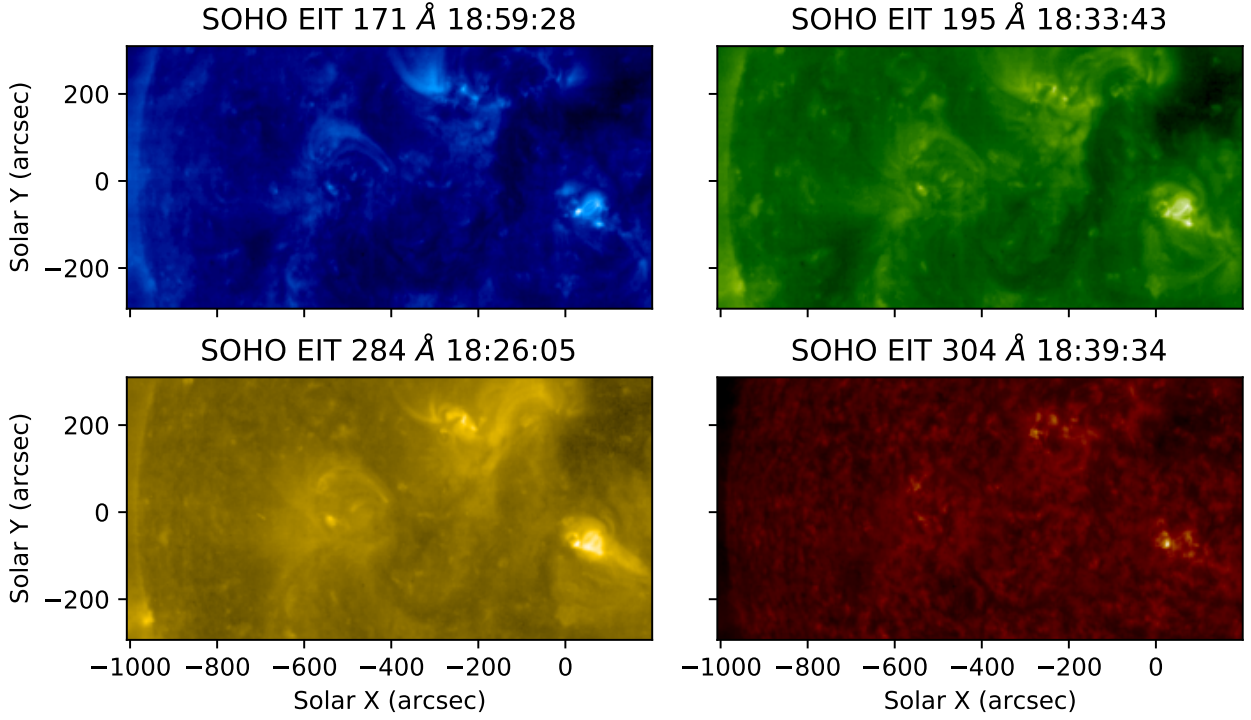


Figure 3.2: SOHO EIT Images taken closest the MOSES Launch on February 8th, 2006. Each image was rotated to 2006-02-08 18:47 UT to match the middle MOSES exposure time. After rotation, the EIT 304 channel was linearly co-aligned to the MOSES zero order, and then the same transformation was applied to every other channel. Each image has been fourth root scaled.

2. Rust (2017) also identified a faint copy of the limb,  $\approx 200''$  to the right of region 3 that was attributed to Si IX/ Fe VI 296.1 Å. Although the probable sources of contamination were identified, their contributions to the total image intensity were not quantified.

### EIT

The Extreme ultraviolet Imaging Telescope (EIT: Delaboudinière et al., 1995) on board the Solar and Heliospheric Observatory (SOHO) captured 4 full disk EUV images, one in each of the 171 Å, 195 Å, 284 Å, and 304 Å channels (Figure 3.2) within  $\approx 20$  minutes of the 2008 MOSES flight. Prior to use, each image was first despiked using `iris_prep_despike.pro` with default settings and made level 1 with `eit_prep.pro`. They were then rotated to 2006-

02-08 18:47 UT, the timestamp of image 13 of the MOSES observing sequence (Fox, 2011), using `drot_map.pro`. EIT and MOSES were co-aligned by applying the affine coordinate transform to EIT 304 Å that maximized the zero-lag cross-correlation between it and the time averaged  $m = 0$  order image described in the proceeding subsection. The same transform was then applied to the other three EIT channels.

At first glance one can find several features in the MOSES difference image (Figure 3.1) that resemble features in the EIT 171, 195, and 284 images (Figure 3.2). The presence of these features in MOSES data indicates a contribution of coronal spectral lines to an otherwise transition region image. While similarities between MOSES difference images and EIT images indicate the contribution of hotter lines to MOSES He II data, they do not straightforwardly tell how much, and by which lines. In Section 3 we set out to quantify the intensity contributed by each source of spectral contamination in the MOSES image.

## Methods

### Difference Image Cross-Correlation

To help identify signatures of hot spectral lines, we cross-correlated the MOSES difference images along the dispersion direction, or image rows. Performing a cross-correlation on the difference images requires justification. An obvious first choice would have been to simply cross-correlate  $I_0$  with either outboard order. Unfortunately the correlation function is dominated by the autocorrelation of the He II signal as seen in Figure 3.3d and 3.3e. These example cross-correlations show two main peaks in correlation that are due to the auto-correlation of bright He II features, and not spectral contamination. This would also be the case when cross-correlating  $I_{+1}$  and  $I_{-1}$ . By taking the difference we remove stationary He II objects (Figure 3.4d and 3.4e) and, in turn, their autocorrelation from the cross-correlation function (Figure 3.4f), leaving only peaks in correlation from features not of He II 303.8 Å.

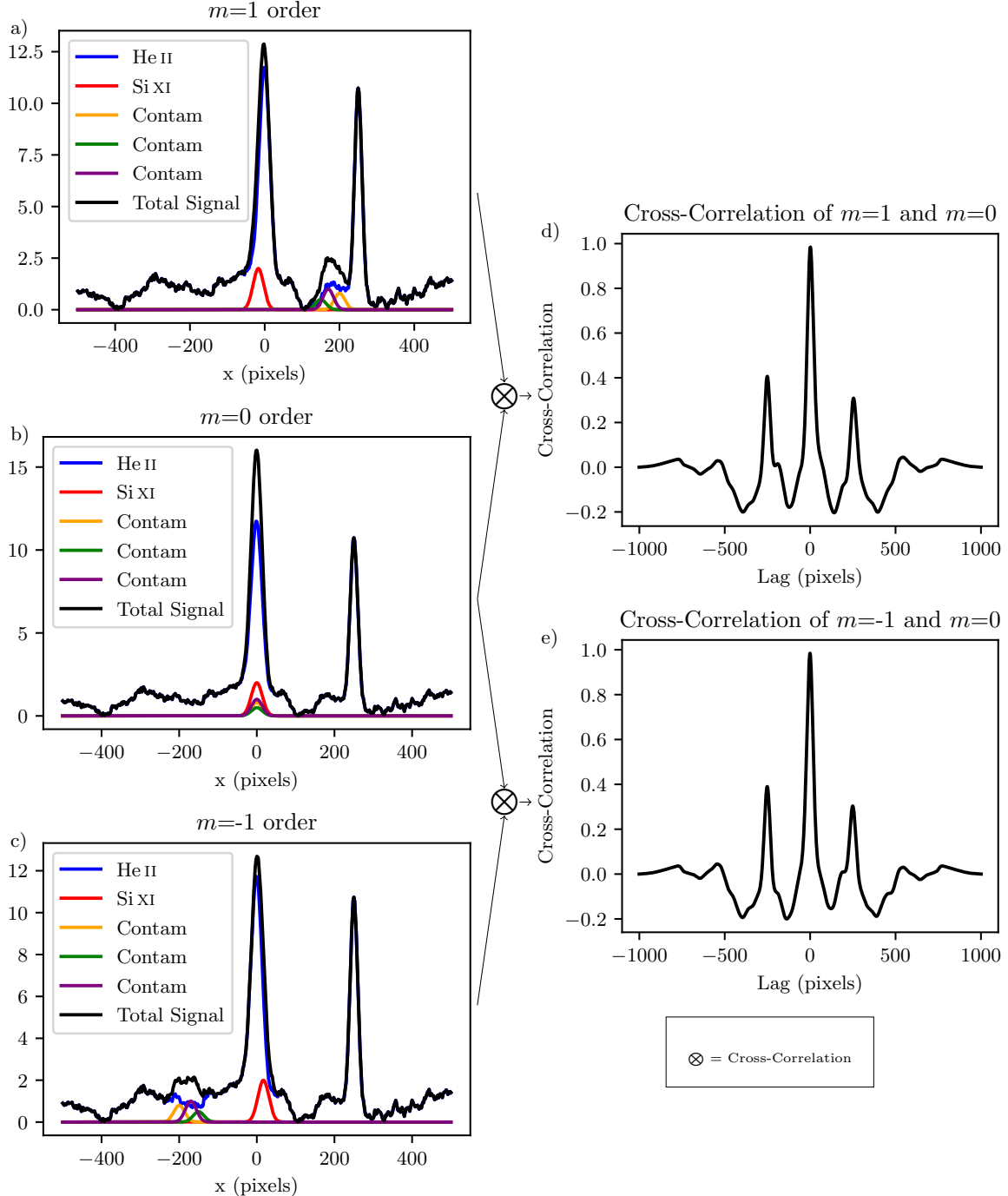


Figure 3.3: Example 1D MOSES row in the  $m = 1$  (a), 0 (b), and -1 (c) spectral orders followed by the cross correlation of  $m=1$  and 0 (d) and the cross-correlation of  $m = -1$  and 0 (e). The cross-correlation of any two MOSES orders is dominated by the autocorrelation of stationary He II features and background making them less useful in identifying spectral content. The strong peaks in correlation at  $\pm 250$  pixels are the result of the two bright He II features at 0 and 250 overlapping.

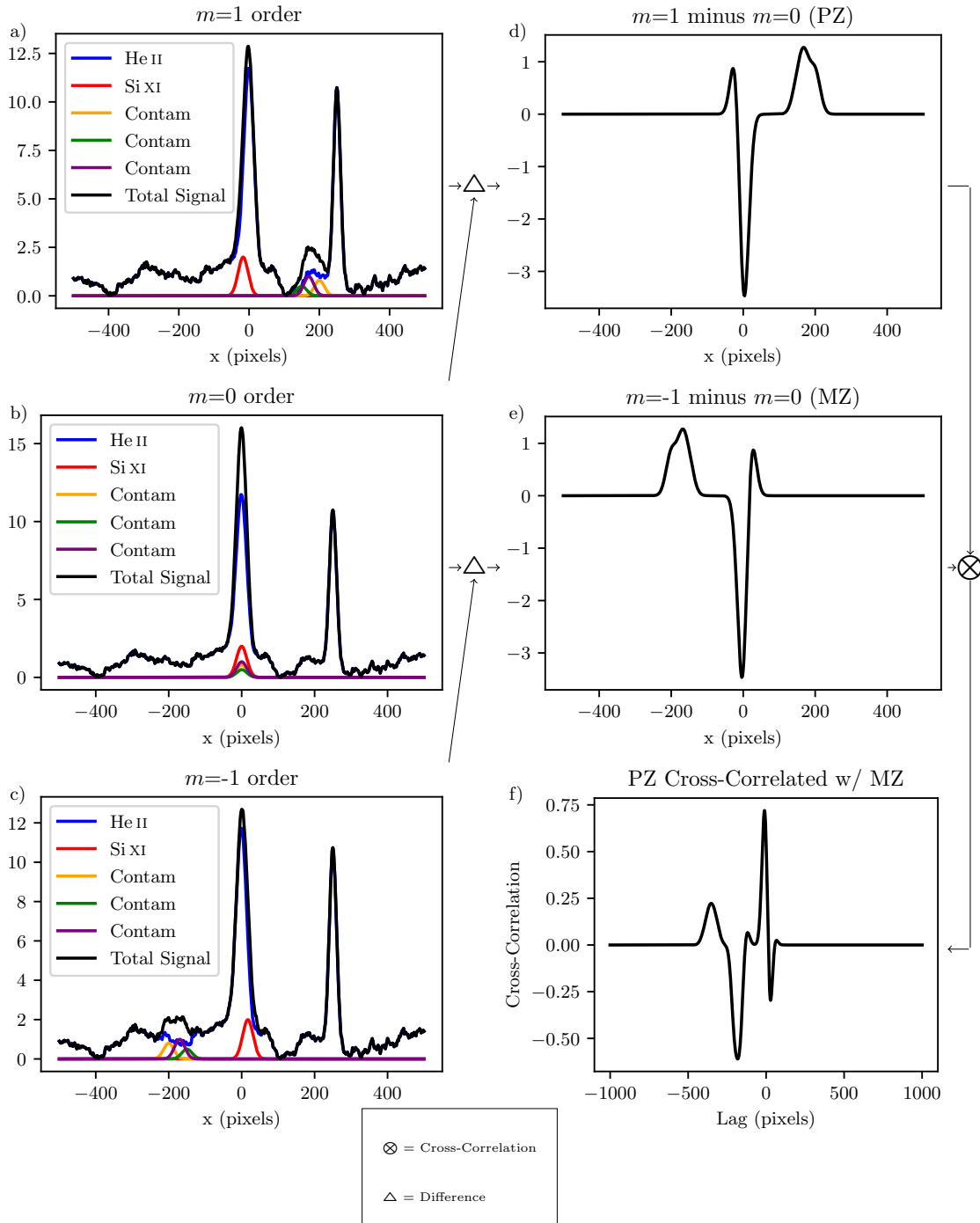


Figure 3.4: Example MOSES rows in  $m = 1$  (a), 0 (b), and  $-1$  (c) spectral orders. Two difference images,  $m = 1$  minus  $m = 0$  (d) and  $m = -1$  minus  $m = 0$  (e) are cross-correlated (e). Taking a difference removes stationary He II features so that peaks in cross-correlation are indicative of extra spectral content. Even in this simple example one cannot read off the spectral content of the MOSES images, demonstrating the need for a forward model.

The cross-correlation of two difference images along their rows is defined to be

$$(I_{+1} - I_0) \otimes (I_{-1} - I_0) = \mathcal{F}_x^{-1} \{ \mathcal{F}_x(I_{+1} - I_0) \mathcal{F}_x(I_{-1} - I_0)^* \}, \quad (3.1)$$

where  $\mathcal{F}_x$  is the Fast Fourier Transform (FFT) operator applied along image rows. Also, image rows were padded with zeros, prior to applying the FFT to minimize effects of wrap-around. Notice that edge effects are practically absent because of our choice to work with image differences. Consequently, windowing was not necessary. This yields a one dimensional cross-correlation function for each row of the MOSES difference images. Since we are concerned mostly with bulk spectral content we then take the mean of all 1024 cross-correlation functions, one for each row, to get our final correlation curve plotted in red in Figure 3.5.

The mean cross-correlation curve for the MOSES difference image has a few notable features. There are large peaks in correlation at approximately  $-1800$ ,  $-500$ ,  $250$ ,  $800$ , and  $1500$  pixel lags. The largest peak in correlation is centered about zero lag and is quite broad. While these features are identifiable, the curve is complicated enough that quantifying peaks in correlation visually is difficult and the significance of any given peak is questionable. We therefore move to test the null hypothesis that none of these features are due to spectral contamination but are instead the result of random fluctuations in the data. We explore this null hypothesis in the next section by cross-correlating random data generated to emulate the scales present realistic solar features, such as those found in the MOSES image rows.

### Significance Testing

The mean cross-correlation function of the two MOSES difference images, red in Figure 3.5, has several interesting peaks in correlation. As can be seen in Figure 3.4e, these peaks can be indicative of extra spectral content. Actual MOSES images contain information not represented in the Figure 3.4 cartoon. Each MOSES order has a slightly different point

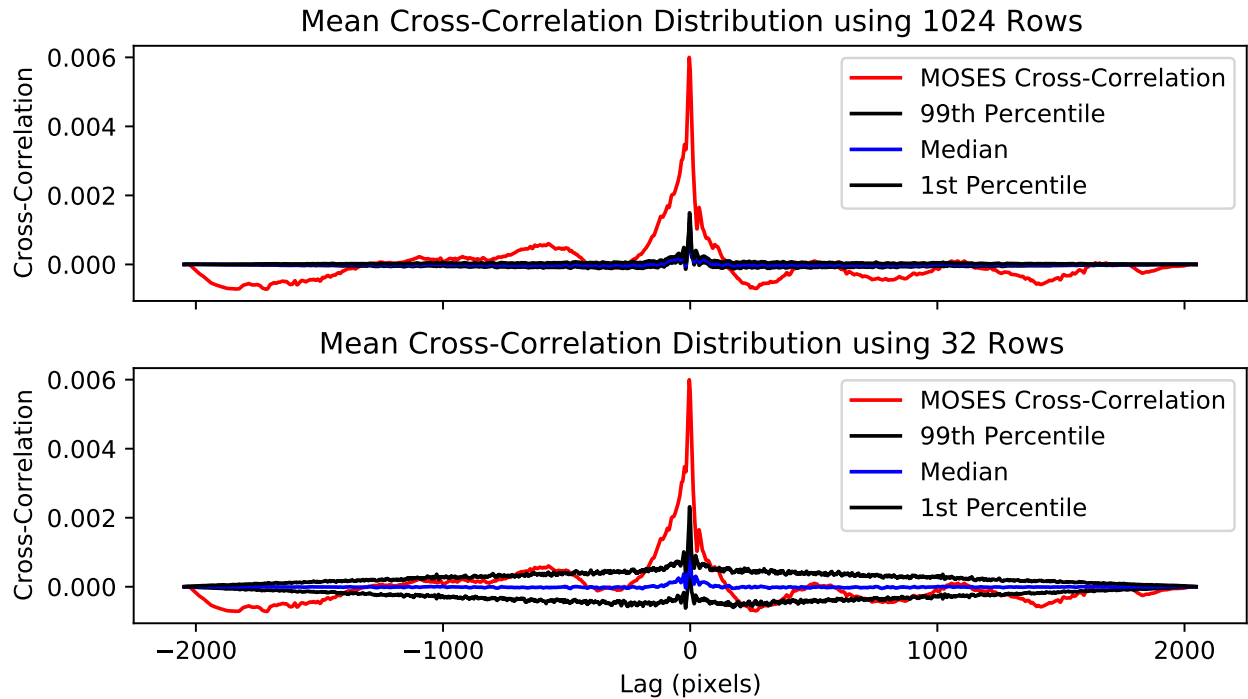


Figure 3.5: The mean cross-correlation function of MOSES difference image rows (red) is compared to a distribution of mean cross-correlations from a selection of randomly generated test row differences (Section 3). The top panel shows the distribution after taking the mean of 1024 (the number of MOSES rows) randomly chosen test row differences 10,000 times. The bottom panel challenges that all 1024 rows of MOSES are unique and shows the distribution for only 128 randomly chosen difference rows, also 10,000 times. In either case the mean cross-correlation values from the MOSES data exceed the 98 percent confidence interval and are therefore deemed significant and indicative of spectral content in the MOSES data.

spread function and the He II features are not all stationary. This leads to many extra small scale features in the difference images across the field of view. It is also unclear what magnitude of cross-correlation we should expect from extra spectral content. We therefore move to test the null hypothesis that the features in the MOSES difference image cross-correlation curve are the result of random correlations between each difference image and not indicative of extra spectral content.

To investigate the null hypothesis, we require test solar data that match the MOSES image rows in length and have similar power spectra and autocorrelation. MOSES images contain 2048 columns. These columns have the same spatial features as MOSES image rows and the same noise distribution, but with none of the repeating patterns that arise from contaminant spectral lines. Therefore, MOSES images columns fairly represent how the MOSES image rows would appear under the null hypothesis. Despite this the MOSES image columns are insufficient for significance testing in two ways. First, there is an insufficient sample size. With features in the MOSES images ranging from  $\approx 4\text{-}100$  pixels in size, we have at most 512 as few as 20 unique columns for significance testing. Second, MOSES columns are half as long as the rows, preventing us from measuring the significance of correlation past 1024 pixel lag. Therefore we require additional steps to generate a test data set for significance testing.

Using the MOSES image columns as our basis we generated  $N$  random arrays that are 2048 pixels long and resemble MOSES columns in structure. First each time averaged MOSES image,  $I_{mxy}$ , is windowed with a Hanning window,  $w_y$ , and Fourier transformed along the column dimension,  $y$ . The windowed Fourier transformed array is defined to be

$$\tilde{I}_{mxk_y} = \mathcal{F}_y [w_y I_{xy}] \quad . \quad (3.2)$$

The spatial dimensions  $x$  and  $y$  represent MOSES image with  $x = 0, 1, \dots, 2047$  and  $y =$

$0, 1, \dots, 1023$ .

From the set of all the Fourier transformed data columns, we will generate a test *row* for each order,  $I'_{mx}$ , by populating its Fourier transform,  $\tilde{I}'_{mk}$ . Each new array is formed by picking an element randomly from the distribution of Fourier transformed columns. Importantly, the same random choice is used to for each spectral order,  $m$ . The transformation outlined in Equation 3.2 gives a distribution of 511 spatial frequency bins and one DC bin that each have 1024 elements (one from each column) for each order. Once assembled, each array is further scrambled by giving each value of  $k$ , aside from the DC term, a random phase shift,  $e^{i\phi}$ , with  $\phi \in (0, 2\pi]$  drawn from a uniform distribution. The same random phase  $\phi$  is employed for the  $k^{\text{th}}$  Fourier component of each spectral order, producing three simulated rows that differ only according to the spectral order from which they were taken.

In order create an array that is 2048 elements long from one that is 1024 elements long we require twice as many values of  $k$  as  $k_y$ :

$$k_y = \begin{cases} 0, & k = 0, \\ \text{ceil}\left(\frac{k}{2}\right), & 0 < k < 1023, \\ 511, & k = 1023, \\ 512, & k = 1024, \end{cases} \quad (3.3)$$

where `ceil` rounds up to the nearest integer, and the  $k$ -indices are arranged as they traditionally are in the fast Fourier transform. Since our data is purely real we can fill in the remaining Fourier components, negative frequencies, with the complex conjugate of the corresponding positive frequency component. Finally, all synthetic rows of spectral order

$m$  are found through an inverse FFT,

$$I'_{mkn} = \mathcal{F}_x^{-1} \left[ \tilde{I}'_{mkn} \right]. \quad (3.4)$$

We examined randomly drawn 1024-pixel segments from the 2048-pixel synthetic MOSES test rows and compared their power spectra to those of the original columns. The 10th percentile, median, and 90th percentile power spectra of both sets match extremely well, giving us confidence that our wavenumber interpolation scheme was properly implemented and yielded plausible distributions of intensity in the test rows.

Now that we have created a set of 10,000 test rows for each order  $m$  we can cross-correlate the order-difference for each row, as we did for MOSES. This yields a set of 10,000 test difference row cross-correlation functions. Since we are interested in the average MOSES difference row cross-correlation we choose a number of test row cross-correlations and average them together before comparison. The blue and black curves in the top panel of Figure 3.5 shows the result of picking 1024 random test cross-correlations (the same number of rows as a MOSES image) and taking their average. We do this 10,000 times and form a distribution of mean cross-correlation values at each pixel lag. The 1<sup>st</sup> and 99<sup>th</sup> percentile of the distribution are plotted in black and the median in blue. From the top panel of Figure 3.5 it is clear that a mean cross-correlation much greater or less than zero is highly unlikely in our test rows with no spectral content. The exception to this is at zero lag when a positive peak in correlation well above zero is typical. Despite this exception the peak in mean cross-correlation from the MOSES data is much greater, and broader, than that of the test data. The comparison in the top panel of Figure 3.5 assumes that all 1024 difference rows from the MOSES data are unique. Since solar features in the MOSES images exceed a single pixel in size this is unlikely. The bottom panel of Figure 3.5 is made in the same way as the top panel but uses the mean of only 32 rows when forming the distribution. We believe 32 independent

rows represents a reasonable lower bound after examining the auto-correlation length of the MOSES rows and seeing a large fall off in autocorrelation ( $\approx 75\%$  on average) by 32 pixel lag. Even when we assume that MOSES has only 32 unique rows we can see the same five large peaks in the MOSES mean cross-correlation (identified in Section 3) fall outside the 98 percent two-sided confidence interval.

From this study we find that the shape and magnitude of the largest peaks in the mean cross-correlation of the MOSES difference images are significant and indicative of spectral content. We therefore wish to quantify that spectral content.

### Forward Model

In this section we use a forward model of the MOSES instrument to form synthetic images with a known spectral content and fit them to the MOSES data in order to identify and quantify the sources of spectral contamination. In particular, we wish to reproduce the broad undulations that are present in the MOSES cross-correlations in Figure 3.5, which were shown in the previous section to be statistically significant. In order to interpret how these peaks in correlation relate to spectral content of the MOSES images we developed a forward model that produces synthetic MOSES difference images with known spectral content using the 4 co-temporal EIT images and Chianti. These synthetic images can be cross-correlated in the same way and compared to the mean MOSES cross-correlation function. Synthetic MOSES images for each order  $m$ ,  $I'_{mxy}$ , were created using the following procedure:

1. Form a DEM map,  $\xi_{xyT}$ , a DEM at every spatial pixel, from 4 co-temporal and co-aligned EIT images.
2. Normalize  $\xi_{xyT}$  to have unit emission measure averaged over the MOSES field of view at every temperature.
3. Calculate the contribution function,  $G_{\lambda T}$ , over the range  $\log T = 4\text{-}6.5\text{ K}$  for each

spectral line between 280 Å and 340 Å using a unit emission measure.

4. Form a synthetic line image at each temperature for every spectral line.

$$I'_{xy\lambda T} = \xi_{xyT} G_{\lambda T} \quad (3.5)$$

5. Shift  $I'_{xy\lambda T}$  along image rows according to the MOSES spectral dispersion  $\delta$ . Sum the dispersed map multiplied by the MOSES optical throughput,  $\alpha_{m\lambda}$ , along the wavelength axis.

$$I'_{mxyT} = \sum_{\lambda} I'_{(x-m\frac{\lambda-303.78}{\delta})y\lambda T} \alpha_{m\lambda}. \quad (3.6)$$

6. Multiply by desired spatially averaged DEM and integrate in temperature to form a synthetic MOSES image in each order.

$$I'_{mxy} = \sum_T I'_{mxyT} \text{DEM}_T \, dT \quad (3.7)$$

We calculate the DEM map,  $\xi_{xyT}$ , using `eit_dem_tool.pro` provided in Solar Soft which combines the four prepped EIT images described in Section 3 and gives a DEM for each pixel across the full EIT field of view. To co-align  $\xi_{xyT}$  to MOSES we apply the same transformation to each temperature image in the map that we applied to the EIT 304 Å channel when co-aligning to the MOSES zero order image. We normalize the DEM map by its average DEM over the MOSES field of view because we are more concerned with the spatial distribution of intensity, at a given temperature, than the absolute DEM predicted by the code. Also, starting with a normalized DEM map allows us to use a each temperature bin in the DEM as the free parameters in our fit.

In order to create a synthetic MOSES image at each spectral order we must combine  $\xi_{xyT}$  with spectral information. Using the Chianti database we generate a synthetic line list

using a constant log pressure of  $15 \text{ K cm}^{-3}$ , Feldman coronal abundance (Feldman, 1992), and a flat log DEM,  $\log \text{DEM}(T) = 1 \text{ cm}^{-5} \text{ K}^{-1}$ . Leaving the line list unsummed in temperature gives the intensity as a function of temperature for each spectral line in the passband,  $G_{\lambda T}$ . Combining  $G_{\lambda T}$  with  $\xi_{xyT}$  and the wavelength dependent MOSES throughput,  $\alpha_{m\lambda}$ , yields an image for every spectral line at every temperature,  $I'_{xy\lambda T}$ . The MOSES throughput is defined by the periodic metallic multilayer coatings on the MOSES primary and secondary optics, as well as the thin film aluminum filters just before the detector.

The MOSES grating has a spectral dispersion of  $\delta = \approx 29 \text{ m}\text{\AA}$  per pixel. Therefore in order to produce a set of images for each of the three MOSES spectral orders,  $m = -1, 0, 1$ , line images,  $I'_{xy\lambda T}$ , must be shifted along x. Each image is shifted by  $n$  pixels where  $n = \frac{m\lambda - 303.78}{\delta}$ . This results in no shift for the central,  $m = 0$  order, and an equal and opposite shift in the outboard orders,  $m = -1$  and  $1$ . When shifting line images to form the outboard orders we allow features out side the field of view defined by the MOSES zero order to shift into the field of view, which is possible since each EIT image is full disk. This mimics the behavior of the actual MOSES optical system since MOSES does not have a stop to strictly enforce its FOV, therefore making it is possible for highly shifted features to exist in the outboard orders that aren't captured by the ESIS zero order and vice versa. After the line image at each temperature is shifted we sum each order in wavelength to form an image in each order at every temperature bin,  $I'_{mxyT}$ .

Final synthetic MOSES images are formed at each order by multiplying the temperature dependent cube by a DEM of choice and integrating in temperature. This gives 3 synthetic MOSES images from which we can form difference images and cross correlate (Equation 3.1). Using each temperature bin of the DEM as a free parameter, we seek to minimize the least squares difference between synthetic and MOSES mean cross-correlation function, yielding closely matching synthetic MOSES data with known spectral content.

When comparing our synthetic data to MOSES we slightly blur each MOSES image

prior to taking the difference and cross-correlating using a normalized Gaussian kernel with a standard deviation of four pixels. This ensures small scale features in the MOSES images (that aren't indicative of spectral contamination) don't impact the fit. During testing it was found that the width of the kernel used had little impact on the final results (a few percent difference in final spectral content), therefore a standard deviation of 4 pixels was chosen based on a factor of  $\approx 4$  difference in resolution between EIT and MOSES, and visual comparison of small scale features in the resulting, blurred, difference images.

In the following section we show the DEM of best fit to the MOSES data, as well as the resulting synthetic difference images and total spectral content.

### Results

Using the forward model described in the previous section we have generated synthetic MOSES images with a known spectral content that best fit the MOSES data. We achieved a best fit by varying the emission measure at each temperature prior to integrating, and then comparing the cross-correlation of the synthetic difference images to that of the MOSES difference images. The DEM of best fit is shown in Figure 3.6.

We find good agreement between our synthetic data of best fit and the MOSES data. Figure 3.7 compares the mean cross-correlation of the difference image rows from the slightly blurred MOSES data, to same cross-correlation of the synthetic data. Comparing the two curves shows notable agreement in a few places including around zero lag and all positive lags. Negative lags match less closely, although the shape between zero and approximately -600 pixels is similar. Considering that we have attempted to use a single DEM to represent the quiet Sun over a very large field of view, we think the agreement is remarkable.

A synthetic difference image of best fit ( $I'_{+1}$  minus  $I'_0$ ) is shown along with the corresponding MOSES difference image in Figure 3.8. In the synthetic difference image each feature identified in Figure 3.1 has been successfully reproduced. The dark imprint

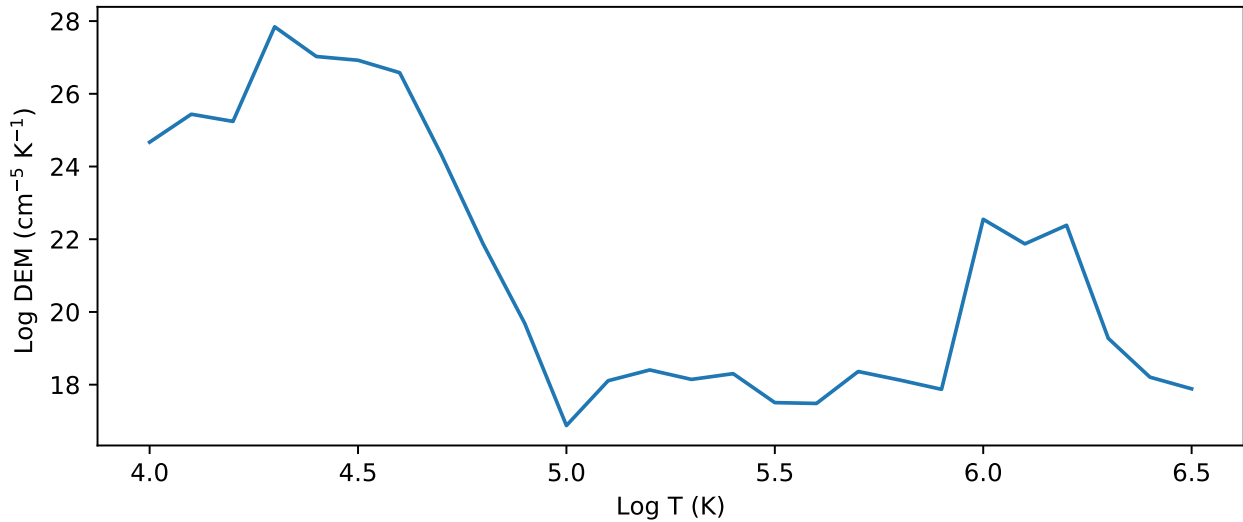


Figure 3.6: Best fit DEM used to generate the final synthetic MOSES images.

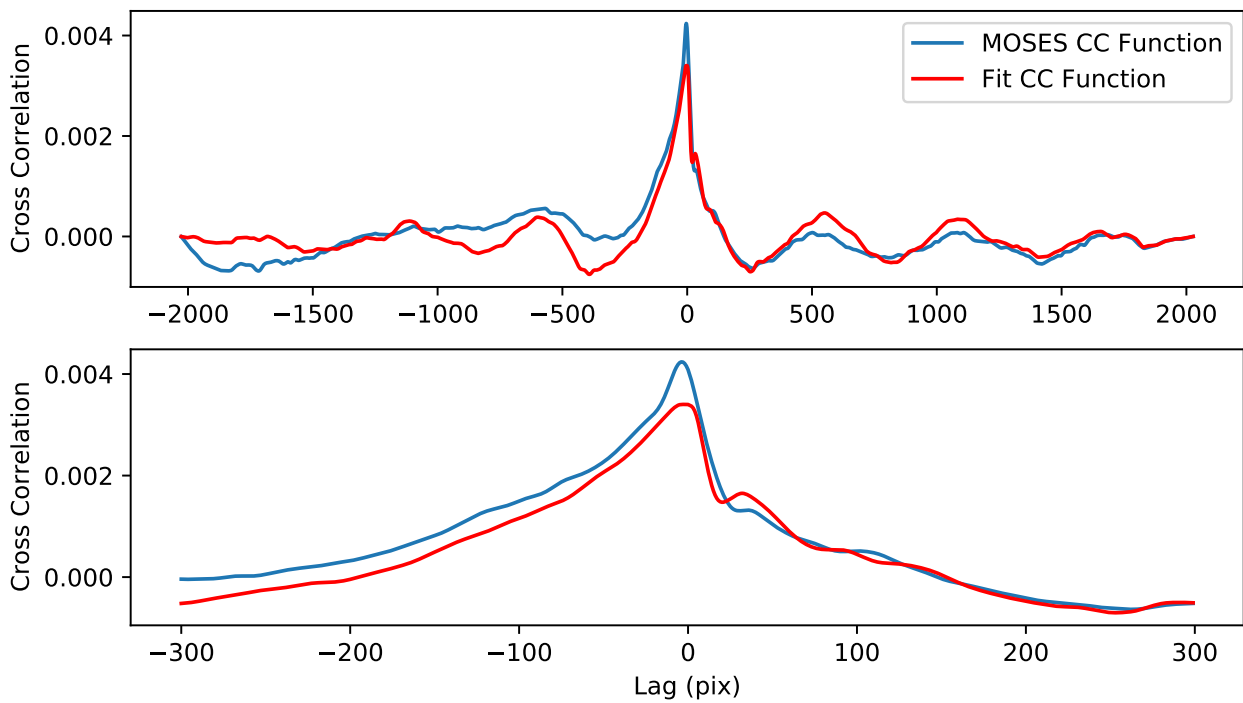


Figure 3.7: The top panel shows the entire mean cross-correlation along image rows of the MOSES (blue) and synthetic (red) difference images. The bottom panel shows a zoomed in view of the same function in order to highlight features near zero lag.

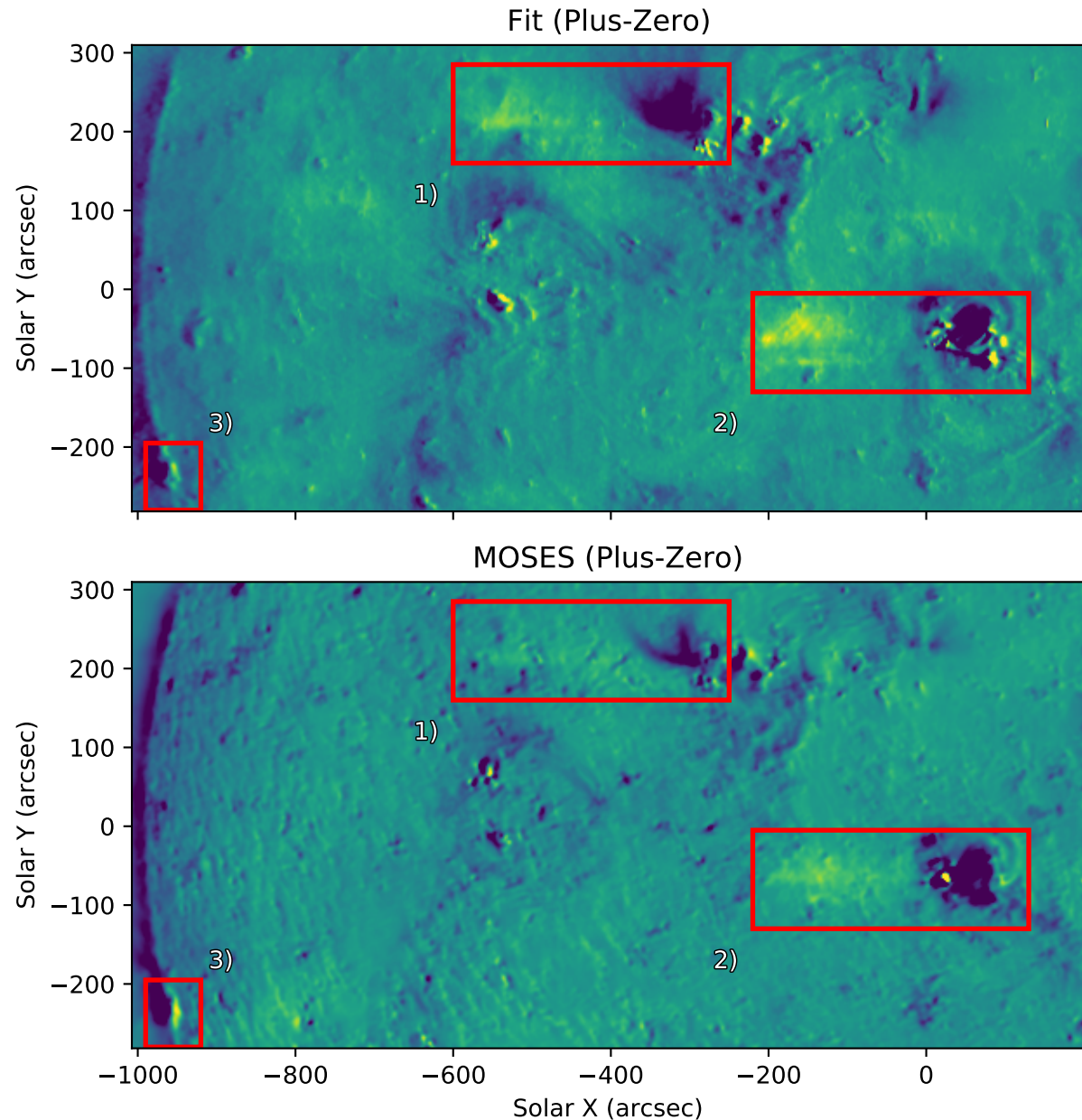


Figure 3.8: The  $I_{+1} - I_0$  difference image, also shown in Figure 3.1c, along side the same difference image prepared from the synthetic MOSES images of best fit. Identical regions 1-3 are boxed in each image for comparison.

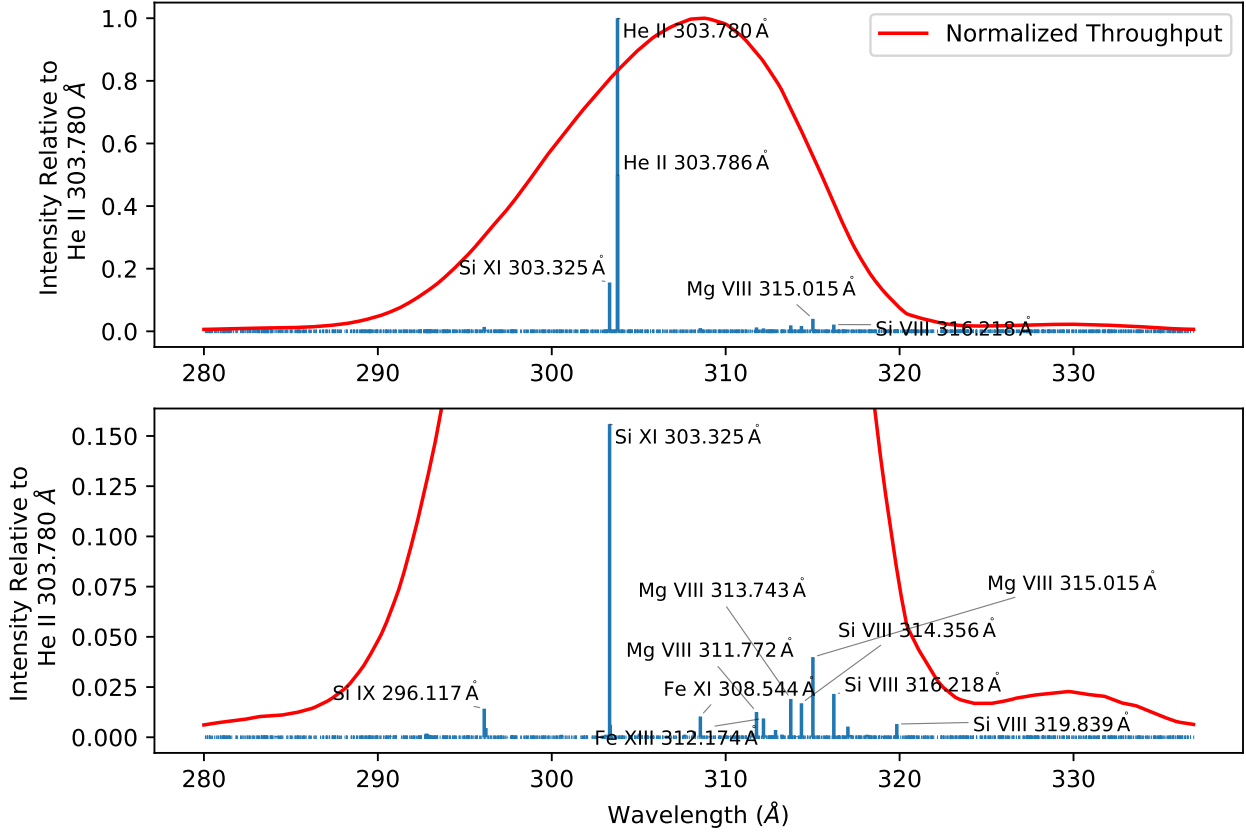


Figure 3.9: Using the DEM of best fit shown in Figure 3.6 we generated the above synthetic spectrum using Chianti. Each line intensity has also been weighted by the wavelength dependent throughput of the MOSES optical system (normalized and shown in red).

of the “wishbone” (region 1) and nearby active region (region 2), are clearly visible and are adjacent to lighter smears of intensity to their left. Region 3, while not as sharp in the synthetic images, is reproduced at the limb with the same close separation between the positive and negative lobes.

Using the DEM of best fit we also generated an average spectrum for the MOSES data weighted by instrument’s the wavelength dependent throughput (Figure 3.9). The synthetic spectrum of best fit was generated using the same constant pressure, abundance file, and spectral range as was used in the forward model (Section 3). MOSES images are dominated by the He II doublet near 303.7 Å. Si XI 303.3 Å, while much dimmer than He II, has the

Table 3.1: Average MOSES Image Spectral Content

Ion	Contribution
He II	80.55%
Si XI	8.37%
Mg VIII	4.14%
Si VIII	2.65%
Si IX	1.33%
Fe XIII	1.29%
Other	1.67%

second highest intensity and represents approximately 8 percent of the total intensity. The other notable, and unexpected contribution to the image intensity is from the host of lines between 310 and 320 angstroms, the brightest being from Mg VIII and Si VIII. Table 3.1 shows the total intensity contribution from each of the brightest ions.

### Discussion and Conclusions

MOSES was successful in its goal of capturing solar images in the He II 303.8 Å emission line. Despite the use of a narrowband multilayer coating on both the primary and secondary optics, MOSES captured several solar features not easily attributed to the dominant He II 303.8 Å or nearby strong Si XI 303.3 Å lines. In order to identify and quantify the spectral content of these additional features we cross-correlated two MOSES difference images and identified peaks in correlation as significant and indicative of spectral contamination. Using a forward model that combines four co-temporal EIT images with synthetic spectra from Chianti we created synthetic MOSES difference images with known spectral content that could be cross-correlated and compared to the MOSES difference image cross-correlation

function. By varying the DEM used we modified the spectral content of the synthetic MOSES data until we minimized the differences between the synthetic and real cross-correlation functions, the results of which are displayed in Section 3.

Compared to other solar DEMs, like those included in the Chianti software package, our DEM of best fit (Figure 3.6) shows a huge increase in emission measure between  $\log T = 4\text{-}5\text{ K}$ . This result is artificial and is caused by a significant lack of modeled intensity in the He II 303.8 Å emission line when using Chianti. The He II 303.8 Å intensity is low by up to an order of magnitude when modeled under classical assumptions, and its lack of emission has been attributed to a host of factors including a lack of ionization equilibrium (Golding et al., 2017). Since the MOSES passband is absent of any other bright, cool lines (<.1 MK) our fit can increase the emission measure at low temperatures resulting in an increase in the intensity of He II 303.8 Å alone, allowing for a more accurate intensity ratio between it and nearby hot emission lines like Si XI 303.3 Å. We find an average line ratio between He II 303.8 Å and Si XI 303.3 Å intensities of  $\approx 10:1$  which is comparable to ratios measured by other slit spectrographs in regions of moderate solar activity (Cushman & Rense, 1978).

It is also important to note that although we chose to use a DEM as the basis of our fit, we do not consider it to be an accurate average DEM of the sun across the MOSES field of view. The formation temperatures of lines within the MOSES passband very sparsely cover the range of  $\log T = 4\text{-}6.5$ , allowing multiple DEMs to represent the same spectral content. Despite the parameter space being very degenerate, we chose to vary emission measure rather than individual line intensities to ensure our final fits have physically realizable line ratios.

The temperature coverage of EIT, used to create the synthetic data, is also very sparse. Luckily, the dominant line in each of the four included EIT images have peak formation temperatures that closely match the peak formation temperatures of the brightest lines imaged by MOSES. The four EIT channels used, He II 304 Å, Fe IX 171 Å, Fe XII 195 Å, Fe XV 284 Å, have peak formation temperature of  $\log T = 4.7\text{ K}$ ,  $5.9\text{ K}$ ,  $6.2\text{ K}$  and  $6.3\text{ K}$

respectively, calculated using Chianti. The bright, hotter lines imaged by MOSES, namely from Mg VIII, Si VIII, and Si XI, have peak formation temperatures of  $\log T = 5.9\text{ K}$ ,  $5.95\text{ K}$ , and  $6.2\text{ K}$  respectively. This allows for synthetic MOSES data with key intensity contributors well represented, as is evident when comparing features in the synthetic difference images of best fit to those in the MOSES difference images (Figure 3.8).

The most mysterious features in the MOSES difference images, those that motivated this study, are regions 1 (the “wishbone”) and 2 identified in Figures 3.1 and 3.8. These two features are very coronal in appearance and easily identifiable in the hotter EIT channels, but they cannot be attributed to the most obvious source of contamination in any He II image, Si XI  $303.3\text{ \AA}$ , due to the lack of positive component  $\approx 15.7$  pixels away like that seen in region 3. The presence of a faint, light smear left of the wishbone indicates that it is from emission at longer wavelengths than He II  $303.8\text{ \AA}$ , but a lack of clear positive wishbone makes it difficult to attribute it to a single contaminant line. The best fit spectrum (Figure 3.9) shows a host of lines between 310 and 320 angstroms, mostly emitted by the Mg VIII and Si VIII ions, the strongest being Mg VIII  $315\text{ \AA}$  (Also identified by Rust (2017)). Despite their individually weak intensity, combined they contribute on order the same intensity as Si XI  $303.3\text{ \AA}$ . Due to spectral dispersion, these lines are very faint in the MOSES outboard order and could likely be neglected. In the zero order image, all of these faint lines land in the same place on the detector which is why these features appear so clearly when subtracting the zero order. The intensity contribution from lines other than He II  $303.8\text{ \AA}$  and Si XI  $303.3\text{ \AA}$  amounts to around ten percent of the total intensity in the zero order and comes from tens of lines that may be easily overlooked during analysis or instrument development. Some of these lines are shifted hundreds of pixels, causing feature within the field of view of the MOSES zero order to be shifted out and those outside to be shifted in the outboard orders. This results in different total intensities existing in each spectral order, which could lead to confusion when comparing orders during inversion.

While overlapping intensity from different spectral lines is inevitable in this type of instrument, the use of a zero order (undispersed) image and a lack of clearly defined field of view in MOSES exacerbates the problem of spectral contamination. ESIS (Parker et al., 2021; Smart et al., 2021), our second-generation rocket borne slitless spectrograph, builds off the MOSES concept and improves on it in several ways. The most relevant improvements include an intermediate focal plane and field stop, that clearly defines the instrument field of view, and four channels rather than three, none of which is undispersed. Including a field stop defines the same field of view for every channel and solves the problem of highly shifted features existing in some orders, but not others. Even with a clearly defined field of view features in the zero order image would still have intensity from lines that are dispersed off the detector in the outboard orders. The ambiguity of spectral content makes it difficult to compare its intensity to outboard orders without DEM forward modeling. Using all dispersed orders, as is done in ESIS, makes it much easier to compare the intensity of solar features from specific emission lines, and tends to reduce the effect of contaminant lines on measured intensity by dispersing them across the image. We think this approach will prove particularly advantageous with a high dispersion instrument whose chief science objective is to resolve the profiles of strong lines. The considerations are rather different when the instrument is designed from the start to reconstruct DEMs, as with COSIE (Winebarger et al., 2019).

In the MOSES design, the zero order was intended to improve the spatial resolution, which is otherwise blurred by the line profiles in the horizontal direction. It served very effectively in this role. With ESIS, we oriented the dispersion of its four channels in four different directions. Each ESIS channel has its highest resolution in the direction perpendicular to the dispersion, and together they are able to separate closely spaced features with any orientation. As our inversion skill improves, we will learn whether this approach to high resolution imaging is as successful as the zero order.

In summary, we have developed a forward model of the MOSES instrument that

combines the Chianti database and images from EIT to form synthetic MOSES data with known spectral content. Our fits match the MOSES data well and indicate that the unexpected solar features identified in MOSES difference images are composed of tens of dim lines that, in the aggregate, contribute approximately 10 percent of the average intensity in the zero order image and are smeared over many hundreds of pixels in the outboard orders. This unexpected spectral content makes it difficult to compare the intensity of certain features between spectral orders and, if not properly accounted for, could lead to poor convergence when inverting slitless spectrograph data. Our analysis led us to comment on the advantages and disadvantages of zero order imaging in a slitless spectrograph. These considerations should aid in the design of future instruments of this type.

#### Acknowledgments

This work was supported primarily by NASA Grant NNX14AK71G, NNX07AG76G, and NNX12AD79G. CHIANTI is a collaborative project involving George Mason University, the University of Michigan (USA), University of Cambridge (UK) and NASA Goddard Space Flight Center (USA).

## FIRST FLIGHT OF THE EUV SNAPSHOT IMAGING SPECTROGRAPH (ESIS)

Contribution of Authors and Co-Authors

Manuscript in Chapter 4

Author: Jacob D. Parker

Contributions: Led manuscript preparation and wrote most of the text unless otherwise noted. Constructed Level 3 data product, prepared and analyzed different images/movies and selected events for analysis. Performed MART inversion.

Author: Roy Smart

Contributions: Prepared the Level 0 and 1 data products, as well as described them in the manuscript. Prepared Figures 4.1, 4.2, and 4.4 and data for Table 4.2. Prepared the despiking routine along side Charles Kankelborg. Guided Nelson Goldsworth and Jacob Parker through implementing Charles Kankelborg's MART algorithm in Python, as well as contributed code himself. Assisted in writing text associated with the described tasks.

Author: Charles Kankelborg

Contributions: Instrument P-I. Provided assistance in both study design and implementation throughout the process. Contributed text to the introduction and conclusion sections, as well as assisted heavily with editing the manuscript.

Author: Amy Winebarger

Contributions: Instrument Co-I. Contributed text to the introduction and mission section. Helped guide the study and provided valuable feedback every step of the way.

Author: Nelson Goldsworth

Contributions: Contributed a large amount of python code for the MART algorithm, as well as performed a considerable amount of testing, guided by Charles Kankelborg and Roy Smart, prior to use on the ESIS Level 3 data.

Manuscript Information

Jacob D. Parker, Montana State University

Roy Smart, Montana State University

Charles Kankelborg, Montana State University

Amy Winebarger, NASA Marshall Space Flight Center

Nelson Goldsworth, Montana State University

Astrophysical Journal

Status of Manuscript:

- Prepared for submission to a peer-reviewed journal
- Officially submitted to a peer-reviewed journal
- Accepted by a peer-reviewed journal
- Published in a peer-reviewed journal

Abstract

The Extreme ultraviolet Snapshot Imaging Spectrograph (ESIS) was launched on a sounding rocket from White Sands Missile Range on September 30, 2019. ESIS is a Computed Tomography Imaging Spectrograph (CTIS) designed to capture both spectral and spatial information simultaneously over a large field of view to provide velocity information on small scale transient events that are prevalent at transition region temperatures. In this paper, we review the ESIS instrument, mission, and the data captured. We demonstrate how this unique data set can be interpreted qualitatively, and further present some initial quantitative inversions of the data. Using a Multiplicative Algebraic Reconstruction Technique (MART) we are able to combine information from all four ESIS channels into a single spatial-spectral cube at every exposure. We analyze two small explosive events in the O V 629.7 Å spectral line with jets near  $\pm 100$  km/s that evolve on 10 s time scales and vary significantly over small spatial scales. Intriguingly, each of these events turns out to be a bimodal (red+blue) jet with outflows that are asymmetric and unsynchronized. We also present a qualitative analysis of a small jet-like eruption captured by ESIS, and draw early comparisons to previously observed mini-filament eruptions. In the 5 minutes of observing time, ESIS captured the spatial and temporal evolution of tens of these small events across the  $\approx 11.5'$  field of view, as well as several larger extended eruptions, demonstrating the advantage of CTIS instruments over traditional slit spectrographs in capturing the spatial and spectral information of dynamic solar features across large fields of view.

Introduction

Observationally, the solar transition region (TR) refers to the portion of the solar atmosphere at temperatures between 20,000 K and 800,000 K. Initially, the transition region was viewed as simply the thin interface region between the dense, cool chromosphere and

tenuous, million-degree corona, where the temperature of the plasma dramatically increased two orders of magnitude over tens of kilometers (see Tian, 2017, and references therein). Though undoubtedly this type of transition region exists in hot coronal loops, the concept of the transition region has been expanded over the last twenty years to include a dynamic and complicated three-dimensional geometry.

The transition region is rife with magnetically driven phenomena such as explosive events (e.g., Dere et al., 1991) and microflares (Gontikakis & Winebarger, 2012) which manifest supersonic flows. Explosive events were discovered in rocket flights (Dere et al., 1989). Explosive event outflows are typically of order  $\pm 100$  km/s. The release of free magnetic energy in the low- $\beta$  plasma was implicated because these flows are much faster than the TR sound speed (e.g.,  $\approx 55$  km/s for C IV, formed at  $10^5$  K). Explosive events have been found to present in different ways and have been observed by many instruments since their original discovery. Innes et al. (1997) found fast bi-directional jets in Si IV 1394 Å line profiles taken by the Solar Ultraviolet Measurements of Emitted Radiation instrument (SUMER) (Wilhelm et al., 1995) separated by a few arcseconds and inferred they must be associated with the outflows of an inclined reconnection current sheet. Higher resolution observations from the Interface Region Imaging Spectrograph (De Pontieu et al., 2014, IRIS) have shown that Si IV line profiles often show very bright line cores with broad wings and very non-gaussian, more triangular profiles. This enhanced line core emission points to a larger amount of stationary plasma, and has been attributed to the presence of a dominate Tearing Mode Instability during the reconnection (Innes et al., 2015). Enhanced emission in the line core of a larger explosive event viewed in He II 303.8 Å by the Multi-Order Solar Extreme-ultraviolet Spectrograph (MOSES) has also been attributed to the tearing mode instability (Fox et al., 2010) despite tens of smaller events in the same data having clear bi-modal profiles (Rust & Kankelborg, 2019). In order to determine which, if any, of these presentations is typical we require high cadence velocity data over a wide range of temperatures simultaneously,

something difficult to achieve even in multi-instrument studies.

Investigations of TR events to date are severely limited by available observational capabilities. Historically, slit spectrographs have been used to determine velocity of the plasma in the solar atmosphere. Spectrally resolved images of the sky plane must be built by rastering the slit over the region of interest, which takes much longer than the timescales of TR phenomena and confuses whether events are evolving temporally or varying spatially.

One solution to simultaneously capture spatial and spectral information over a large field of view is to use a slitless imaging spectrograph. The data from these instruments, sometimes called overlapograms, have spatial and spectral information overlapped in the dispersive direction, requiring the data to be inverted or unfolded. The difficulty in unfolding slitless spectrograph data has limited its usefulness for extended astrophysical objects like the Sun. Only two satellite missions have routinely captured solar slitless spectrograph data: The S082A instrument on *Skylab* (Tousey et al., 1973) and the Res-K instrument of the Russian KRONOS-I mission (Zhitnik et al., 1998), though others have been recently developed and proposed (Golub et al., 2020; Winebarger et al., 2019). Additionally, the currently-operating Extreme-ultraviolet Imaging Spectrograph (EIS; Culhane et al. (2007)) on the *Hinode* mission (Kosugi et al., 2007) includes 40'' and 266'' slots that can produce overlapogram data. Though EIS slot data are not often studied quantitatively, they have been used as a flare trigger and since analyzed to aid in interpretation of impulsive phase of solar flares (Harra et al., 2020, 2017). In addition to these satellite observatories, the Multi-Order Solar EUV Spectrograph (MOSES) instrument by Kankelborg and collaborators (Fox et al., 2010; Kankelborg & Thomas, 2001; Rust & Kankelborg, 2019) has observed dynamic events in the solar transition region. MOSES captured the zero and plus and minus one order of the He II 303.8 Å line simultaneously. Doppler shifts were then detected as the spectral displacements in opposite directions in the  $\pm 1$  orders.

Slitless spectrograph data can be thought of as a projection of a three dimensional

spatial-spectral data cube,  $I(x, y, \lambda)$ , onto a two dimensional detector. Although *Skylab* S082A had just a single projection through  $x, y, \lambda$ -space, it was possible under some circumstances to determine line intensities and line ratios (e.g., Keenan et al., 1988, 2006; Tayal et al., 1989), and even Doppler shifts (Mariska & Dowdy, 1992).

Slitless spectrographs using two projections (usually one dispersed, and one undispersed) have proven sufficient to implement an efficient ground-based magnetograph (DeForest et al., 2004), map Doppler shifts in the solar transition region (Courrier & Kankelborg, 2018), and invert temperature or density information (Winebarger et al., 2019). However, as with any tomographic inversion problem (e.g., Kak & Slaney, 2001), the fidelity of reconstruction improves dramatically as projections are added. This is particularly true as the complexity of the object increases, causing the overlap of multiple features along the projection. An instrument that captures multiple projections of the spatial-spectral data cube is called a Computed Tomography Imaging Spectrograph (CTIS, Descour & Dereniak, 1995). MOSES is an example of a CTIS, as it captured three projections in the  $\pm 1$  and 0 orders. Fox et al. (2010) was able to extract line widths and Doppler shifts from a relatively complex explosive event observed by MOSES in He II 303.8 Å. Rust & Kankelborg (2019) found unambiguous evidence of explosive events with well resolved, double-peaked spectral line profiles in the same data set.

In 2013, the Extreme-ultraviolet Snapshot Imaging Spectrograph (ESIS) was proposed to the NASA Low Cost Access to Space (LCAS) program and subsequently selected. ESIS is a CTIS with four unique projections of the spatial-spectral data cube and is designed to capture velocity information in small-scale reconnection events in the O V 629.7 Å emission line that is formed in the solar transition region. ESIS builds off of the MOSES concept, but adds an additional projection, the ability to independently focus each channel, and an explicit field of view defined by the field stop, a significant upgrade in flexibility and data quality over MOSES. ESIS was launched along with MOSES from White Sands Missile

Table 4.1: Dominant spectral lines observed by ESIS. Intensities are relative to O V 629.7 Å.

Ion	$\lambda$ (Å)	Intensity
He I	584.33	0.70
O III	599.59	0.13
O IV	608.40	0.06
Mg X	609.79	0.25
O IV	609.83	0.11
Mg X	624.94	0.13
O V	629.73	1.00

Range on September 30, 2019. Unfortunately the MOSES shutter failed to open during the flight and did not collect any solar images as a result. Therefore, this paper is a description of the ESIS mission, data and preliminary results. The ESIS experiment, target, and flight is described in Section 2. Section 3 provides information on the data processing. Preliminary results are given in Section 4; these include both qualitative and quantitative measures of small-scale velocity events in the solar transition region. The ESIS mission was successful in observing tens of small-scale reconnection events over the short rocket flight, as well as demonstrating the usefulness of CTIS observations and developing the analysis techniques required to interpret this unique data.

### ESIS Mission

In this section we provide an overview of the ESIS experiment as well as the time and conditions of the ESIS rocket launch and subsequent data collection.

## The Experiment

The full ESIS experiment includes an optical instrument, a set of detectors, an on board data acquisition system, and ground support equipment and is described in great detail in the preceding paper (Smart et al., 2021). The ESIS optical design consists of a single parabolic primary mirror, an octagonal field stop placed at an intermediate focal plane, and 4 spherical diffraction gratings each with their own corresponding CCD detector. Incoming light is focused by the primary mirror onto the octagonal field stop. The octagonal field stop is  $\approx 5$  mm wide, which is equivalent to  $11.5'$  when projected onto the sky. The light that exits the field stop is reimaged by the four spherical diffraction gratings onto their own CCD. The portion of the solar spectrum that is captured by each detector ranges from  $\approx 584 \text{ \AA}$  to  $630 \text{ \AA}$ . Table 4.1 shows the dominant lines observed by ESIS. Intensities relative to O V  $629.7 \text{ \AA}$  are calculated using Chianti (Del Zanna & Young, 2020; Dere et al., 1997) assuming a constant log pressure of  $15 \text{ K cm}^{-3}$  and a quiet sun DEM, combined with the Schmeltz 2012 abundance file (Schmelz et al., 2012). While this paper focuses primarily on the dominant O V  $629.7 \text{ \AA}$  spectral line, future work will be focused on measuring plasma velocity in other bright lines.

Each grating and detector pair, referred to as a channel in this paper, is itself an independent slitless imaging spectrograph. The channels are arrayed at  $45^\circ$  increments about the axis of symmetry of the paraboloidal primary mirror such that each channel disperses the solar image a different direction. Hence, each of these channels capture a unique projection of the spatial spectral cube, shown in Figure 4.1. As shown, each channel captures the Sun imaged through the octagon and dispersed at different relative angles with respect to solar north. Combining these four channels creates a CTIS. Exposures from all four channels are gathered nearly simultaneously by triggering the frame transfer in three of the cameras by a single “master” camera. The ESIS instrument currently has 4 channels, but is built to accommodate up to 6 (limited by interference with the optical bench).

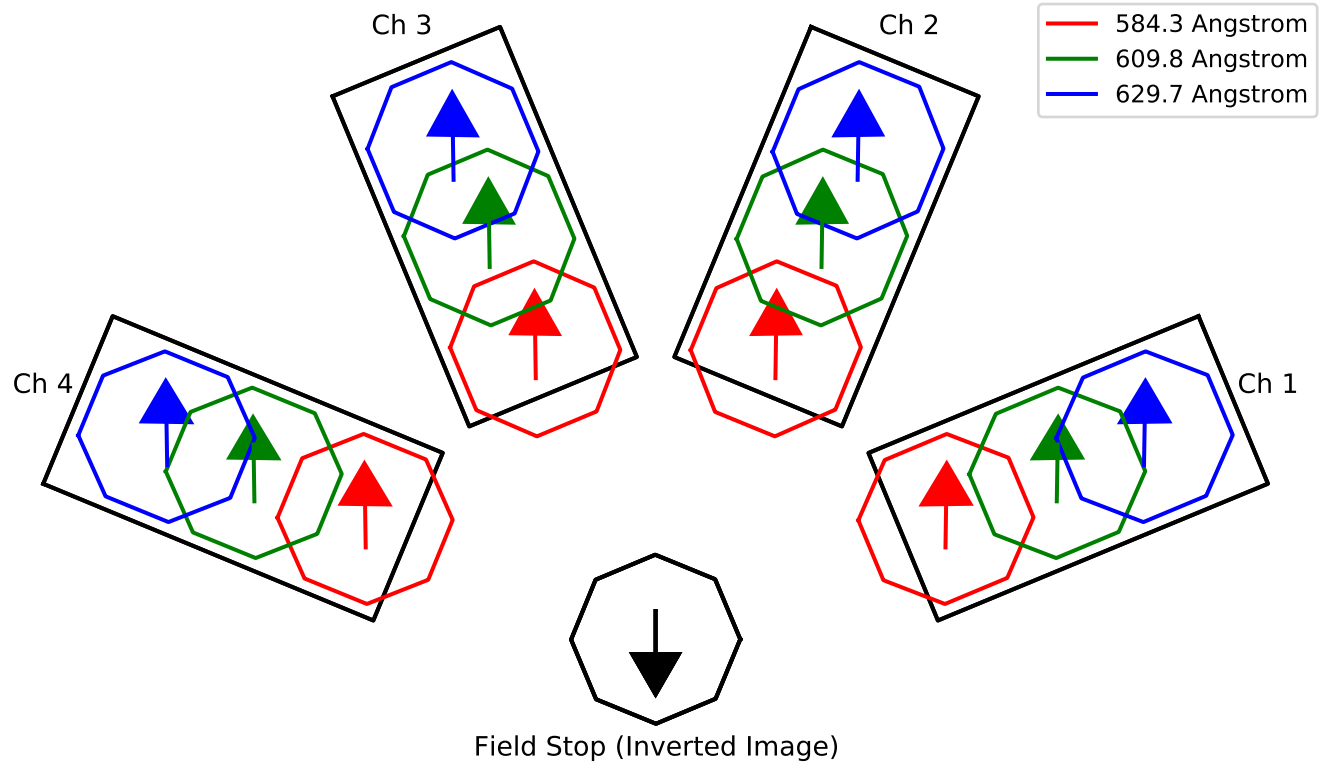


Figure 4.1: A modeled layout showing the orientation of each ESIS channels' detector relative to the solar image at the octagonal fieldstop. The locations of the brightest wavelengths (He I 584.3 Å, Mg X 609.79 Å, and O V 629.7 Å) in the passband are shown on each detector. The HeI 584.3 Å line extends off the detector edge by design, as can be seen in Figure 4.4.

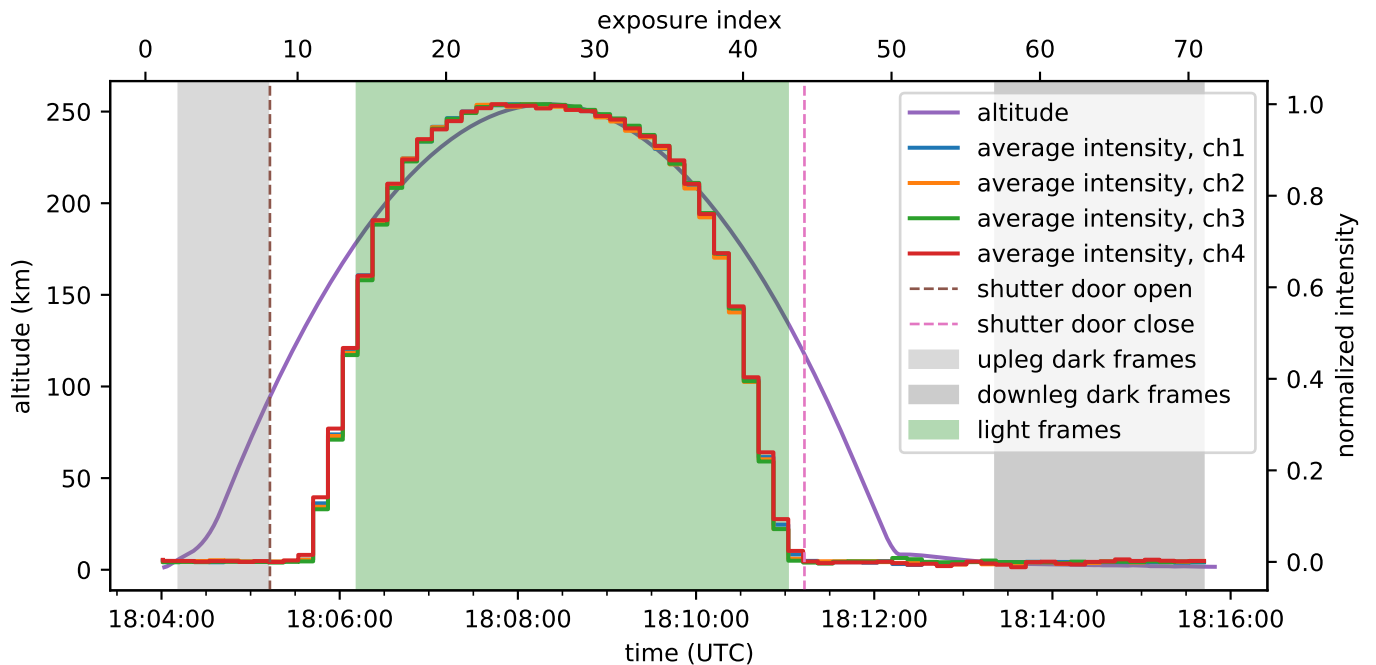


Figure 4.2: The altitude of the ESIS rocket determined from White Sands Missile Range radar data as a function of elapsed time from launch. The event times listed in Table 4.2 are labeled.

### Launch and Data Collection

ESIS was launched at 18:04:00 UTC on September 30, 2019 from White Sands Missile Range. Figure 4.2 provides the height of the sounding rocket as a function of time, determined from radar measurements, as well as several key events during the flight. The ESIS cameras began exposing at launch and continued to record full detector ( $\sim 2k \times 1k$ ) images with a 10 s exposure and cadence throughout the flight. Images taken while the experiment shutter door was closed (i.e., during the initial boost phase of the rocket flight, and ballistic ascent to approximately 100 km altitude) serve as darks. At 73.0 s after launch, the shutter door opened. The Sun was acquired by the Solar Pointing And Rocket Control System (SPARCS) and the ring laser gyro (RLG) was enabled at 124.2 s indicating the rocket was in Fine Pointing Mode. During this mode, SPARCS maintained a constant

target; however, thermal expansion of optical components inside the instrument caused the apparent drift of the solar image on the detectors, as described in Section 3. At 433.0 s, the shutter door closed ending solar observations. Exposures continued until the system shutdown at 18:15:41, providing several additional dark frames at the end of the flight. A summary of the flight and data collected is given in Table 4.2.

September 30, 2019 was a very quiet day on the Sun. In fact, the last B-class event detected by GOES (Chamberlin et al., 2009) prior to the ESIS launch was July 7, 2019. Because of this exceptionally quiet period on the Sun, we chose to point at disk center. The actual pointing of the center of the ESIS octagonal field stop and roll were found after flight by comparing the ESIS exposure nearest apogee at 18:08:17 UTC to the closest 304 Å image in time taken by the Atmospheric Imaging Assembly (AIA Lemen et al., 2012), taken at 18:08:17 UTC. The ESIS field of view projected onto the AIA 304 Å image is shown in Figure 4.3 as a green octagon. The pointing was found to be  $\approx [18'', -19'']$  and the roll offset was found to be  $\approx 0.85^\circ$  (clockwise about Sun center), both within the tolerances for SPARCS pointing. Figure 4.3 shows the full-disk AIA 304 Å image. The ESIS FOV is indicated by the octagon.

Each of the ESIS cameras collected 71 images during flight. The first two images are unusable; the first image has an exposure time of 0 s and is basically a dump of the dark current in the camera, while the second image has an exposure time slightly longer than 10 s caused by the cameras syncing to a single trigger of the master camera. All the other images have a 10 s exposure time. 29 of these images were light frames, meaning the shutter door was open and the RLG was enabled. The time during the rocket flight when light frames were collected is shaded green in Figure 4.2. Light emitted by the Sun is absorbed by the Earth’s atmosphere. The degree of absorption depends upon the column of the atmosphere that the telescope is looking through. The wavelength dependence of atmospheric absorption is weak, on the order of a few percent across the ESIS passband. Figure 4.2 shows the mean

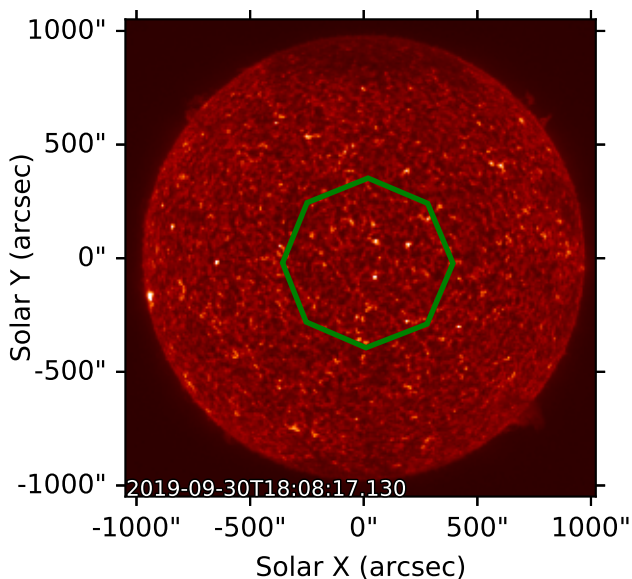


Figure 4.3: The reference AIA 304 Å data taken at 18:08:17 UTC was used for determining the absolute pointing. The octagon indicates the ESIS FOV.

intensity in each of the ESIS channels as a function of time. Atmospheric absorption clearly impacted the observations in the up and down legs of the flight. Accounting for atmospheric absorption will be discussed in Section 3. Though there are 29 light frames, the first and last several frames were greatly impacted by atmospheric absorption and have limited usefulness. As the rocket was re-entering the atmosphere, a transient signal affects some of the images that would otherwise be considered darks. It is likely due to violent deceleration when the payload encountered Earth’s atmosphere. This effect can be seen as the small bump in the mean intensities at roughly 18:12:20 in Figure 4.2. We restrict the dark frames to the data taken after the first two images, but before the shutter door opened in the upleg, and after the transient in the downleg; these times are shaded with gray in Figure 4.2. In total there were 20 usable dark images.

Table 4.2: ESIS Flight Data Summary

Launch Date	September 30, 2019	Image Size	(1040, 2048) pix
Data Acquisition Time	18:04:00–18:15:41 UTC	Avg. Noise:	$4.02 \pm 0.14$ adu
Pointing	$\approx [18'', -19'']$	Avg. Gain	$2.56 \pm 0.03$ e <sup>-</sup> adu <sup>-1</sup>
Field of View	$\approx 11.5'$ octagonal	Exposure Time	10 s
Roll	$\approx 0.85^\circ$ CW	No. Light Exp:	29
Spatial Plate Scale	[0.74, 0.77] " pix <sup>-1</sup>	No. Dark Exp:	20
Spectral Plate Scale	0.037 Å pix <sup>-1</sup>	Analog-Digital Unit (adu)	

Data

We have established several levels of data processing that are described in detail below. Level 0 represents the raw data that was obtained by the four different cameras during flight. Level 1 data incorporates a quadrant dependent bias and gain correction, cropping of non-active pixels, and dark subtraction. Normally, for solar observatories like AIA, higher level data would be further corrected for solar pointing and roll by interpolating the data onto a common grid, referenced to solar coordinates.<sup>1</sup> For ESIS this step would be complicated, and would not be the best treatment of the data. First, the spatial-spectral overlap on the detector complicates the notion of image alignment. Second, interpolation inherent in such geometrical corrections degrades spatial resolution unnecessarily. Finally, the ESIS optics slightly distort the solar image, mainly due to the tilt of each CCD and also anamorphic magnification by the gratings, which occurs along the dispersion direction for each channel. In fact, the relationship between position and wavelength in each pixel

---

<sup>1</sup>See the Guide to SDO Data Analysis, [http://helio.cfa.harvard.edu/trace/SSXG/ynsu/Ji/SDO\\_Data\\_Analysis\\_guide.pdf](http://helio.cfa.harvard.edu/trace/SSXG/ynsu/Ji/SDO_Data_Analysis_guide.pdf).

depends on distortion parameters which we expect to vary subtly across the field of view, so that the distortion cannot be undone without simultaneously inverting the spatial-spectral cube across all wavelengths. Because of this complication, we define two additional data levels.

Level 2 data will include updated header information with accurate coefficients of a non-linear and wavelength dependent coordinate mapping from solar coordinates and wavelength to each detector for each image. It will also be corrected for atmospheric absorption and contain a header keyword tracking the correction as a function of time for use in instrument noise models. In addition, Level 2 data will be despiked, and store a mask for future respiking. Level 2 data is a necessary step toward inverted data products that cover the full ESIS wavelength range. The Level 2 distortion model must incorporate not only the optical design parameters, but the consequences of small element-by-element misalignments that inevitably occur when an optical system is built up. This model is in active development, hence the Level 2 product will not be described further here.

In lieu of a complete Level 2 product we seek a shortcut to interpretation of the ESIS data, which we will refer to as Level 3. Level 3 data is comprised of a single spectral line cropped from Level 1 data and mapped to the sky plane via a non-linear coordinate transform derived from a coalignment to co-temporal AIA data and an internal coalignment of each ESIS channel to a reference channel. Over the short wavelength range corresponding to a single spectral line (for our present purpose, we will choose O V 629.7 Å), it is quite straightforward to characterize the distortion by comparing the ESIS data to co-temporal AIA 304 Å data. This shortcut allows us to take differences between images and perform simplified inversions that are nevertheless rich in physical detail.

The highest level data product we envision providing in the future, Level 4, is the spatial-spectral data cube, i.e., the intensity as a function of  $[x, y, \lambda]$ , which will be the results of various inversion methods. Since inversions generally do not produce unique solutions, there

may be multiple Level 4 products obtained by different inversion methods.

The Level 0, 1, and 3 data products are described in detail in the remainder of this section.

### Level 0 Data

Level 0 data is the raw data collected during the ESIS rocket flight. Each image was written to a fits files with on-board timestamp, camera number, and other parameters, such as the read out from temperature sensors included in the header.

Each camera includes a detector with 2048 columns and 2064 rows. The detector is operated in frame transfer mode, meaning the exposed portion of the detector is shifted into a storage portion that is read out during the next exposure. The storage portion is simply a mechanically masked region of the detector. The intention was that the storage region would be 520 rows per quadrant while the exposed region would be 512 rows per quadrant, producing an image that was 1024 rows in total. An oversight during implementation inverted the size of the storage and exposed region, meaning the final image had 1040 rows. Having a larger exposed region than storage region implies that eight rows originally exposed at the central portion of the detector were not behind the mechanical mask when the read out was initiated. However, because these rows were only unmasked for roughly 20 ms, as compared to the 10 s exposure time, there was no discernible impact on the data.

The data is read out through 4 ports, corresponding to the four quadrants of the detector. The read out register has 50 additional dummy pixels, or non-active pixels (NAPs), that are read out before each row of the detector data. When the detector is read out, those 50 pixels are stored as part of the image. Two additional “overscan” pixels are read after each row of data and also stored as part of the image. A stored Level-0 data file, then, is  $2152 \times 1040$  pixels. During pre-flight lab testing, it was found that the median intensity in columns 21-50 of the NAPs of each read out port are an excellent proxy for the detector bias.

Additionally the data from each port is converted from analog to digital through a unique circuit. Though the same components were used, slight variations in the circuits caused slight differences in the gain (elec / DN) and read noise associated with each quadrant. The gain for each quadrant in each camera was measured prior to flight. The noise was measured from usable dark images during flight. The average and standard deviations in these values are given in Table 4.2.

### Level 1 Data

A summary of the flight data parameters, as described in the preceding sections, is provided in Table 4.2. For each channel, there were 29 light images that were processed into Level 1 data and 20 dark images used to process the data. Our procedure to convert from Level 0 to Level 1 is described below. An example of a Level 0 and Level 1 image is shown in Figure 4.4.

1. Calculate and subtract the bias of each quadrant of each usable image (light or dark) by taking the median of columns 21-50 of the NAPs for each read out port.
2. Create a master dark image for each channel by taking the median along the time axis of all the bias-subtracted usable dark images.
3. Subtract the master dark from each bias-subtracted light image.
4. Crop each image to remove the non-active and overscan pixels.
5. Convert images from DN to electrons by multiplying each quadrant of each image by the gain for that quadrant.

The resulting Level 1 dataset contains each channel's image sequence in units of photoelectrons. In addition to the images, the Level 1 fits header is updated with the time, exposure length, and altitude associated with each image using standard FITS header keywords.

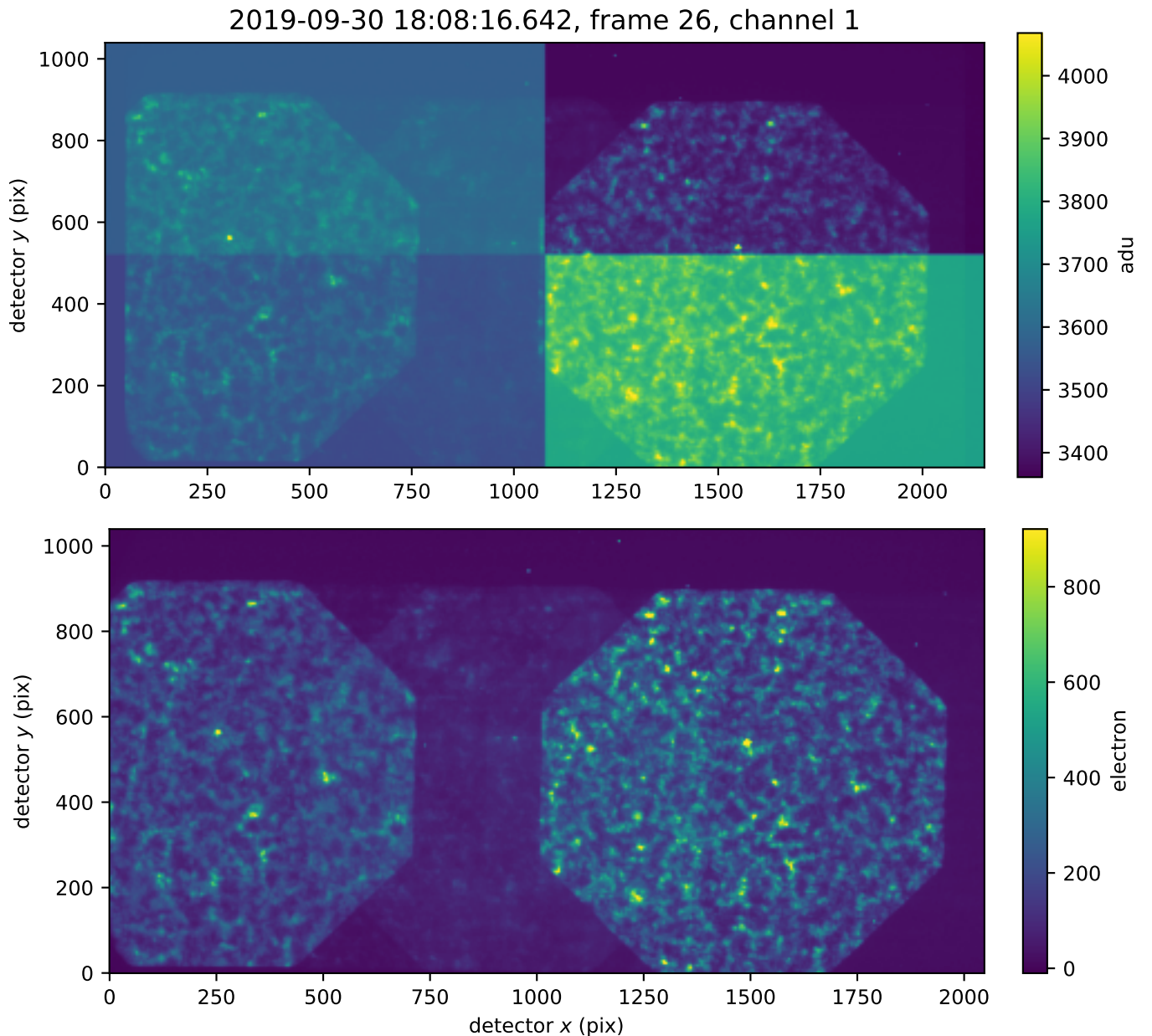


Figure 4.4: The top panel is the raw, Level 0 image captured by Channel 1 of ESIS during apogee. The bottom panel is the same image after Level 1 processing. The Sun viewed through the octagonal field stop in the O V 629.7 Å spectral line is on the right side of the detector, this portion of the detector was cropped to generate Level 3 data. The Sun viewed through the octagonal field stop in the He I 584.3 Å line is partially on the left side of the detector. The Mg X 609.79 Å line is between and partially overlapping both of these two strong lines.

### Level 3 Data

The ESIS Level 3 data product is created to provide a co-aligned, single wavelength image in each channel for quick identification of events with significant line-of-sight velocities and easy comparison with coordinated data that does not require inversion. Level 3 data also allows for single wavelength inversion prior to the completion of the final optical distortion model and the Level 2 data product. A demonstration of both qualitative and quantitative analysis of Level 3 data is given in Section 4.

Level 3 data is generated directly from Level 1 as follows:

1. Level 1 data is converted to units of photons in the target wavelength and then despiked.
2. Optical distortion and internal co-alignment are corrected, and each channel is resampled onto an appropriately cropped common grid, with known alignment to AIA data.
3. Each channel is corrected for vignetting.

Figure 4.5a shows an example of a Level 3 image from Channel 2 taken at 18:08:46. All three steps make the assumption that the intensities are associated with the target wavelength. No attempt is made to distinguish photons of other wavelengths that may overlap with the octagonal field stop image in the target wavelength, so Level 3 is a useful construct for a target wavelength corresponding to a strong spectral line with minimal contamination. The above steps are described in greater detail below.

Conversion to Photons and Despiking In order to use Level 3 data for early inversion the intensity needs to be converted to photons in order to properly account for uncertainty in the data. The conversion from electron to photon is done to Level 1 data prior to co-alignment

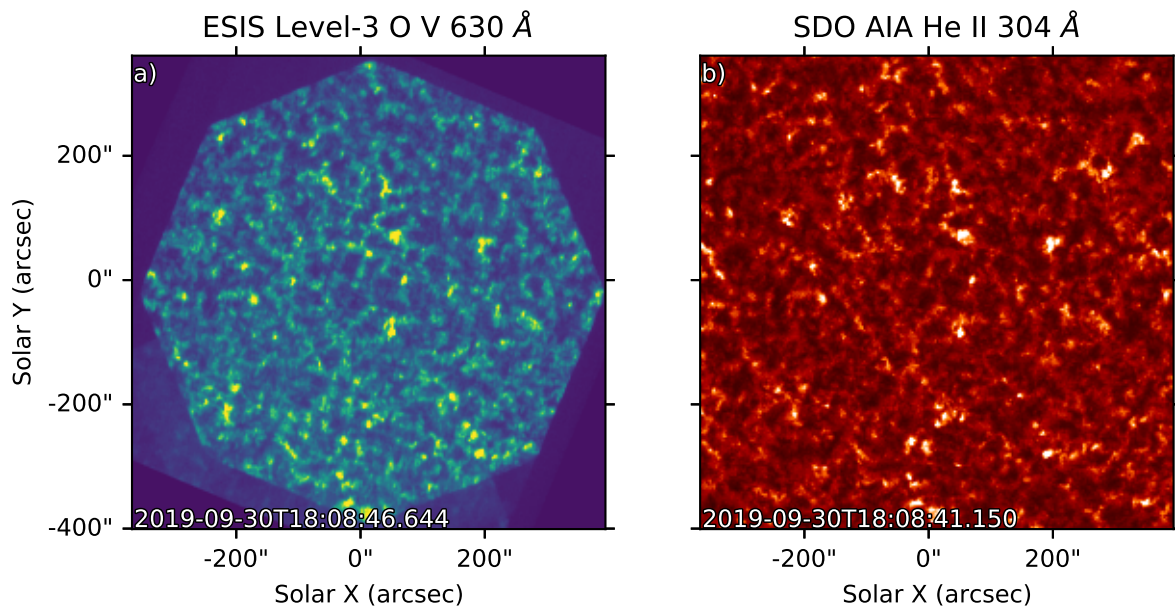


Figure 4.5: (a) An example of the Level 3 data product from Channel 1 taken at 18:08:46. This data has been aligned using nonlinear mapping parameters to the closest co-temporal AIA 304 Å image, shown in (b).

efforts. The intensity in photons,  $I_\gamma$ , then becomes

$$I_\gamma = I_e * 3.6 \frac{\text{eV}}{e} * \frac{\lambda}{hc}, \quad (4.1)$$

where  $I_e$  is the Level 1 intensity in electrons, and  $\lambda$  is the target wavelength. With a Silicon band gap energy of  $3.6 \text{ eV}/e$ , and an energy per O V 629.7 Å photon of 19.6 eV gives 0.18 photons per electron.

Due to geomagnetic activity on launch day, our detectors received a substantial number of charged particle hits. We therefore elected to despike the data. Available despikers were difficult to tune in such a way that they eliminated particle hits, but not small transient events (e.g. explosive events). We therefore developed a new despiking algorithm, which is identified in Appendix A.

Optical Distortion Correction and Channel Co-Alignment The four ESIS channels were spatially co-aligned in two steps. First, each ESIS image is cropped around the O V 629.7 Å spectral line, (roughly pixels 1000 - 2048 of the Level 1 data shown in Figure 4.4) and then co-aligned to the closest AIA 304 Å image in time. The AIA 304 channel was chosen for co-alignment because it is the AIA EUV channel most visually similar to O V, in both the background and bright events (Figure 4.5b). Prior to co-alignment each AIA image was prepped to Level 1.5 using the aiapy routines `aiapy.calibrate.update_pointing()` and `aiapy.calibrate.register()`. The co-alignment was achieved through a linear coordinate transformation of the cropped ESIS image that maximizes the zero lag cross-correlation between it and AIA 304, the results of this are shown in Figure 4.5.

Since ESIS has a slightly non-linear distortion function (Smart et al., 2021), an additional internal alignment step is performed. Sub-pixel accuracy of the ESIS inter-channel alignment is critical to our tomographic inversion of the data to obtain line profiles, so we exercise more care than with the alignment to AIA. Using a single ESIS channel as reference,

in this case Channel 2, each other channel is co-aligned to it via a quadratic coordinate transformation that maximizes the zero-lag cross-correlation. Figure 4.6 shows the ratio of peak cross-correlation after the quadratic internal alignment to that of the linear co-alignment with AIA for every camera pair and every exposure. A ratio greater than 1 implies this second step improved co-alignment. We find that the internal alignment improves not only the co-alignment between each channel and the reference channel (dots in Figure 4.6), but also the co-alignment between every other combination of channels (stars in Figure 4.6). This ratio is greater than 1 in all cases and shows a less than 1 percent improvement in peak correlation, demonstrating the subtle non-linearity of the ESIS optical distortion function. In pixels, this corresponds to an average change in mapping of  $\approx 0.4$  pixels.

After the co-alignment is complete each Level 3 image has been re-binned to AIA resolution, 0.6 arcsecond per pixel, and can be assigned the WCS information (Calabretta & Greisen, 2002) from the nearest image AIA in time, providing pointing information and easier co-alignment with coordinating instruments.

Vignetting Correction Each ESIS channel has a linear trend in intensity across the octagonal field of view along the dispersion direction due to internal vignetting in the optical system caused by having multiple stops in the optical system (Smart et al., 2021). In the co-aligned Level 3 images, where solar north is rotated to the top of the image, the dispersion axes run at different angles relative to solar north in each channel, so the impact of the vignetting field can be seen in the linearly trending background when taking the difference between two channels (Figure 4.7a). We corrected the vignetting by dividing out a linearly trending background, aligned to the dispersion axis, in every image. The parameters of this linear trend in each channel were obtained by minimizing the intensity trend seen in Level 3 difference images.

We define the vignetting field for the  $i$ th channel, at each time index,  $s$ , as a function

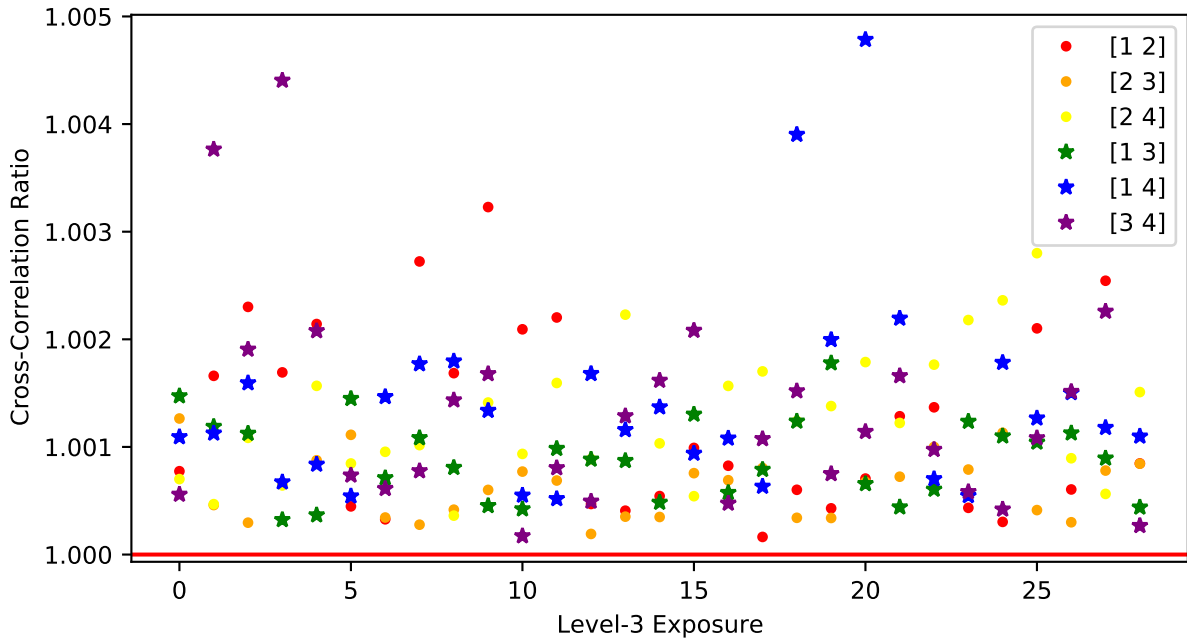


Figure 4.6: For each ESIS exposure (or image sequence) every channel pair, labeled in the legend, is cross-correlated to measure internal alignment quality. The ratio of zero lag cross-correlation after a quadratic transformation to that of a linear transformation is plotted. Every point is above the ratio = 1 line, indicating improved internal alignment for every combination of ESIS channels at each exposure.

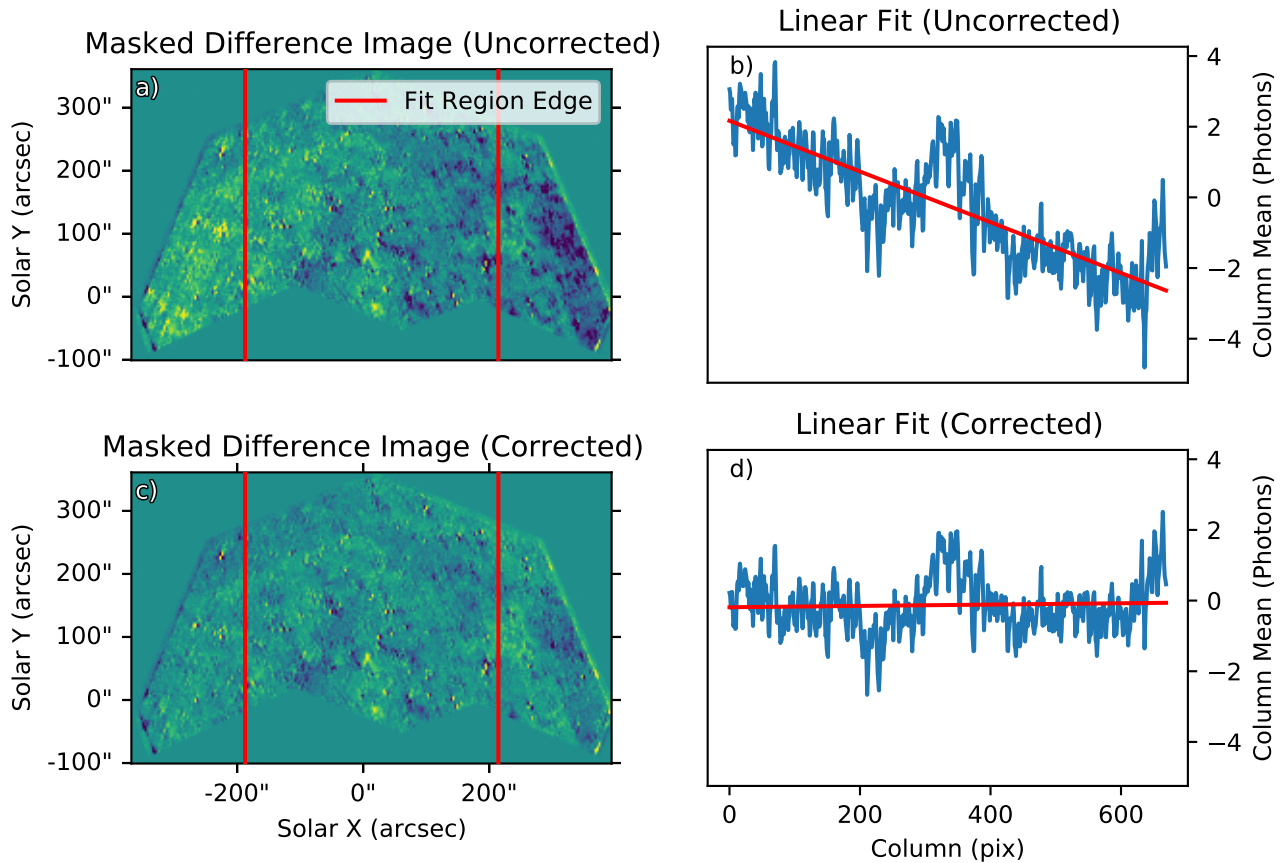


Figure 4.7: Panels a and c show example difference between images with Mg X 609.79 Å masked that are uncorrected and corrected for vignetting respectively. The line fit to the column mean as a function of column (fit between the red bars) shows a difference in background of  $\approx 5$  photons before correction (panel b) at the edges of the field of view, and .4 photons after (panel d).

of the pixels in the Level 3 data,  $(x, y)$ , as

$$V_{is}(x, y) = \frac{m_i}{r_t} * [r(x, y, s) - r_0] + 1, \quad (4.2)$$

where

$$r = x_0 + [\cos(\alpha_i)(x - x_0 - x_{\text{drift}} * s/s_t) - \sin(\alpha_i)(y - y_0 - y_{\text{drift}} * s/s_t)]. \quad (4.3)$$

In Equation 4.2,  $r_0$  is equal to 65 pixels, and represents the distance from the Level 3 image edge to the ESIS field stop octagon edge at  $s = 0$ , the first Level 3 image. The width of the octagon along the dispersion direction,  $r_t$ , is equal to 1140 pixels. In Equation 4.3,  $\alpha_i$  is the angle of rotation of each ESIS Level 3 image relative to a Level 1 image row. In this case,  $\alpha_i = [112.5^\circ, 67.5^\circ, 22.5^\circ, -22.5^\circ]$  for Channels 1-4, respectively. The vignetting field is rotated about the point  $[x_0, y_0] = [635, 635]$ , which is the nominal center of the Level 3 image, to account for the change in dispersion direction. ESIS Level 3 images have a fixed solar coordinate, therefore the the field of view defined by the octagon drifts as a function of time index,  $s$ , due to a slight pointing drift during the flight. The empirical drifts are  $[x_{\text{drift}}, y_{\text{drift}}] = [8, -4]$  pixels. The total number of Level 3 exposures is  $s_t = 29$ .

In the above relations, we have just four free parameters, the slopes  $m_i$ . The four channels of ESIS give 6 possible difference images for fitting the vignetting function for each image sequence  $s$ . When the average slope of all 174 combinations (6 difference images per each of the 29 exposures) is minimized we consider the vignetting corrected.

Measuring the trend from the data is additionally complicated by the overlap of the bright Mg X 609.79 Å line. This line overlaps different regions of the field of view in each channel, see Figure 4.8. Therefore when fitting the background we restrict ourselves to the portion of the field of view without the Mg X 609.79 Å overlap in any channel. We also only use column means between the red bars in Figure 4.7 to ensure sufficient pixel numbers in

each column.

The resulting final fit,  $m_i = [.35, 0.28, 0.34, 0.6]$ , differs from the field predicted using ray tracing and geometric optical models (Smart et al., 2021), which can be attributed to a few likely culprits. Our optical models assume a perfectly built and aligned ESIS instrument, resulting in each channel having identical vignetting. A misalignment of the ESIS field stop center, the ESIS primary optic center, and the center of the ESIS grating array, all shift the geometry of the ESIS central obscuration and can easily modify the vignetting field in each channel. When performing this vignetting correction we found we needed to allow the slope to vary for each channel to achieve a quality fit. Another difference between the fit and the model is the slope of each vignetting field. Our fits to Level 3 data show less vignetting in every channel than is predicted by our optical models. This likely comes from the imprint of adjacent spectral lines, the most obvious being that of Mg X 624.9 Å visible in Figure 4.7c. Since this Mg X line overlaps almost entirely with O V, and has an identical vignetting function, it adds intensity that prevents a perfect fit. It is also possible that there is a subtlety to the ESIS vignetting calculation that we have failed to account for in our ray trace and geometric optical models. Despite the uncertainties in vignetting, which we have found difficult to quantify, Level 3 differences are much flatter in intensity post vignetting correction as is seen in Figure 4.7c, and will therefore lead to a higher fidelity intensity recovery when inverting Level 3 data.

Relative Radiometric Correction The intensity of each channel is normalized by equalizing the image mean over the least contaminated shared piece of Sun, and is therefore performed after inter-channel co-alignment and the vignetting correction. We divide each image by its mean in the region of the field of view uncontaminated by Mg X 609.79 Å in every channel (shape shown in Figure 4.7 a and c) and multiplying it by the mean in that same region from the brightest image in the brightest channel (Channel 2 at apogee) This

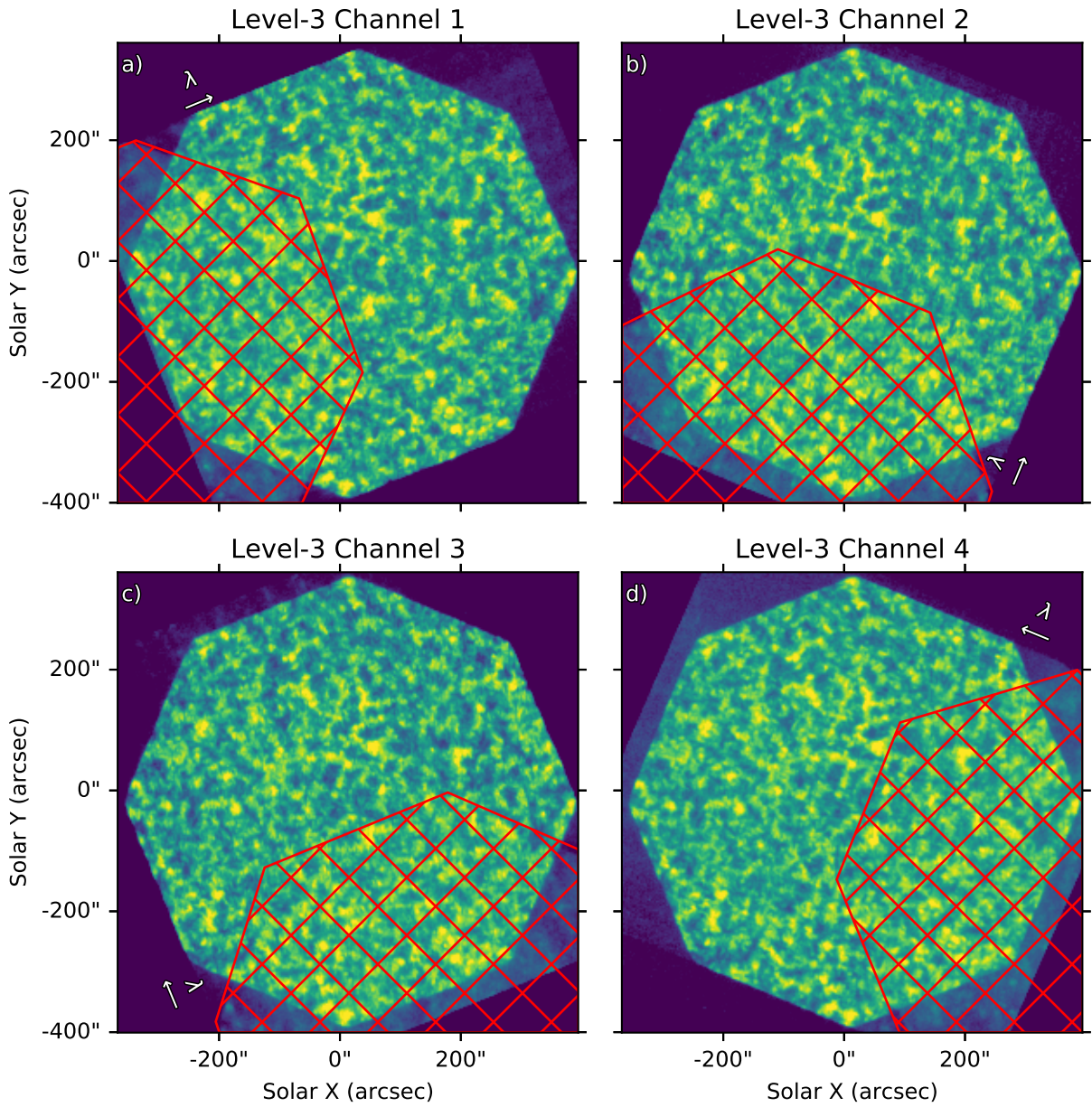


Figure 4.8: The red hashed region shows the overlap of the Mg X 609.79 Å spectral line in each channel that is masked prior to the vignetting correction and intensity normalization. These images are displayed in log scale in an attempt to bring out the subtle contamination. The outline of the Mg X can be seen very clearly in difference images like Figure 4.9.

not only normalizes the intensity between each channel at every exposure, but also corrects for the effects of atmospheric absorption mentioned in earlier sections.

### Preliminary Results

In this section, we provide a preliminary analysis of the ESIS Level 3 data. Our aims are to assess the ability of the ESIS data to (1) provide velocity signatures of dynamic events and (2) aid in developing a useful qualitative and quantitative understanding of the events. Despite the lack of solar activity, ESIS managed to capture tens of small, transient events and one larger event during the  $\approx 5$  minutes of observation in the O v 629.7 Å spectral line. We analyze five example events in this section.

#### Level 3 Difference Images

Early work with MOSES images demonstrated the utility of examining differences between different projections of the spatial-spectral cube (channels) to identify solar features with significant line-of-sight velocity (Fox, 2011; Fox et al., 2010; Rust & Kankelborg, 2019; Rust, 2017), and to diagnose spectral contamination (Rust & Kankelborg, 2019; Rust, 2017). It is for this reason that we developed a Level 3 data product, spatially co-aligned in O v, that would allow us to take differences between ESIS channels. Each ESIS channel disperses solar features in a different direction relative to solar north, determined by the orientation of each grating. The positive dispersion direction in each Level 3 image is indicated by the arrows in Figure 4.8.

Figure 4.9 (and associated animation) shows the difference between Channels 2 and 3 for the full ESIS field of view. Since wavelength is dispersed a different direction in each channel, taking the difference between two simultaneous, spatially aligned channels cancels the intensity in the O v spectral line core. What remains are signatures of Doppler shifts, line broadenings, and other spectral lines. Before we describe signatures of Doppler shift, it may

be helpful to point out certain large-scale features that arise from spectral contamination. The yellow octagon that overlays the lower left quadrant of the image is the Mg x 609.79 Å line that overlaps the O v 629.7 Å line in Channel 2. Similarly, a dark octagon on the lower right quadrant is the portion of the Mg x 609.79 Å line that overlaps the O v 629.7 Å line in Channel 3.

In the difference image, small-scale black and white lobes frequently appear near the locations of bright features on the Sun. A few of such features are marked with red boxes and will be discussed in detail below. The small black lobes tend to lie at an angle of  $-22.5^\circ$  with respect to solar north, which is the direction of dispersion of Channel 3, while white lobes tend to lie at an angle of  $+22.5^\circ$  with solar north, which is the direction of dispersion of Channel 2. A sufficiently compact and well-isolated brightening functions as its own spectrograph slit. The lobes then form V-,  $\Lambda$ -, or X-shaped features. Furthermore, intersection of the lobes occurs at the line center. Lobes above that intersection (i.e., along the dispersion direction in both channels) indicate a red shift (V). Lobes below line center similarly indicate a blue shift ( $\Lambda$ ). The complete X-shape indicates a line broadening in which both red and blue shifts are present.

Although the ESIS geometry differs significantly from MOSES, which had three images taken at spectral orders  $m = -1, 0, 1$  of a single grating, analogous Doppler signatures appeared in MOSES data. These Doppler signatures were analyzed in great detail by Rust & Kankelborg (2019), who sliced through small events along the dispersion direction to measure He II 303.8 Å line profiles from MOSES data.

Three features, labeled a, b, and c in figure 4.9, serve to illustrate the  $\Lambda$ , V, and X morphologies described above. Figure 4.10 shows the difference image in the first column for all three events, then the Channels 2 and 3 data in the subsequent columns. Figure 4.10a shows a  $\Lambda$ -shaped event with lobes pointed downward in the difference between the Channel 2 and Channel 3 Level 3 image. Since we know that the direction of positive wavelength

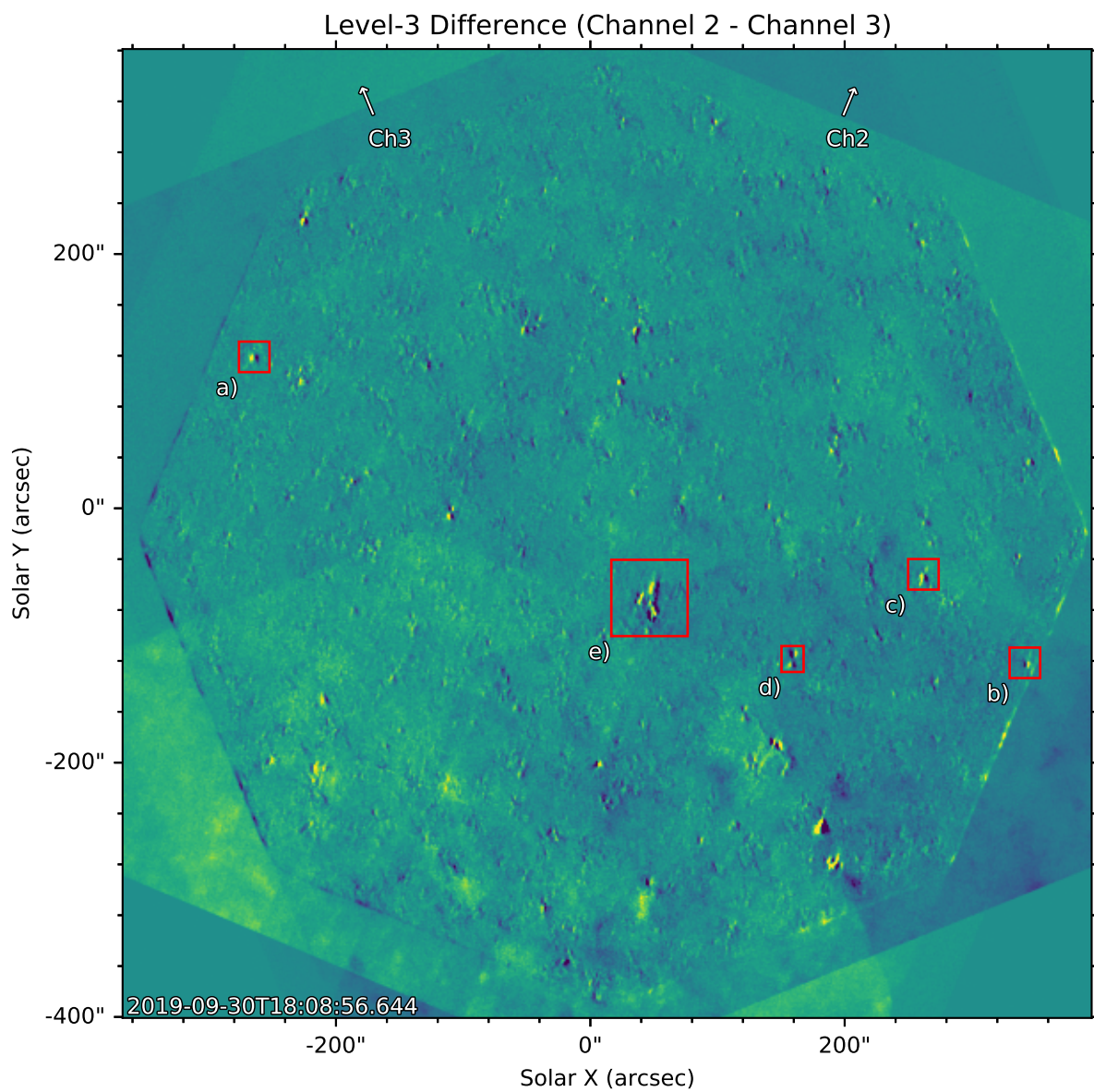


Figure 4.9: Full FOV Difference between Channel 2 and Channel 3 Level 3 images. Arrows denote the positive dispersion direction in Channel 2 and 3. Events a-c are highlighted in Figure 4.10. Inverted results for Events c and d are shown in Section 4. A time series of Event e is shown in Figure 4.11. The associated animation shows these difference images throughout the ESIS observation.

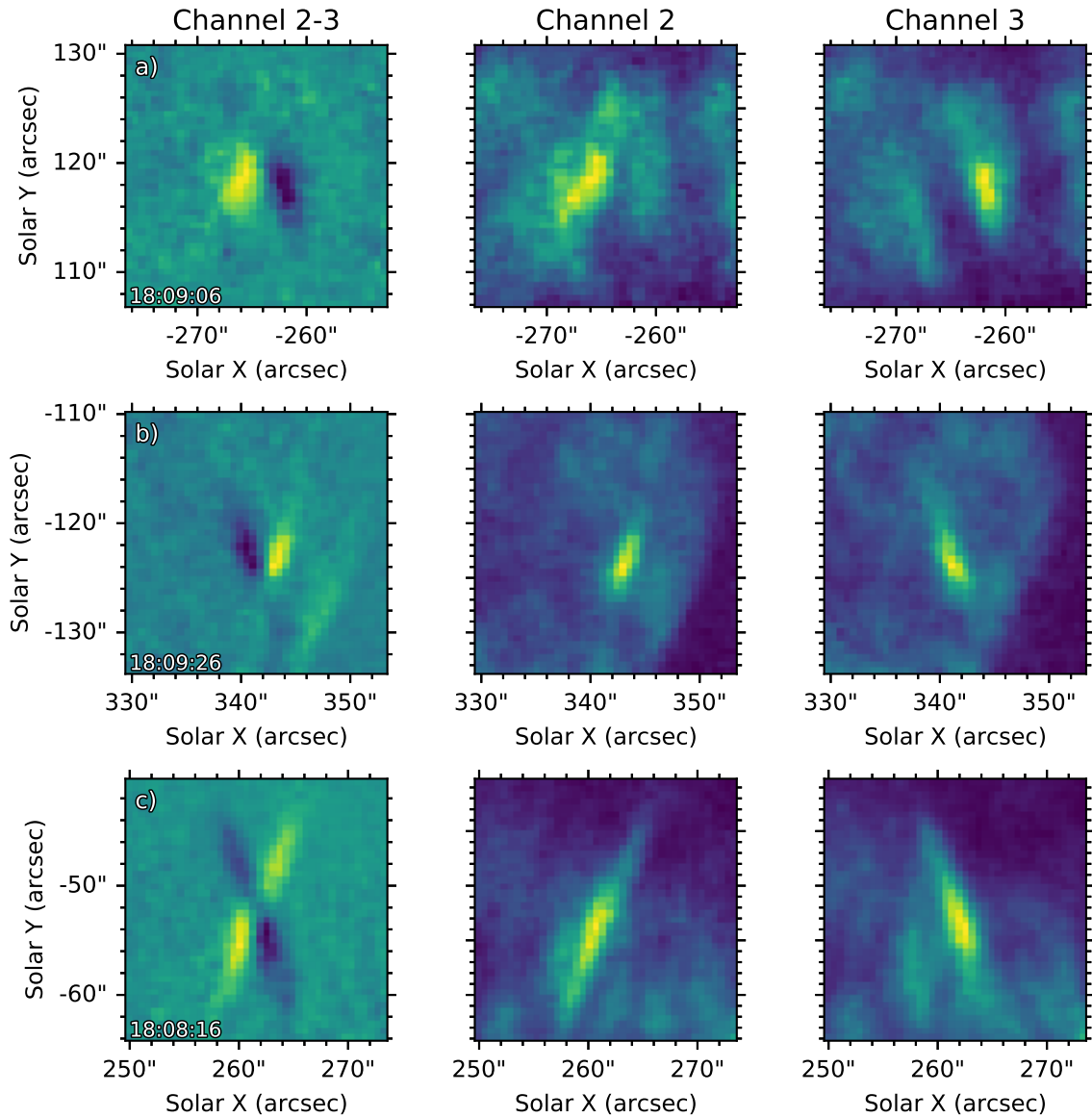


Figure 4.10: Events a, b and c identified in Figure 4.9 are examples of a mostly blue, red, and broadened even, respectively. The difference between Channels 2 and 3 is shown in the left hand column, while the Channel 2 and Channel 3 intensities are shown in the middle and right columns. The velocity signature is most easily seen in the difference image, while the straight intensities provide information on the line core intensities.

dispersion is up and to the right in Channel 2 and up and to the left in Channel 3 (Figure 4.8) we immediately know that this event is predominantly blue shifted. Similarly, an upward facing V-shaped event, like the one shown in Figure 4.10b, is predominantly red shifted. X-shaped events, shown in Figure 4.10c, suggest enhanced emission in both the red and blue wing of the line profile. Difference images can provide immediate qualitative understanding of these simple, point-like events. During the 5 minute rocket flight, tens of similar events were detected in the ESIS field of view. We observe that the X-shaped events are especially common in this dataset, though multiple examples of each type are apparent.

During the ESIS flight, we also captured a handful of spatially extended Doppler signatures that are more difficult to interpret. The most obvious of these is an eruption near disk center, Event e in Figure 4.9. This large event is shown at three times in Figure 4.11. The entanglement of spatial and spectral information in this relatively complex event makes it difficult to derive a qualitative interpretation from the difference images (left column of the figure). A cluster of overlapping positive and negative lobes in the brightest portion of the event (location e1) sometimes present as a  $\Lambda$ , V, or X shape, but not always, and evolve significantly in time. The top row shows this event early in its evolution. Intensity is concentrated to a small region and presents as two jets, one red and one blue, with the red shifted source slightly to the right of the blue shifted source. 100 seconds later (middle row), the event is dominated by a significant red shift (upward facing V) at the location of initial brightening. There is also an imprint of fainter differences above the brightest knot of intensity (location e2) showing motion along a spatially extended structure. The difference lobes in this faint structure are opposite in polarity to the intensity below, and therefore appear to represent blue shifted material ejected from the site of initial brightening. This is supported by the appearance of a thin string of ejected material at the same location in AIA 304  $\text{\AA}$ , 171  $\text{\AA}$ , and 193  $\text{\AA}$  (Figure 4.12 and the animation associated with Figure 4.11). By the end of the event (another 70 seconds later, bottom row) the dominant red shift subsides,

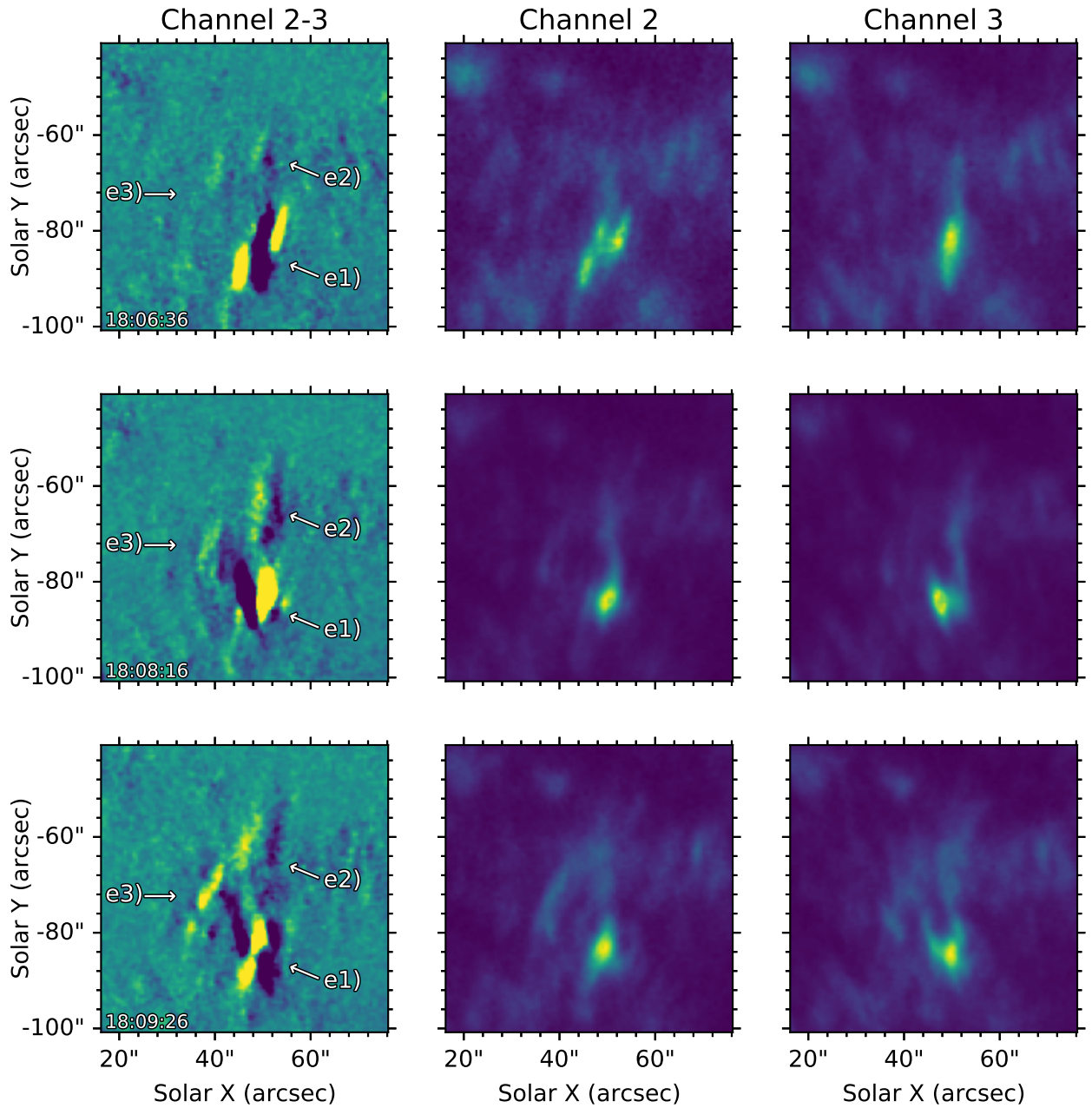


Figure 4.11: The largest and most complex velocity event (e) captured by ESIS shown at three different times (complete evolution in animation). The event starts as two jets (one red, one blue) with slight spatial separation, evolves into a strong red shift where the event begins paired with faint blue shifted material above, and ends in a complicated combination of velocity not easily interpreted from difference images. Co-temporal images from AIA 304 Å, 171 Å, and 193 Å are included in the animation for additional context.

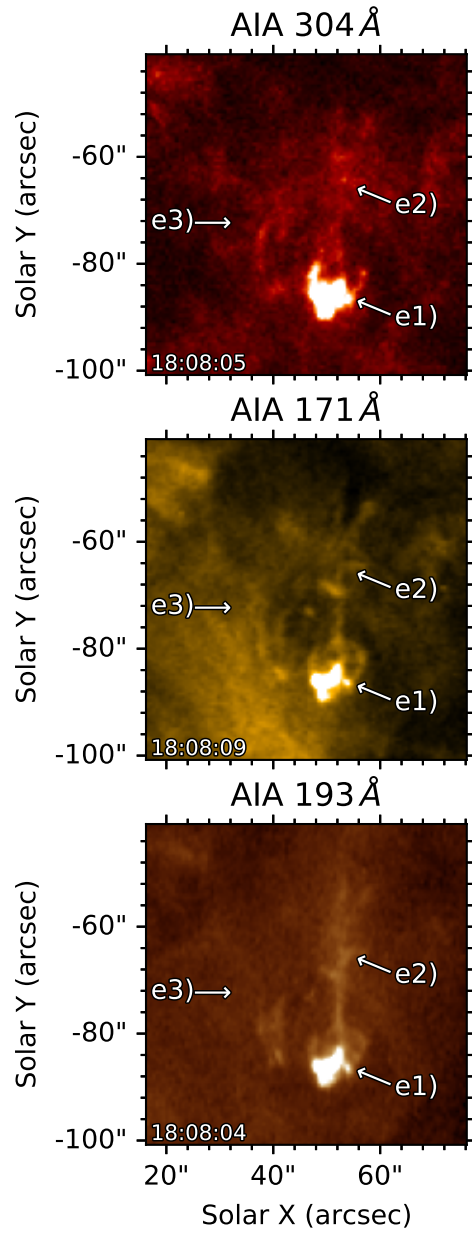


Figure 4.12: Co-aligned AIA 304 Å, 171 Å, and 193 Å images of event e (highlighted in Figure 4.11) are shown with identical locations labeled. The location of peak intensity (e1) in the ESIS Level 3 data is also the location of brightest intensity in these EUV channels. We also note a jet like structure which is very diffuse in the cooler 304 Å images, and visible as a thin line of intensity in 171 Å and 193 Å between the e1 and e2 labels that matches the location of the faint blue shifted structure visible in Level 3 difference images. Animations of these AIA channels, included with Figure 4.11, show material traveling along this line and being ejected away from location e1.

leaving a complicated spectral signature at the brightest portion of the event, and in the adjacent region up and to the left (location e3).

So far, we have been exploiting two of the four ESIS channels with our difference image. This approach is qualitative, and its limitations become apparent with complex and spatially extended dynamics as we saw in event e. An understanding of ESIS difference images provides a starting point, and offers a sanity check when interpreting numerical inversions that take advantage of all four projections. In the following section we will focus on inverting two smaller events (c and d), and will save a more in depth analysis of Event e for a future publication.

### Early Inversions

In order to better disentangle the spectral and spatial information captured by ESIS, and to provide quantitative velocity information, all four channels must be combined and “inverted” to return a single, spatial-spectral cube,  $I(x, y, \lambda)$ , at every exposure. For our preliminary inversions of the O v 629.7 Å ESIS Level 3 data we used a Multiplicative Algebraic Reconstruction Technique (MART). MART is attractive for our first inversions because it is fast, requires no training or explicit assumptions about the data, and automatically enforces image positivity. We describe our MART implementation in Appendix B.

When constructing the ESIS Level 3 data, each channel is co-aligned to a reference channel (Section 4). By doing this, we are assuming that the mean velocity in O v 629.7 Å is zero prior to inverting. Work by Peter & Judge (1999) suggests that the transition from a mean red shift to a mean blue shift at disk center occurs around .5 MK. Therefore, since O v 629.7 Å is a relatively hot transition region line, and is formed near .22 MK, we expect a systematic error in our inverted velocities of less than  $10 \text{ km s}^{-1}$  as a result of this assumption.

In Figures 4.13 and 4.14, and their associated animations, we present the MART

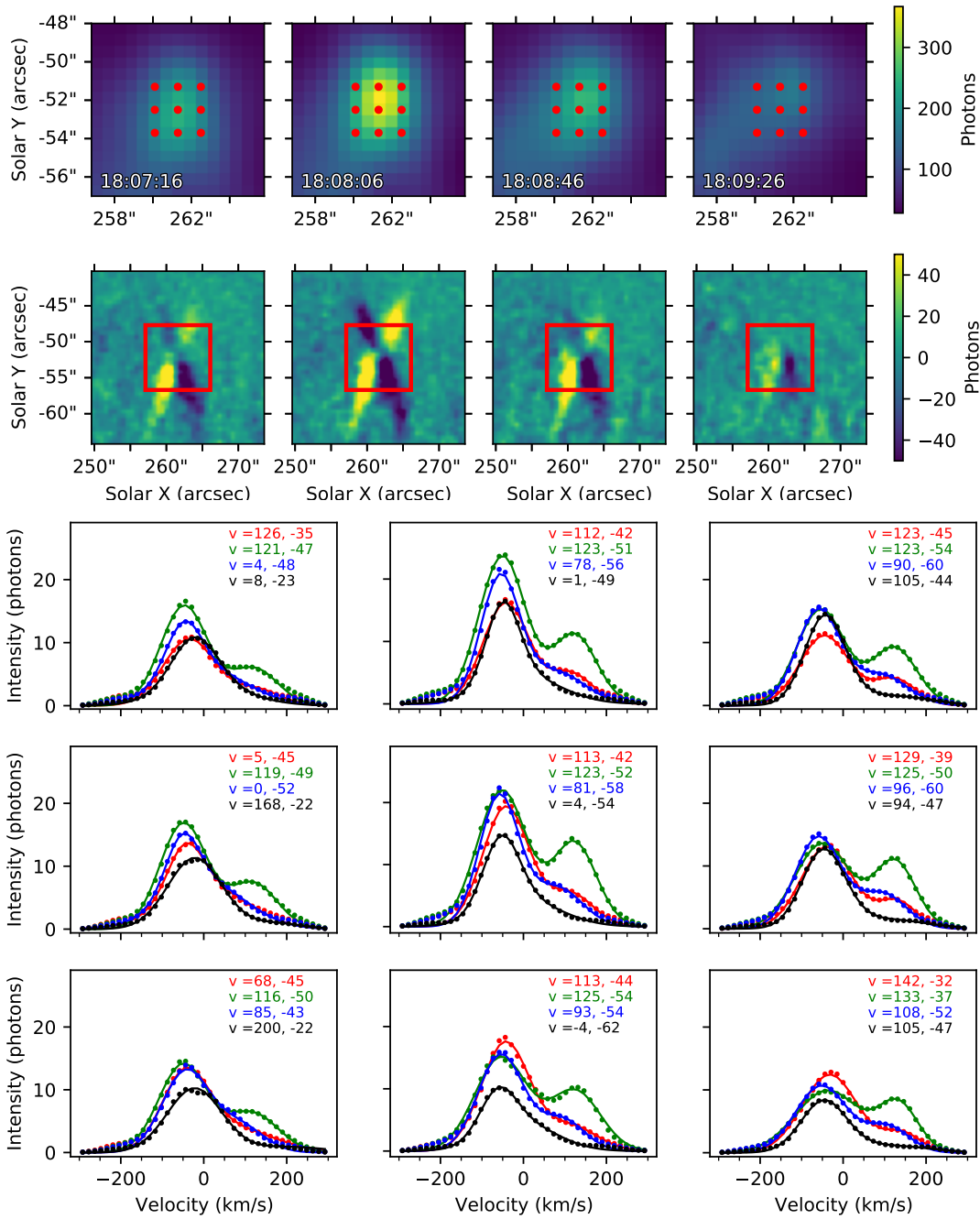


Figure 4.13: MART inverted results for event c in Figure 4.9. The integrated intensity (top row) and corresponding Level 3 difference image (second row) are shown at 4 different times. The red box marks the FOV used in the top row. The O V 629.7 Å line profile at each position marked with a red dot is plotted in the matching 3x3 grid in a different color for each time (in order red, green, blue, black). Each MART line profile (dots) is overplotted with a double gaussian fit (solid line). Bulk shifts in km/s for each component of the fit are provided in the legend for each time in their respective color.

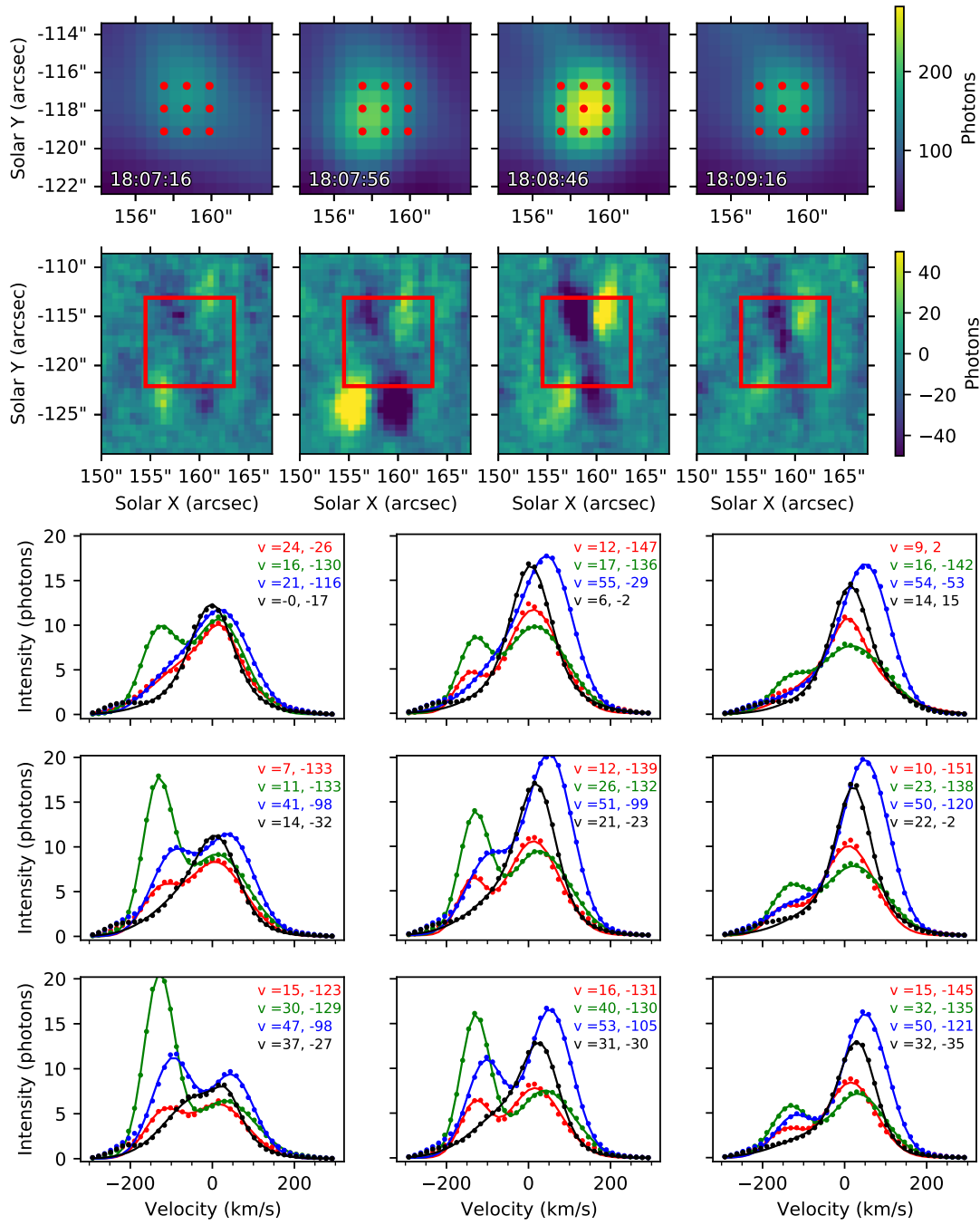


Figure 4.14: MART inverted results for event d in Figure 4.9 presented in the same fashion as Figure 4.13.

inversion for two different compact transient events, labeled c and d in Figure 4.9. Both events have an X-shaped presentation, begin and end within the ESIS observing time, and show noticeable temporal evolution in velocity. Each figure shows the total O v 629.7 Å integrated intensity, obtained by summing the MART inversion along the wavelength dimension, in the top row at four different times. The second row shows uninverted Channel 2-3 Level 3 difference images at those same times for comparison. The FOV of the intensity image from the top row is shown as a red box on the difference image. Inverted O v 629.7 Å line profiles are plotted in a  $3 \times 3$  grid, corresponding to the grid of 9 positions marked in red on the intensity images. The red, green, blue, and black curves correspond to the four times indicated in the top row. We performed a double Gaussian fit for each line profile in order to more easily pick out the location of each peak in velocity. The results of the fit (solid line) is plotted over the MART inverted data (dots). The deviation from line center of each Gaussian is recorded in  $\text{km s}^{-1}$  in the color matching the line profile. In the animation, we plot the red and blue components of each fit separately as dashed lines, their sum as a solid line in fuschia, and the MART inverted line profile in green dots.

Event c, shown in Figure 4.13, lasts just over 4 minutes and shows significant temporal evolution in the line profile. Throughout the event the blue component of the O v 629.7 Å line dominates and is centered at  $\approx -50 \text{ km s}^{-1}$ . This blue component persists for the entire duration of the event with relatively gradual changes in intensity and velocity. The red component of the event is bursty in nature, with two small peaks in intensity at 18:07:36 and 18:08:16, and is centered at  $\approx 120 \text{ km s}^{-1}$ . The red and blue components of the line are only occasionally well separated, but the two Gaussian fit consistently follows the inverted line profiles with only small deviations. This explosive event is  $\approx 3$  arcseconds in diameter and shows little spatial variation in the line profile across the event.

The explosive event highlighted in Figure 4.14, event d, is similar to event c in that it has enhancements in both the red and blue wing of the line profile, but is more complicated

in its presentation. Event d begins around 18:07:16 and its intensity has almost completely died away by the last Level 3 image. At the beginning of the event a slightly redshifted component dominates the line profile. A strong blue component in the line profile centered near  $-130 \text{ km s}^{-1}$  begins to appear 18:07:16 and peaks at 18:08:06. This blue component is brightest in the lower left portion of the event. The red component of the line profile peaks at 18:08:56 and is centered near  $50 \text{ km s}^{-1}$ . Unlike event c, the blue component of the line is less persistent in time. Also, the blue and red components of the event do not occur in the same spatial location. This is visible both in the grid of line profiles and the difference images. Intensity in the line profiles show the blue component peaking in the lower left, while the red component peaks in the middle to right columns. In the difference images, this corresponds to a clear vertical and horizontal separation between the blue  $\Lambda$  and the red V. A closer look at the inverted data shows an  $\approx 1.35$  arcsecond spatial separation between centroids of the blue and red component.

There are two free parameters in our MART algorithm, namely the exponent used in the contrast enhancement filter and the number of times it is applied (Appendix B steps 2 and 3). The inversions in this section were tried with a wide range of these parameters. The Appendix shows the results of tweaking these free parameters for a single timestamp of Event C. We find that the results are robust to variation in both parameters. In particular, we consistently find line profiles consistent with a qualitative interpretation of the difference image movies, and measure bulk flows within  $\approx \pm 15 \text{ km s}^{-1}$  ( $\approx \pm 1$  pixel) for a given exposure.

#### Discussion/Conclusions and Future Work

The ESIS sounding rocket mission, launched September 30, 2019, was successful in capturing spatial and spectral information over its entire  $11.5'$  field of view in multiple wavelengths (He I 584.3 Å, Mg X 609.79 Å, and O V 629.7 Å) at every exposure. ESIS is

a unique instrument. It is not only a slitless imaging spectrograph, of which there only a handful of examples, it is also a Computed Tomography Imaging Spectrograph (CTIS). To our knowledge, the ESIS and MOSES sounding rocket instruments are the only CTIS instruments ever flown in space to observe the Sun.

We have processed the ESIS data into multiple levels such that preliminary scientific work can be done, including a Level 3 data product (Section 4) that allows for taking spatial differences between channels, and early inversion. Level 3 difference images in the O V 629.7 Å wavelength (Section 4) reveal a host of small transient brightenings across the field of view with significant line-of-sight Doppler velocity, some in excess of  $\pm 100 \text{ km s}^{-1}$ . They also reveal several larger and more complex events with large velocities, most notably the eruption identified near disk center (event e in Figure 4.9).

During the roughly 5 minutes of ESIS observing time it captured tens of events with supersonic velocities, evolving on 10 s timescales, over its 11.5' field of view. Even seemingly simple explosive events evolve fast enough in time, and have significant spatial distributions of intensity and velocity, such that rastering a traditional slit spectrograph would fail to capture the event completely. This, combined with the fact that ESIS can measure many events like this simultaneously, makes it a powerful tool for capturing and diagnosing dynamic events in the solar atmosphere.

We use a Multiplicative Algebraic Reconstruction Technique (MART, Appendix B) to disentangle the combined spatial and spectral information in the four ESIS Level 3 images to find a single spatial-spectral cube  $(x, y, \lambda)$ , covering just the O V 629.7 Å line, for two small transient brightenings (Section 4). Our inversions reveal strong red and blue jets with bulk flows in excess of  $100 \text{ km s}^{-1}$  that evolve on the timescale of the ESIS cadence, 10 seconds. These two events are spatially compact, a few arcseconds, and have lifetimes of a few minutes. Despite their compact nature, the red and blue components measured are separate and distinct in both space and time. This is especially noticeable in event d (Figure

4.9 and 4.14) where the centroids of the blue and red jet are displaced by a little over an arcsecond.

The bimodal nature of these small brightenings is similar to observations made by Rust & Kankelborg (2019) He II 303.8 Å using MOSES data, particularly in the case of event d where the separation is visible in the Level 3 data prior to inversion. This presentation is different than typical explosive event line profiles typically observed by IRIS in Si IV 1394 Å, where small transient events often show smaller bulk flows, dominant line core emission, non-thermal broadening (Chitta et al., 2017; Innes et al., 2015). The bimodal profile and bulk flows exceeding the sound speed ( $\approx 78 \text{ km s}^{-1}$  for O V at 225000K) suggest magnetic reconnection occurring in a small region with little to no stationary emitting plasma, most reminiscent of a Petschek type reconnection (Innes & Tóth, 1999). Though we hypothesize that both jets originate at a single reconnection site, we admit that it is puzzling that observed fluctuations of the red and blue jets are not temporally correlated, most notably in explosive event d (Figure 4.14). It is also puzzling that in both events c and d there is a lack of symmetry in velocity between the red and blue jets. It may be that the reconnection in these small events is more complex than we imagine and needs to be treated in 3-D; however, it is also possible that, looking in a single spectral line, we are not seeing all of the ejected plasma. Further work with the ESIS data may help to clarify this issue. Several of these events were captured in He I 584.3 Å, Mg X 609.79 Å, and O V 629.7 Å simultaneously, putting ESIS in a position to measure the outflows at multiple temperatures. If the event is present in hotter or cooler lines we can also see if the bi-modal nature of these line profiles is unique to O V 629.7 Å or persists at lower and higher temperatures. Also, IRIS was running small four step coarse rasters near disk center during the hour long ESIS launch window. Although none of the events analyzed in this paper were captured by IRIS, a closer look at the IRIS data may reveal small explosive events suitable for direct comparison with ESIS line profiles.

The largest event captured by ESIS (Figure 4.11 and Figure 4.12) most notably shows a strong red shift at the brightest part of the event (location e1) and a faint string of blue shifted material (location e2) rising above. The faint blue shift, combined with the appearance of rising material in the cooler AIA channels, gives the appearance of a small jet or possible mini-filament eruption. The brightest part of the event being red shifted also matches the idea that “jet bright points”, a common feature of smaller jets found at the base of the erupting structure, are the result of a small post-reconnection arcade (see Sterling et al., 2015, and references therein). The ability of ESIS to capture velocity information across this dynamic event at a 10 second cadence gives us a great advantage when trying understand the underlying physics, and is an exciting opportunity for future study and collaboration. Future work on this event will focus on comparing multiple inversion methods, and examining multiple spectral lines in the ESIS passband, to ensure we have the clearest possible picture of the velocity distribution before drawing conclusions.

The next major tasks in the analysis of ESIS data will be to invert the entire spatial-spectral cube, from He II 584 Å to O V 630 Å. A self-consistent inversion will be required to separate out the dimmer Mg X 624.9 Å, and perhaps even the faint O III 599.6 Å line. This will require a careful characterization of the wavelength-dependent distortion in the images, which is currently underway. Future multi-wavelength inversions of the ESIS data will allow for more accurate estimates of the frequency and distribution of explosive events across a large portion of the solar disk and at different heights in the solar atmosphere than have been possible with slit spectrographs. It will also allow us to track energy and material moving through multiple layers of the solar atmosphere to form a clearer picture of where and how these reconnection events unfold.

### Acknowledgments

This work was supported primarily by NASA Grant NNX14AK71G. Roy Smart acknowledges NASA NESSF program grant 80NSSC17K0524. The success of ESIS owes much to the technical skill of personnel at NASA Marshall Space Flight Center, particularly Ken Kobayashi, Brent and Dyana Beabout, Harlan Haight, and James Duffy. We would also like to acknowledge the NASA SRPO and NSROC employees involved, all of whom went above and beyond to support ESIS from start to finish, we couldn't have done it without you. CHIANTI is a collaborative project involving George Mason University, the University of Michigan (USA), University of Cambridge (UK) and NASA Goddard Space Flight Center (USA). This research used version 0.5.0 (10.5281/zenodo.4676478) of the aiapy open source software package (Barnes et al., 2020).

## FINAL CONCLUSIONS

The crowning achievement of my graduate work is the success of the ESIS sounding rocket mission, which I most certainly did not accomplish alone. ESIS succeeded in measuring plasma velocities, in multiple temperature regimes of the solar atmosphere, over a large field of view, every 10 seconds during its 5 minutes of observing time. Even on an exceptionally quiet day on the sun, we captured tens of small solar eruptions and found their velocities to have interesting spatial distribution and temporal evolution at 10 seconds timescales. This demonstrates that the simplifying assumptions we often make when analyzing solar data to account for missing information need to be continuously challenged. It also supports the utility and importance of CTIS instruments for solar study, and the need to build better methods to process the sometimes ambiguous and difficult to analyze data.

The April 18 flare analyzed in the first chapter has been interpreted differently by other scientists and is a great example of when a CTIS observation would have been useful. If it is indeed a tearing mode propagating along a current sheet that created the observed wave in the flare ribbon, then the oscillations in space and velocity should repeat along the ribbon, as is assumed in our model. Fortunately the high resolution slit jaw imager on IRIS allowed us to see the oscillation in space. Unfortunately, because IRIS is a slit spectrograph and was operating in sit and stare mode, we only have velocity information at one position. Assuming extreme luck and perfect pointing of IRIS during the flare it would have been possible to raster over the ribbon and measure the velocity at multiple positions, however the flare ribbon evolved much too quickly in time and we still would have been left with an incomplete picture of the velocity distribution. While the velocity information would have been difficult to retrieve from an ESIS style observation of this event, at least the increased field of view and spectral information in every pixel make it possible to gain a more complete picture of the ribbons evolution.

The first flight of MOSES was also successful at capturing velocity information over its entire field of view in a single wavelength. Data from that flight demonstrated that CTIS data could be inverted to return velocity information from spatially extended eruptions (Fox et al., 2010). It also inspired several design changes implemented in ESIS (Smart et al., 2021) that led to higher quality and more easily interpretable data. Differing point spread functions in each channel of MOSES negatively effected the velocity resolution and made interpreting small explosive events difficult (Fox et al., 2010; Rust & Kankelborg, 2019). This inspired dedicated and independently focusable gratings in channels with more similar point spread functions, making it much easier to compare channels, even visually, at small scales. The detection of significant unexpected spectral content in the MOSES images led to the addition of a field stop in ESIS, clearly defining the field of view to be the same in every wavelength. With out the field stop, it would have been incredibly difficult to differentiate intensity from O V 629.7 Å, Mg X 609.79 Å, and He I 584.3 Å without a complete inversion of the data. Since information from each wavelength only partially overlaps we can already tell we captured certain events in multiple wavelengths, demonstrating the incredible amount of information gathered by ESIS every ten seconds.

A very exciting study yet to be done with the ESIS data is to invert the spatially extended jet (possible minifilament eruption) in each of the bright wavelengths so that we can track the plasma through the transition regions and get a three dimensional picture of the velocity distribution. We know already that the velocity distribution of the jet is evolving on ten seconds timescales from examining the O V 629.7 Å difference movies. Therefore ESIS managed to capture this jet in a way that no currently operating solar instrument, or even combination of instruments, could have, giving us a truly one of a kind picture of the jet. Successful implementation of this study will show the full potential of ESIS and will hopefully help inform and clarify current theories and models of jet formation and evolution.

Though the first launch of ESIS was incredibly successful, we can only learn so much

about the sun from 5 minutes of data. The sounding rocket flights of MOSES and ESIS have allowed us to improve our instrumentation and analysis techniques, but have yet to significantly improve our understanding of the sun. There has been increased interest and popularity of this style of instrument recently, with the proposals of the MUSE(?) and COSIE(Winebarger et al., 2019) satellites, the flight of the MaGIXS(Athiray et al., 2019) sounding rocket with a slot, and the use of EIS slot data for scientific studies(Harra et al., 2020, 2017). This gives me hope that the community is almost convinced that we are capable of understanding, and are seeing the potential in, overlapogram style data, as well as more openly acknowledging the shortcomings of current observing methods. I hope to continue to contribute to the field of solar physics by working on CTIS style instruments and their data, so that we can get this technology on a larger platform. That way we can truly unlock the next level of solar studies and improve our understanding of this giant ball of gas that affects us on earth every second, of every day.

REFERENCES CITED

- Aschwanden, M. J., Nightingale, R. W., Tarbell, T. D., & Wolfson, C. J. 2000, ApJ, 535, 1027
- Athiray, P. S., et al. 2019, ApJ, 884, 24
- Aulanier, G., Pariat, E., Démoulin, P., & DeVore, C. R. 2006, Sol. Phys., 238, 347
- Barnes, W. T., et al. 2020, Journal of Open Source Software, 5, 2801
- Biskamp, D. 1986, Physics of Fluids, 29, 1520
- Brannon, S. R., Longcope, D. W., & Qiu, J. 2015, ApJ, 810, 4
- Brosius, J. W., & Daw, A. N. 2015, ApJ, 810, 45
- Brosius, J. W., Daw, A. N., & Inglis, A. R. 2016, ApJ, 830, 101
- Calabretta, M. R., & Greisen, E. W. 2002, A&A, 395, 1077
- Carmichael, H. 1964, in AAS-NASA Symposium on the Physics of Solar Flares, ed. W. N. Hess (Washington, DC: NASA), 451
- Chamberlin, P. C., Woods, T. N., Eparvier, F. G., & Jones, A. R. 2009, in Society of Photo-Optical Instrumentation Engineers (SPIE) Conference Series, Vol. 7438, Solar Physics and Space Weather Instrumentation III, ed. S. Fineschi & J. A. Fennelly, 743802
- Chandrasekhar, S. 1961, Hydrodynamic and Hydromagnetic Stability (New York: Dover)
- Chen, Q., Otto, A., & Lee, L. C. 1997, J. Geophys. Res., 102, 151
- Chitta, L. P., Peter, H., Young, P. R., & Huang, Y. M. 2017, A&A, 605, A49
- Courrier, H. T., & Kankelborg, C. C. 2018, Journal of Astronomical Telescopes, Instruments, and Systems, 4, 018001
- Culhane, J. L., et al. 2007, Sol. Phys., 243, 19
- Cushman, G. W., & Rense, W. A. 1978, Sol. Phys., 58, 299
- De Pontieu, B., et al. 2021, Sol. Phys., 296, 84
- De Pontieu, B., et al. 2014, Sol. Phys., 289, 2733
- DeForest, C., Elmore, D. F., Bradford, M. P., Elrod, J., & Gilliam, D. L. 2004, ApJ, 616, 600
- Del Zanna, G., & Young, P. R. 2020, Atoms, 8, 46
- Delaboudinière, J. P., et al. 1995, Sol. Phys., 162, 291

- Dere, K. P., Bartoe, J. . F., Brueckner, G. E., Ewing, J., & Lund, P. 1991, *J. Geophys. Res.*, 96, 9399
- Dere, K. P., Bartoe, J. D. F., & Brueckner, G. E. 1989, *Sol. Phys.*, 123, 41
- Dere, K. P., Landi, E., Mason, H. E., Monsignori Fossi, B. C., & Young, P. R. 1997, *A&AS*, 125, 149
- Descour, M., & Dereniak, E. 1995, *Appl. Opt.*, 34, 4817
- Doss, C. E., Komar, C. M., Cassak, P. A., Wilder, F. D., Eriksson, S., & Drake, J. F. 2015, *Journal of Geophysical Research (Space Physics)*, 120, 7748
- Einaudi, G., & Rubini, F. 1986, *Physics of Fluids*, 29, 2563
- Feldman, U. 1992, *Phys. Scr.*, 46, 202
- Fisher, G. H., Canfield, R. C., & McClymont, A. N. 1985, *ApJ*, 289, 414
- Fletcher, L., Pollock, J. A., & Potts, H. E. 2004, *Sol. Phys.*, 222, 279
- Forbes, T. G., & Priest, E. R. 1984, in *Solar Terrestrial Physics: Present and Future*, ed. D. Butler & K. Papadopoulos (NASA), 35
- Foullon, C., Verwichte, E., Nakariakov, V. M., Nykyri, K., & Farrugia, C. J. 2011, *ApJ*, 729, L8
- Foullon, C., Verwichte, E., Nykyri, K., Aschwanden, M. J., & Hannah, I. G. 2013, *ApJ*, 767, 170
- Fox, J. L. 2011, Ph.D. thesis, Montana State University
- Fox, J. L., Kankelborg, C. C., & Thomas, R. J. 2010, *ApJ*, 719, 1132
- Furth, H. P., Killeen, J., & Rosenbluth, M. N. 1963a, *Physics of Fluids*, 6, 459
- Furth, H. P., Killeen, J., & Rosenbluth, M. N. 1963b, *Physics of Fluids*, 6, 459
- Golding, T. P., Leenaarts, J., & Carlsson, M. 2017, *A&A*, 597, A102
- Golub, L., et al. 2020, *Journal of Space Weather and Space Climate*, 10, 37
- Gontikakis, C., & Winebarger, A. R. 2012, in *10th Hellenic Astronomical Conference*, ed. I. Papadakis & A. Anastasiadis, 11
- Handy, B. N., et al. 1999, *Sol. Phys.*, 187, 229
- Harra, L., et al. 2020, *Sol. Phys.*, 295, 34

- Harra, L. K., Hara, H., Doschek, G. A., Matthews, S., Warren, H., Culhane, J. L., & Woods, M. M. 2017, ApJ, 842, 58
- Harris, E. G. 1962, Il Nuovo Cimento, 23, 115
- Hirayama, T. 1974, Sol. Phys., 34, 323
- Innes, D. E., Brekke, P., Germerott, D., & Wilhelm, K. 1997, Sol. Phys., 175, 341
- Innes, D. E., Guo, L. J., Huang, Y. M., & Bhattacharjee, A. 2015, ApJ, 813, 86
- Innes, D. E., & Tóth, G. 1999, Sol. Phys., 185, 127
- Isobe, H., Takasaki, H., & Shibata, K. 2005, ApJ, 632, 1184
- Janvier, M., Aulanier, G., Bommier, V., Schmieder, B., Démoulin, P., & Pariat, E. 2014, ApJ, 788, 60
- Judge, P. G. 2020, The Sun: A Very Short Introduction
- Kak, A., & Slaney, M. 2001, Principles of Computerized Tomographic Imaging, Classics in Applied Mathematics (Society for Industrial and Applied Mathematics)
- Kankelborg, C. C., & Thomas, R. J. 2001, in Society of Photo-Optical Instrumentation Engineers (SPIE) Conference Series, Vol. 4498, UV/EUV and Visible Space Instrumentation for Astronomy and Solar Physics, ed. O. H. Siegmund, S. Fineschi, & M. A. Gummin, 16
- Keenan, F. P., Aggarwal, K. M., Berrington, K. A., & Widing, K. G. 1988, ApJ, 327, 473
- Keenan, F. P., Aggarwal, K. M., Bloomfield, D. S., Msezane, A. Z., & Widing, K. G. 2006, A&A, 449, 1203
- Killeen, J. 1970, Computational Problems in Plasma Physics and Controlled Thermonuclear Research, ed. B. J. Rye & J. C. Taylor (Boston, MA: Springer US), 202
- Kopp, R. A., & Pneuman, G. W. 1976, Sol. Phys., 50, 85
- Kosugi, T., et al. 2007, Sol. Phys., 243, 3
- Lemen, J. R., et al. 2012, Sol. Phys., 275, 17
- Li, J. H., & Ma, Z. W. 2010, Journal of Geophysical Research (Space Physics), 115, A09216
- Li, T., Yang, K., Hou, Y., & Zhang, J. 2016, The Astrophysical Journal, 830, 152
- Li, T., & Zhang, J. 2015, ApJ, 804, L8
- Mariska, J. T., & Dowdy, J., James F. 1992, ApJ, 401, 754
- Nishizuka, N., Asai, A., Takasaki, H., Kurokawa, H., & Shibata, K. 2009, ApJ, 694, L74

- Ofman, L., Chen, X. L., Morrison, P. J., & Steinolfson, R. S. 1991, Physics of Fluids B, 3, 1364
- Ofman, L., Morrison, P. J., & Steinolfson, R. S. 1993, Physics of Fluids B, 5, 376
- Ofman, L., & Thompson, B. J. 2011, ApJ, 734, L11
- Okamoto, T., & Yamaguchi, I. 1991, Optics Letters, 16, 1277
- Owens, S. M., et al. 2005, in Society of Photo-Optical Instrumentation Engineers (SPIE) Conference Series, Vol. 5900, Optics for EUV, X-Ray, and Gamma-Ray Astronomy II, ed. O. Citterio & S. L. O'Dell, 5
- Parker, E. N. 1957, J. Geophys. Res., 62, 509
- Parker, E. N. 1979, Cosmical magnetic fields. Their origin and their activity
- Parker, J. D., Smart, R. T., Kankelborg, C. C., Winebarger, A. R., & Goldsworth, N. 2021, In preparation for ApJ
- Peter, H., & Judge, P. G. 1999, ApJ, 522, 1148
- Petschek, H. E. 1964, Magnetic Field Annihilation, Vol. 50 425
- Poletto, G., & Kopp, R. A. 1986, in The Lower Atmosphere of Solar Flares, ed. D. F. Neidig & M. E. Machado, 453
- Priest, E. 2014, Magnetohydrodynamics of the Sun
- Priest, E. 2020, Solar physics: Overview
- Pucci, F., & Velli, M. 2014, ApJ, 780, L19
- Qiu, J. 2009, ApJ, 692, 1110
- Qiu, J., Lee, J., Gary, D. E., & Wang, H. 2002, ApJ, 565, 1335
- Qiu, J., Wang, H., Cheng, C. Z., & Gary, D. E. 2004, ApJ, 604, 900
- Reeves, K. K., Linker, J. A., Mikić, Z., & Forbes, T. G. 2010, ApJ, 721, 1547
- Roegge, A., & Brannon, S. 2017, in American Astronomical Society Meeting Abstracts, Vol. 229, American Astronomical Society Meeting Abstracts, 339.05
- Rust, T., & Kankelborg, C. C. 2019, ApJ, 877, 59
- Rust, T. L. 2017, Ph.D. thesis, Montana State University
- Savage, S. L., McKenzie, D. E., Reeves, K. K., Forbes, T. G., & Longcope, D. W. 2010, ApJ, 722, 329

- Schmelz, J. T., Reames, D. V., von Steiger, R., & Basu, S. 2012, ApJ, 755, 33
- Seaton, D. B., Bartz, A. E., & Darnel, J. M. 2016, ArXiv e-prints
- Seaton, D. B., & Forbes, T. G. 2009, ApJ, 701, 348
- Smart, R. T., et al. 2021, In preparation for ApJ
- Steinolfson, R. S., & van Hoven, G. 1983, Physics of Fluids, 26, 117
- Sterling, A. C., Moore, R. L., Falconer, D. A., & Adams, M. 2015, Nature, 523, 437
- Strauss, H. R. 1986, Physics of Fluids, 29, 3668
- Sturrock, P. A. 1968, in Structure and Development of Solar Active Regions, ed. K. O. Kiepenheuer, Vol. 35, 471
- Takasao, S., Asai, A., Isobe, H., & Shibata, K. 2012, The Astrophysical Journal Letters, 745, L6
- Takasao, S., Asai, A., Isobe, H., & Shibata, K. 2016, ApJ, 828, 103
- Tayal, S. S., Henry, R. J. W., Keenan, F. P., McCann, S. M., & Widing, K. G. 1989, ApJ, 343, 1004
- Temmer, M. 2021, Living Reviews in Solar Physics, 18, 4
- Tian, H. 2017, Research in Astronomy and Astrophysics, 17, 110
- Tousey, R., et al. 1973, Sol. Phys., 33, 265
- Velli, M., & Hood, A. W. 1989, Sol. Phys., 119, 107
- Verhoeven, D. 1993, Appl. Opt., 32, 3736
- Warren, H. P., & Marshall, A. D. 2001, ApJ, 560, L87
- Wilhelm, K., et al. 1995, Sol. Phys., 162, 189
- Winebarger, A. R., et al. 2019, ApJ, 882, 12
- Yokoyama, T., & Shibata, K. 1998, ApJ, 494, L113
- Zhang, Q. M., Ji, H. S., & Su, Y. N. 2016, Sol. Phys., 291, 859
- Zhang, X., Li, L. J., Wang, L. C., Li, J. H., & Ma, Z. W. 2011, Physics of Plasmas, 18, 092112
- Zhitnik, I. A., Kuzin, S. V., Oraevskii, V. N., Pertsov, A. A., Sobel'Man, I. I., & Urnov, A. M. 1998, Astronomy Letters, 24, 819

## APPENDICES

APPENDIX A

DESPIKING

We developed a new image despiking algorithm with a spike intensity threshold that varies according to the local median intensity. The key to our strategy is to establish a finite number of bins for the local median intensity, and then examine the statistics of all the pixels falling into each bin. Our despiking routine is implemented in the following steps:

1. For each data dimension (image row, image column, and time), calculate a local median intensity image by averaging the nearest 11 pixels along the given axis. Divide the range of median image values into 128 bins.
2. For each local median bin, form a cumulative distribution of intensities. Identify the intensity value corresponding the 99.9th percentile. The result is three curves (one for each data dimension) of 128 points each.
3. For each data dimension, fit a line to the threshold curve. The line identifies the relationship between median intensity and spike threshold for that dimension.
4. Create three masks, which are boolean-valued images identifying pixel values that exceed the thresholds, one image per data dimension.
5. Combine the three masks with logical AND to produce the final map of bad pixels (spikes).
6. Replace each bad pixel with a local mean of good (i.e., not bad) pixels only, weighted by kernel  $k$  (Equation A.1).

The kernel used to determine the replacement value for bad pixels is

$$k(x, y, t) = e^{-\{|x|+|y|+|t|\}/a}. \quad (\text{A.1})$$

For our implementation  $a = .5$  pixels and  $x, y, t = -2, -1, 0, 1, 2$ . The kernel is normalized prior to application by its total, ignoring any other bad pixels that may fall within the kernel.

The algorithm described above has a number of advantages compared to those available in standard data prep routines for solar physics missions. We are aware of only one published example of a despiker that uses the time axis for spike identification, used by Aschwanden et al. (2000) on data from the Transition Region and Coronal Explorer (Handy et al., 1999, TRACE). In our algorithm, a pixel must stand out from its neighbors in all three dimensions to be identified as a spike. This criterion reduces false positives; yet because of this approach, we can choose a relatively sensitive percentile threshold based on image statistics to reduce false negatives. Usually, a percentile-based threshold would result in identifying a fixed number of bad pixels; but since the logical AND is nonlinear with respect to the three binary masks, it is possible to identify a small or large number of spikes in a given image. For example, with our 99.9th percentile threshold, the algorithm can find as few as zero or as many as 2129 bad pixels in a  $2048 \times 1040$  Level 1 image.

APPENDIX B

MULTIPLICATIVE ALGEBRAIC RECONSTRUCTION TECHNIQUE

The Multiplicative Algebraic Reconstruction Technique (MART) was developed for limited-angle tomography problems, in which a small number of projections are used to reconstruct a volume (Okamoto & Yamaguchi, 1991; Verhoeven, 1993). As ESIS has only four projections through the  $(x, y, \lambda)$  volume, it is a good candidate for this approach. When testing a variety of inversion methods on MOSES data, Fox (2011) identified MART as most promising of several methods in terms of speed and fidelity. Rust (2017) applied a slightly different version of MART to the MOSES data paired with a wavelet based partial reconstruction technique for better background subtraction and event isolation. Due to its speed, simplicity, and automatic enforcement of image positivity we have chosen MART for our first inversion of Level 3 ESIS data.

With MART we seek to reconstruct the true spatial-spectral cube,  $I_{xy\lambda}$ , using all four ESIS images from a single exposure. Each ESIS image,  $i_{\theta x'y'}$ , can be expressed as an angled projection through  $I_{xy\lambda}$  onto a 2-D detector, or,

$$i_{\theta x'y'} = \sum_{\lambda} I_{\theta x'(y'-\delta\lambda)\lambda}, \quad (\text{B.1})$$

where

$$I_{\theta x'y'\lambda} = \mathcal{R}_{\lambda}(\theta) I_{xy\lambda}, \quad (\text{B.2})$$

and,  $\mathcal{R}_{\lambda}(\theta)$ , is a rotation about the  $\lambda$  axis into the primed detector coordinates  $[x', y']$ . In this rotated system,  $y'$  is the dispersion direction. There is one ESIS image for each  $\theta \in \{-67.5^\circ, -22.5^\circ, 22.5^\circ, 67.5^\circ\}$ , representing the orientations of each ESIS channel. Projections through  $I$  are done along lines of constant  $y' - \delta\lambda$ . For our specific implementation, the resolution of  $I_{xy\lambda}$  in  $\lambda$  is chosen to be  $28 \text{ m}\text{\AA} \text{ pix}^{-1}$ , the spectral dispersion of an ESIS grating, such that  $\delta = 1$ .

MART attempts to find the true spatial spectral cube  $I_{xy\lambda}$  by iteratively correcting a guess cube,  $G_{xy\lambda}$ , until its projected images,  $g_{\theta x'y'}$ , match each ESIS image,  $i_{\theta x'y'}$ , with a reduced chi-squared,  $\chi^2_{R,\theta}$ , less than one. Our procedure is as follows:

1. Create a guess cube, initialized as  $G_{xy\lambda} = 1$  on the same domain as  $I$ .
2. Enhance the contrast of  $G$  and normalize.

$$G \leftarrow \frac{G + G^{(1+\Psi)}}{\sum_{xy\lambda} G + G^{(1+\Psi)}} \sum_{xy\lambda} G, \quad (\text{B.3})$$

3. Convolve  $G$  with smoothing kernel  $K$ ,  $G \leftarrow G * K$ , in our case,

$$K_{ijk} = \frac{2^{3-|i|-|j|-|k|}}{64} \quad \text{for } i, j, k = -1, 0, 1. \quad (\text{B.4})$$

4. Assuming  $\delta = 1$ , sum  $G_{\theta x'y'\lambda}$  along lines of constant  $y' - \lambda$  to calculate a projection for

each angle  $\theta$ ,

$$g_{\theta x'y'} = \sum_{\lambda} G_{\theta x'(y'-\lambda)\lambda}, \quad (\text{B.5})$$

where

$$G_{\theta x'y'\lambda} = \mathcal{R}_{\lambda}(\theta) G_{xy\lambda}, \quad (\text{B.6})$$

and,  $\mathcal{R}_{\lambda}(\theta)$ , is a rotation about the  $\lambda$  axis.

5. Calculate reduced chi-squared and check for each channel for convergence, in this case that  $\chi_{R,\theta}^2 < 1$ ,

$$\chi_{R,\theta}^2 = \frac{1}{N_{x'} N_{y'}} \sum_{x'y'} \frac{(i_{\theta x'y'} - g_{\theta x'y'})^2}{g_{\theta x'y'} + \sigma_{RN}^2}, \quad (\text{B.7})$$

where  $\sigma_{RN}$  is the read noise in photons,  $N_{x'}$  is the total number of elements along  $x'$ .

6. Calculate correction factors for each unconverged channel,  $\theta_{uc}$ , weighted by  $\gamma$ ,

$$c_{\theta x'y'} = \left[ \frac{g_{\theta x'y'}}{i_{\theta x'y'}} \right]^{\gamma}, \quad (\text{B.8})$$

where  $\gamma = 2/n$  with  $n$  equal to the total number of channels.

7. Assign correction factors to lines of constant  $y' - \lambda$  in the volume  $(x', y', \lambda)$ ,

$$C_{\theta x'(y'-\lambda)\lambda} = c_{\theta x'y'} \quad (\text{B.9})$$

8. Apply a weighted product of each derotated correction to  $G$ ,

$$G \leftarrow G \left\{ \prod_{\theta \in \Theta_{uc}} \mathcal{R}_{\lambda}(-\theta) C_{\theta x'y'\lambda} \right\}^{1/m_{uc}}, \quad (\text{B.10})$$

where  $m_{uc}$  is the total number of unconverged channels and  $\Theta_{uc}$  denotes the set of unconverged channels.

9. Repeat steps B4-B8 until every channel has converged at step B5. Once converged proceed to next step.

10. Return to Step B2 if additional filtering is desired.

The above algorithm begins with an arbitrary, flat guess (step B1). The guess is rapidly modified to fit the data projections  $i_{\theta x'y'}$  by steps B4-B8, which project through the guess, compare the results to the data, calculate and apply intrinsically positive correction factors. These steps are very similar to prior implementations of the MART algorithm. When applied to ESIS Level 3 data the total number of channels is  $n = 4$ . The rotations  $\mathcal{R}_{\lambda}(\pm\theta)$  cause ringing due to the Gibbs phenomenon associated with resampling and interpolation. All

negative values resulting from this ringing are set to zero. In our case, the ringing occurs mostly at the sharp discontinuity at the edge of the field stop octagon.

The inversion is ill-posed, in the sense that multiple different  $G_{xy\lambda}$  cubes can satisfy  $\chi^2_{R,\theta} < 1$ . In particular, tomographic inversion algorithms such as MART tend to smear intensity along the projection directions (Kak & Slaney, 2001). This tendency is especially strong when there are only a few projections. This smearing results in rapid convergence to an intensity distribution in the volume that matches the projection data, but results in artificial streaks that intersect and produce anomalous bright sources. Since the resulting artifact forms a gridlike pattern of enhancements, we use the nickname “plaid” to describe it. In the reconstructed ESIS data cube, the plaid artificially enhances the wings of the spectral line wherever projections through unrelated intense sources happen to meet. To suppress the plaid, we implement an outer filtering loop that enhances the contrast of  $G_{xy\lambda}$  and applies smoothing prior to the MART corrections to further constrain our inversions. The contrast enhancement (step B2) works to suppress the intensity of the artifacts and redistribute their intensity into the brightest features. We aim thereby to arrive at a solution with the fewest sources that are consistent with the appearance of the data. By itself, the contrast enhancement can tend to develop excess power at the Nyquist frequency and (sometimes) numerical instability. These undesired effects of contrast enhancement are suppressed by a smoothing filter (step B3).

As a result of the plaid suppression technique described above, our implementation of MART has two free parameters, namely the contrast enhancement exponent  $\Psi$  and the number of times the filtering step (steps B2 and B3) is applied. In order to better understand the impact of these two parameters on our inversions we inverted a single exposure of Event c (Figure 4.9 and 4.13) using several different values of each free parameter. During this exercise we found that lowering  $\Psi$  resulted in faster MART convergence, but required more applications of the filtering step to minimize the plaid. Increasing  $\Psi$  lowered the number of required filtering loops, but increased the convergence time of each MART iteration and quickly led to overfiltered and artificial looking results. For smaller values of  $\Psi$ , less than approximately .4, we find  $\Psi$  to be nearly degenerate with the number of filtering steps, i.e. inversions found using a lower  $\Psi$  and more filtering steps are similar to those found using a higher  $\Psi$  and less filtering steps. In the end we chose to use  $\Psi = 0.2$  in an effort to not overfilter our inversions and maintain a reasonable total algorithm convergence time.

Figure B.1 shows the results of changing the total number of filtering steps with  $\Psi = 0.2$ . While other numbers of filtering steps were tried, the inverted results after 0, 25, and 75 steps sufficiently illustrate the effect of varying this parameter. The impact of plaid is most evident in the red spectral lines in Figure B.1, where the contrast enhancement filter wasn’t used at all. Despite excess intensity in the wings of the lines from excessive plaid, the brightest pixels are still double peaked in nature and the two Gaussian fits reasonably approximate the inverted line profiles. The blue spectral lines in Figure B.1 correspond to 75 filtering steps, after which point the filtering has converged, in the sense that further filtering iterations have no effect. Since the contrast enhancement filter is designed to pull intensity from the background and into regions of stronger signal, it has the effect of clumping the intensity into a smaller area. This causes much less intensity in the far wings of the line profile and

narrower peaks overall. Unfortunately this also has the ill effect of clumping background intensity where there is very little signal. In low signal regions where we would expect a relatively flat, low intensity, and noisy line profile overfiltering can cause what little intensity is there to clump together artificially far out in the wings of the line. Therefore we choose to compromise and run the filtering step enough times, in our case 25, such that the majority of the artificial intensity in the wings has been beaten down, but not so much that we artificially remove a flat noisy line profile in low signal regions.

Regardless of the parameters chosen, we find that our inverted results match qualitative interpretations of ESIS difference images. The degree of filtering affects the breadth of the individual Gaussian components, so that they are more or less resolved. Their velocities, and relative intensities also vary, but are less affected. An extreme parameter range was explored, from no filtering to maximal (fully converged) filtering. We have argued that both extremes represent implausible solutions on physical grounds. Consequently, we conclude that the relative velocities and intensities of the double Gaussian fits are robust, while their widths are uncertain.

The final configuration we used when inverting all Level 3 data used 25 filtering steps and a contrast enhancement exponent of  $\Psi = 0.2$ . In this configuration, a single exposure of a small region like event c (with final inverted dimensions of  $[x, y, \lambda] = [140, 140, 41]$  pixels) can be inverted in  $\approx 75$  seconds on a single thread of a four core 2.8 GHz processor. Since the inversion of each ESIS exposure is independent, inversions can be done on multiple threads to increase efficiency when inverting additional exposures.

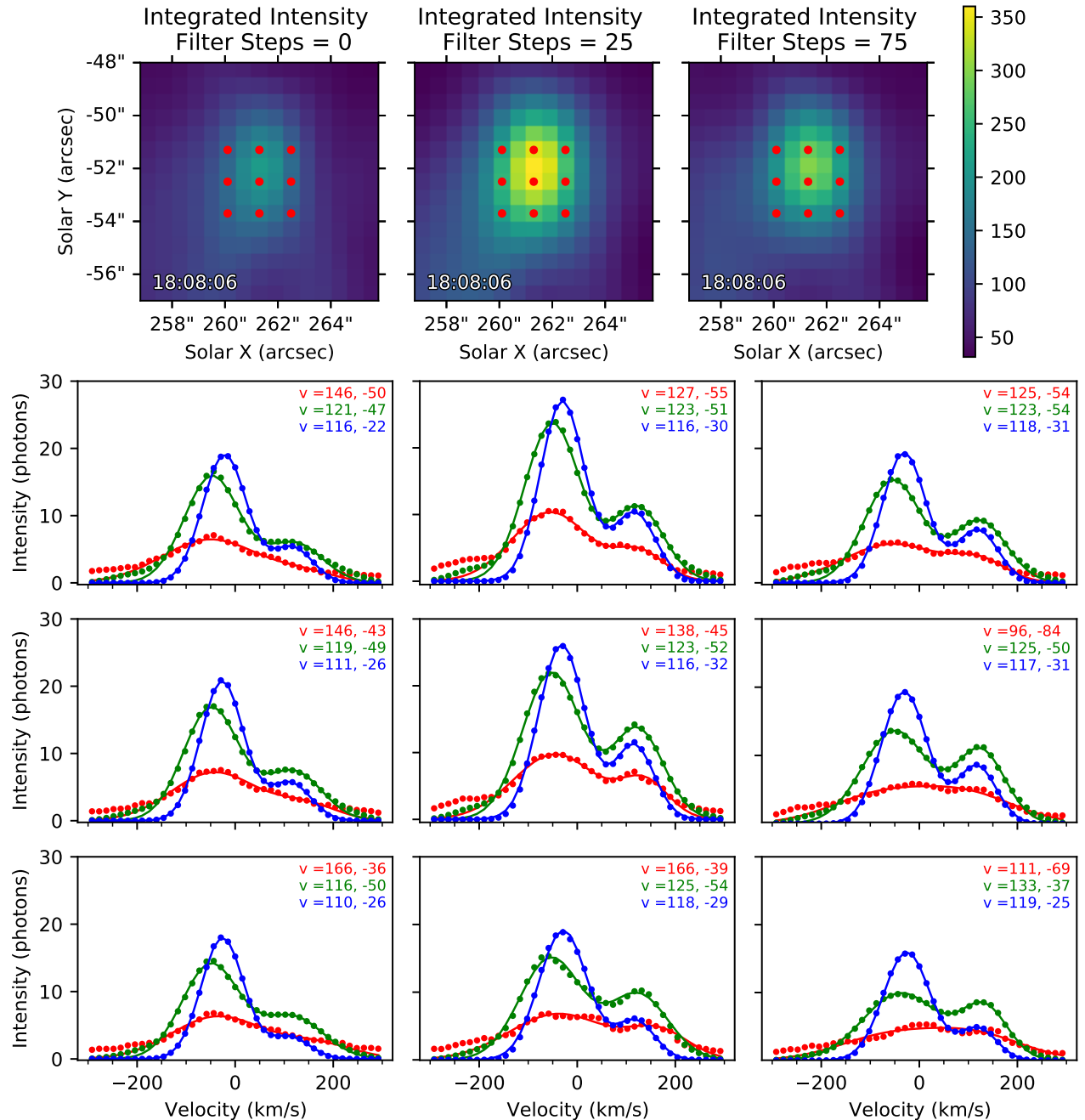


Figure B.1: Comparison of MART outputs for a single timestamp in Event c (Figure 4.9 and 4.13) with different amounts of filtering. The top row shows the total inverted intensity at a single timestamp each using a different number of MART filtering steps (steps B2 and B3). The lower grid shows the inverted O V spectral line at each red dot for 0, 25, and 75 filtering steps in red, green, and blue respectively.